Copyright
by
Xiangrong Fu
2013

The Dissertation Committee for Xiangrong Fu
certifies that this is the approved version of the following dissertation:

# Turbulent Particle and Thermal Transport in Magnetized Plasmas

Committee:

Philip Morrison, Supervisor

Wendell Horton, Supervisor

Herbert Berk

Gennady Shvets

Gary Hallock

# Turbulent Particle and Thermal Transport in Magnetized Plasmas

**by**

**Xiangrong Fu, B.S., M.S.**

**DISSERTATION**

Presented to the Faculty of the Graduate School of

The University of Texas at Austin

in Partial Fulfillment

of the Requirements

for the Degree of

**DOCTOR OF PHILOSOPHY**

THE UNIVERSITY OF TEXAS AT AUSTIN

May 2013

Dedicated to Ying, Cindy and Abby.

# Acknowledgments

I wish to thank Prof. Wendell Horton for his guidance on my research. He encourages me to collaborate with many groups of people and spends a lot of time editing my papers, thesis, and presentations. I thank Prof. Philip Morrison for all his inspiring courses on physics and math and for being my official supervisor. I also thank Prof. Zhihong Lin and Dr. Yong Xiao at UC Irvine for teaching me the GTC code.

Students and staff members in IFS help me a lot. I would like to thank Jane Pratt, Cynthia Correa, Ehab Hassan, Jingfei Ma and Dmitry Meyerson for helpful discussions and group study.

I am deeply grateful to my wife Ying Zhang for taking care of our family and bringing joys and blessings. Without her, it would be impossible to finish my Ph.D work and the life in Austin would have been much duller.

I also thank brothers and sisters in Austin Christian Assembly for their love and prayer. I owe everything to Jesus Christ our Lord.

# Turbulent Particle and Thermal Transport in Magnetized Plasmas

Publication No. _____

Xiangrong Fu, Ph.D.
The University of Texas at Austin, 2013

Supervisors: Philip Morrison
Wendell Horton

The particle and thermal transport by low-frequency drift waves in magnetized plasmas are studied with theories and simulations. Universal in inhomogeneous plasmas, drift waves in Earth's ionosphere, the GAMMA-10 Tandem Mirror machine, the Columbia Linear Machine and C-Mod tokamak are studied in this thesis.

The first investigations are the $\mathbf{E} \times \mathbf{B}$ particle transport in the given electric and magnetic fields of the GAMMA-10 mirror machine at the University of Tsukuba in Japan. The results show that the formation of $E_r$-shear by local heating of electrons can reduced the radial particle loss.

The turbulent impurity particle transport driven by various modes in the MIT tokamak Alcator C-Mod is studied by a quasilinear theory and compared to experimental measurement of Boron density profiles. A code is developed for solving eigensystems of drift wave turbulence equations for the

multi-component fusion plasmas and calculating quasilinear particle fluxes. The calculations are much faster than nonlinear simulations and may be suitable for real-time analysis and feedback control of tokamak plasmas.

The electron temperature gradient (ETG) mode is a candidate mechanism for anomalous electron thermal transport across various magnetic confinement geometries. This mode was produced in the Columbia Linear Machine (CLM) at Columbia University. Large scale simulations of the ETG mode in the CLM by a gyrokinetic code GTC are carried out on supercomputers at TACC and NERSC. The results show good agreement with experiments in the dominant mode number, wave frequencies and the radial structure. Some nonlinear properties are also analyzed using the code.

# Table of Contents

**Acknowledgments** **v**

**Abstract** **vi**

**List of Tables** **xii**

**List of Figures** **xiii**

**Chapter 1. Introduction** **1**
1.1 Magnetic Confinement of Plasmas . . . . . 1
1.2 Classical, Neoclassical and Turbulent Transport . . . . . 5
1.3 Drift Wave Basics . . . . . 7

**Chapter 2. Methods and Models for Transport Study** **10**
2.1 Kinetic Methods . . . . . 10
2.1.1 Gyrokinetic Method . . . . . 10
2.1.2 Drift Kinetic Method . . . . . 12
2.2 Fluid Methods . . . . . 13
2.3 Computer Simulations . . . . . 13
2.3.1 Fluid Simulations . . . . . 14
2.3.2 Gyrokinetic Simulations . . . . . 15
2.3.3 Computing Resources . . . . . 15
2.4 Turbulent Transport Models . . . . . 16
2.4.1 Hasegawa-Mima Model . . . . . 17
2.4.2 Density-Gradient-Driven Drift Waves . . . . . 20
2.4.3 Ion Temperature Gradient Modes . . . . . 24
2.4.4 Trapped Electron Modes . . . . . 26
2.4.5 Electron Temperature Gradient Modes . . . . . 27
2.4.6 Drift Waves in Earth's ionosphere and magnetosphere . 31

**Chapter 3. Particle Transport in Mirror Machines** **37**
3.1 Gamma-10 at the University of Tsukuba . . . . . 37
3.2 Drift Waves in the Mirror Machine . . . . . 38
3.3 Particle Transport in Gamma-10 . . . . . 39

**Chapter 4. Impurity Transport in Tokamaks** **48**
4.1 Impurity Transport . . . . . 48
4.2 C-Mod Impurity Experiments . . . . . 49
4.3 Quasilinear Theory . . . . . 50
4.3.1 Density Gradient Driven Drift Waves . . . . . 51
4.3.2 Slab Geometry . . . . . 53
4.3.2.1 Linear Analysis . . . . . 55
4.3.3 Toroidal Effects . . . . . 58
4.3.3.1 Without Impurity . . . . . 61
4.3.3.2 With Impurity . . . . . 62
4.4 Impurity Drift Waves . . . . . 65
4.4.1 Ion Parallel Motion . . . . . 65
4.4.2 Impurity Drift Waves . . . . . 66
4.5 Passive Impurity Transport . . . . . 69
4.6 Neoclassical Impurity Transport . . . . . 70
4.7 Kinetic Theory of Fluctuations . . . . . 71
4.8 Turbulent Particle Transport . . . . . 72
4.8.1 Quasilinear Flux . . . . . 72
4.8.2 Impurity Transport in the Slab Geometry . . . . . 72
4.8.3 Impurity Transport in the Toroidal Geometry . . . . . 73
4.8.4 Fluctuation Spectrum . . . . . 74
4.9 Ion Temperature Gradient . . . . . 75
4.10 Trapped Electron Mode . . . . . 77
4.11 Conclusions . . . . . 87

**Chapter 5. Electrostatic Electron Temperature Gradient Mode 90**
5.1 Kinetic theory for the ETG mode . . . . . 91
5.2 ETG modes in the CLM experiments . . . . . 95
5.3 Linear Properties of ETG Modes in a Cylinder . . . . . 99
5.4 Gyrokinetic Simulations using GTC code . . . . . 100
5.4.1 Numerical Results . . . . . 102
5.4.1.1 Modeling electron temperature and density profiles 104
5.4.1.2 Time history of the simulation . . . . . 104
5.4.1.3 Time history of two modes . . . . . 105
5.4.1.4 Radial profile of the electric potential fluctuations 108
5.4.1.5 Heat flux . . . . . 109
5.4.2 Parametric Variations of Measured Signal and those from Simulations . . . . . 109
5.4.2.1 Variation of fluctuations with the temperature gradient . . . . . 109
5.4.2.2 Variation of the fluctuations with parallel wavenumber or axial Length . . . . . 112
5.4.3 Nonlinear Saturation of ETG modes . . . . . 113
5.5 A Hamiltonian Model for ETG . . . . . 115
5.5.1 Finite-dimensional Hamiltonian System . . . . . 115
5.5.2 Hamiltonian for Infinite-Dimensional System . . . . . 116
5.5.2.1 Functional Derivatives . . . . . 116
5.5.2.2 Generalized Hamiltonian Field Theory . . . . . 116
5.5.2.3 Jacobi Identity . . . . . 117
5.5.3 Electrostatic ETG Turbulence . . . . . 117
5.5.3.1 Model Equations . . . . . 117
5.5.3.2 Noncanonical Poisson Bracket . . . . . 119
5.5.4 Conservation Laws . . . . . 120
5.6 Conclusions . . . . . 120

**Chapter 6. Summary 122**

**Appendices 124**

**Appendix A. Plasma Dispersion Function** **125**
A.1 Plasma Dispersion Function . . . . . 125
A.2 Computational Method . . . . . 126
A.2.1 Direct Method . . . . . 126
A.2.2 Integral Transform . . . . . 127

**Appendix B. Useful Expressions** **133**

**Appendix C. Index of Notation** **135**
C.1 General notation . . . . . 135
C.2 Special notations . . . . . 136

**Index** **151**

**Vita** **152**

# List of Tables


2.1 Typical parameters inside and outside the plasmapause. The location of the plasmapause is at $\sim 4R_E$. . . . . 36

4.1 Reference parameters of ITER and C-Mod. . . . . 64

4.2 Parameters for C-Mod experiments . . . . . 80

4.3 Comparison of C-Mod and LHD parameters . . . . . 88

5.1 Machine and plasma parameters for a typical ETG experiment in the Columbia Linear Machine. . . . . 96

# List of Figures


1.1 A closed magnetic field line in the tokamak, with $m = 2$, $n = 1$. Arrows point to the local direction of the magnetic field, and the color represents the strength of the $B$ field. . . . . 3

1.2 Tokamak with a circular cross section, with major radius $R_0$ and minor radius $a$. . . . . 4

1.3 A gyrating ion undergoes collision with neutral atoms. The ion diffuses away, no longer being attached to a certain field line. . 6

1.4 Drift waves with (a) $\delta n$ and $\phi$ in phase (b) $\delta n$ and $\phi$ out of phase. A net flux of particles in the $x$ direction is generated in (b), while no net flux in (a). . . . . 8

1.5 The role of the phase shift on the particle flux for fixed fluctuation amplitudes is shown by comparing the left figure, where the potential leads the density by 1 radian phase, with the right figure, where the potential lags the density by 1 radian for a wave propagating to the right. $\delta n = \sin(y)$, $\phi = \sin(y + \Delta)$. . . . . 9

2.1 The growth rate and frequency of drift waves as a function of $\nu_{\|}$. 23

3.1 A schematic of the Gamma-10 machine: (a) the coils that generate confining magnetic field, (b) the magnetic flux surface, and (c) the electric potential $\Phi$ and the magnetic field $B$ on the axis. . . . . 39

3.2 Radial profile of the electric potential $\Phi$ measured in Gamma-10 (Reproduced from Ref. [12].) . . . . . 40

3.3 Models for the electric potential $\Phi$ in Gamma-10 . . . . . 43

3.4 $I - \theta$ phase space map for the monotonic potential $\Phi_1$, with $e\phi_m/T_e = 0.01, 0.02, 0.05, 0.1, 0.2, 0.4$, using Eqs. (3.11)-(3.12). 44

3.5 $I - \theta$ phase space map for the $E_r$-reversed potential $\Phi_2$. . . . . 45

3.6 $I - \theta$ phase space map for the nontwist potential $\Phi_3$. . . . . 46

4.1 (a)Time evolution of boron density profile in the C-Mod discharge with 3.5 MW ICRF heating, from the H-mode (blue circles), transition (black squares), to ITB (red triangles); (b) boron density gradient profile in H-mode (blue dash) and ITB (red solid).[60] . . . . . 49

4.2 The frequencies and growth rates versus $k_y\rho$ for the three modes for the density-gradient-driven drift wave, based on typical C-Mod parameters in plasmas with peaked impurity profiles. (a)-(b) The frequency and growth rate of the impurity mode. (c)-(d) The frequency and growth rate of the electron drift wave mode. (e)-(f) The frequency and growth rate of the damped mode. . . . . 63

4.3 Polarization diagram of two eigenmodes of the drift wave model. 64

4.4 The frequencies and growth rates versus $k_y\rho$ for the three modes for the ITG model (same parameters as in Fig. 4.2). . . . . 78

4.5 Main ion turbulent flux and impurity flux versus impurity density gradients ($R/L_{nz}$) for a set of typical C-Mod parameters, for the ITG mode. From the slope and the intercept of the curve we can extract the transport coefficients $D$ and $V$. The negative values of $R/L_{nz}$ correspond to hollow impurity profiles with inward impurity particle fluxes. . . . . 81

4.6 C-Mod shot #1070831028 H-mode (a) plasma density, electron temperature, and boron density profiles, (b) calculated diffusion coefficients (black curves) and convection velocity (blue curves), (c) comparison of neoclassical $V/D$ with experimental results ($= -1/L_{nz}$) and (d) neoclassical and turbulent particle fluxes for impurities ("DW" means impurity drift wave, "ITG" means the ITG mode, "NEO" means neoclassical results, and "EXP" means experimental results). . . . . 82

4.7 C-Mod shot #1070831028 ITB regime (a) plasma density, electron temperature, and boron density profiles, (b) calculated diffusion coefficient and convection velocity, (c) comparison of neoclassical $V/D$ with experimental results and (d) neoclassical and turbulent particle fluxes for impurities (same notation as in Fig. 4.6). . . . . 83

4.8 C-Mod shot #1101209010 I-mode (a) plasma density, electron temperature, and boron density profiles, (b) calculated diffusion coefficient and convection velocity, (c) comparison of neoclassical $V/D$ with experimental results and (d) neoclassical and turbulent particle fluxes for impurities (same notation as in Fig. 4.6). . . . . 84

5.1 The frequency and growth rate of ETG as a function of $\eta_e$ using Eq. (5.14). The parameters are $k_y\rho_e = 0.5$, $k_z\rho_e = 0.01$, $\rho_e/L_{ne} = 0.1$. The dashed lines in the upper and lower panels show $|\omega_r| = k_z v_{te}$ and $|\gamma| = k_z v_{te}$, respectively. . . . . 94

5.2 (a) Radial profiles of electron temperature $T_e$, ion temperature $T_i$ and plasma density $n_e$ measured in the CLM. Two sets of data with two different bias voltages (thus different temperature gradients) are shown. A strong electron temperature gradient is produced between $r = 1.5\,\text{cm}$ and $r = 2.2\,\text{cm}$. Note that the density in the region of $1.5\,\text{cm} < r < 2.2\,\text{cm}$ is nearly flat. The electron velocity distribution is close to a local Maxwell-Boltzmann distribution with the temperature $T_e(r)$ and a constant electron density $n_e$. The ion temperature is also constant and less than 1/5 the electron temperature. (b) The power spectra of the signals picked up by a high frequency probe are recorded for various temperature gradients ($a/L_{T_e}$). For strong enough temperature gradient, $L_{T_e} < 0.428\,\text{cm}$, signals are found to be peak around 2.4 MHz in the laboratory frame. Reprinted with permission from Wei et al. [65]. Copyright 2010 American Institute of Physics. . . . . 98

5.3 The radial profile of the electric potential fluctuation measured in the CLM, peaking around $r = 1.7\,\text{cm}$. Reprinted with permission from Ref. [65]. Copyright 2010 American Institute of Physics. . . . . 99

5.4 The dispersion relation of the slab ETG mode without density gradient, given by Eq. (5.16). There are three modes: mode 1 is purely damping; mode 2 and mode 3 are complex conjugates. We are interested in the unstable mode 2, whose growth rate is larger than the frequency. The growth rates obtained from linear simulations are shown as blue crosses. . . . . 101

5.5 The electron temperature profile for GTC simulations. The experimental results are shown as the dotted curve with plus signs. The analytic model is depicted by the solid curve, and the dash curve is its inverse scale length $1/L_{Te}$. The triangle marks the radial position of the maximum gradient of the model. 103

5.6 The time evolution of the root-mean-square of the electric potential $\langle\phi\rangle = \int_V \sqrt{\phi^2} d^3r / \int_V d^3r$, and the radial electron energy flux $q_e = \int\int \frac{cE_\theta}{2B} m_e(v^2 - v_0^2)\delta f d^3v d^3r / \int_V d^3r$. . . . . 105

5.7 Contours of the electric-potential fluctuation in the poloidal plane at a) linear stage $t = 2000t_0$, and b) nonlinear stage $t = 4000t_0$. In the linear stage, the fastest growing mode with $m \approx 70$, $n = 2$ ($m, n$ are the poloidal and the parallel mode number, respectively) dominates, while in the nonlinear stage, $m \approx 12$, $n = 1$ mode dominates. . . . . 106

5.8 The poloidal power spectra of the electric potential fluctuation at $r = 1.88\,\mathrm{cm}$. The strong nonlinear coupling causes inverse cascading, and the peaking mode shifts from $m = 55$ down to $m = 12$. . . . . 107

5.9 The time history of the electric potential of $m = 15$ mode and $m = 60$ mode. The solid line is the real part and the dotted line is the imaginary part. The frequency of $m = 15$ mode is about 0.24 MHz in the nonlinear stage. . . . . 108

5.10 The evolution of the radial profile of the electric potential fluctuation averaged over an $r =$ constant surface, with the green curve corresponding to $t = 2000t_0$, the blue curve to $t = 3000t_0$, and the black curve to $t = 4000t_0$. The background electron temperature profile is fixed with the maximum gradient at $r = 1.8\,\mathrm{cm}$ and maximum $1/L_{Te}$ at $r = 2.1\,\mathrm{cm}$. Due to nonlinear effects, the peak of the fluctuation profile moves inward in time. . . . . 110

5.11 The evolution of the radial profile of the electron energy flux, with the green curve corresponding to $t = 2000t_0$, the blue curve to $t = 3000t_0$, and the black curve to $t = 4000t_0$. . . . . 111

5.12 (a) Various background electron temperature profiles for simulations, with the minimum $L_{T_e} = 0.33\,\mathrm{cm}, 0.45\,\mathrm{cm}$, and $0.66\,\mathrm{cm}$. (b) Comparison of the maximum potential fluctuation, the maximum electron heat flux, the averaged potential fluctuation, and the averaged electron heat flux between these simulations. . . 112

5.13 The power spectrum of electric potential fluctuation in the nonlinear stage. Shown is a power-law decay with the intensity proportional to $k^{-1}$ for $10 < m < 100$ modes, and $k^{-3}$ for $m > 100$ modes. . . . . 114

A.1 Plasma dispersion function $Z(\zeta)$ and its derivative with real argument $\zeta = x$. . . . . 129

A.2 The general behavior of the plasma dispersion function $Z(x + iy)$. 130

# Chapter 1

# Introduction

## 1.1 Magnetic Confinement of Plasmas

The ultimate goal of controlled thermonuclear fusion is to confine high temperature gases (plasmas) for a long enough time to make sustained nuclear fusion reactions for creating a new carbon-free electric power supply for civilian use. Unlike the Sun, which confines hot plasma by its gravity, laboratory devices on the Earth use either inertia or magnetic fields to confine plasmas. The most feasible reaction in the lab is the deuterium-tritium (D-T) reaction

$$ {}^{2}_{1}\mathrm{D} + {}^{3}_{1}\mathrm{T} \longrightarrow {}^{4}_{2}\mathrm{He}\,(3.5\mathrm{MeV}) + {}^{1}_{0}\mathrm{n}\,(14.1\mathrm{Mev}). $$

The famous Lawson criterion states that for the D-T reaction to reach ignition (energy produced by the reaction exceeds the energy losses without external power input), the product of plasma density $n_e$ and the energy confinement time $\tau_E$ must satisfy

$$ n_e \tau_E \geq 1.5 \times 10^{20}\,\mathrm{m}^{-3}\mathrm{s} \tag{1.1} $$

where the minimum occurs at temperature T = 25 keV (1 eV≈11600 K). These plasma parameters pose strong gradients of density and temperature

across the machine confining the plasma since at the wall the plasma density drops to zero and temperature drops to the room temperature.

The most promising way (at present) of confining plasmas is to use strong magnetic fields to harness hot charge particles comprising the plasma. Among many configurations of confinement field, closed field line geometries of the tokamak and stellarator are most popular. In fact, the international project ITER (Table 4.3), which is still under construction, will be the largest tokamak ever built. In the tokamak geometry, a donut shaped (torus) plasma is confined by a closed magnetic field generated by the combination of the current in external coils and the internal current carried by the plasma. The $m = 2$, $n = 1$ magnetic field line of an axisymmetric tokamak plasma with circular cross section is shown in Fig. 1.1, where $m$ and $n$ are the number of turns the field line travels in the long (toroidal) way and in short (poloidal) way around the torus before it closes on itself. Two key parameters for a tokamak are the major radius $R_0$ and minor radius $a$ as shown in Fig. 1.2.

In the 70's and 80's, MHD was the focus of plasma stability and control. However, as the confinement approached the criterion in Eq. (1.1), low-frequency small-scale turbulence driven by micro-instabilities dominated the transport and produced the turbulent transport observed in tokamaks. Drift wave instabilities, driven by density and temperature gradients arise in such inhomogeneous plasmas, and degrade the confinement. We shall discuss more on drift waves later.

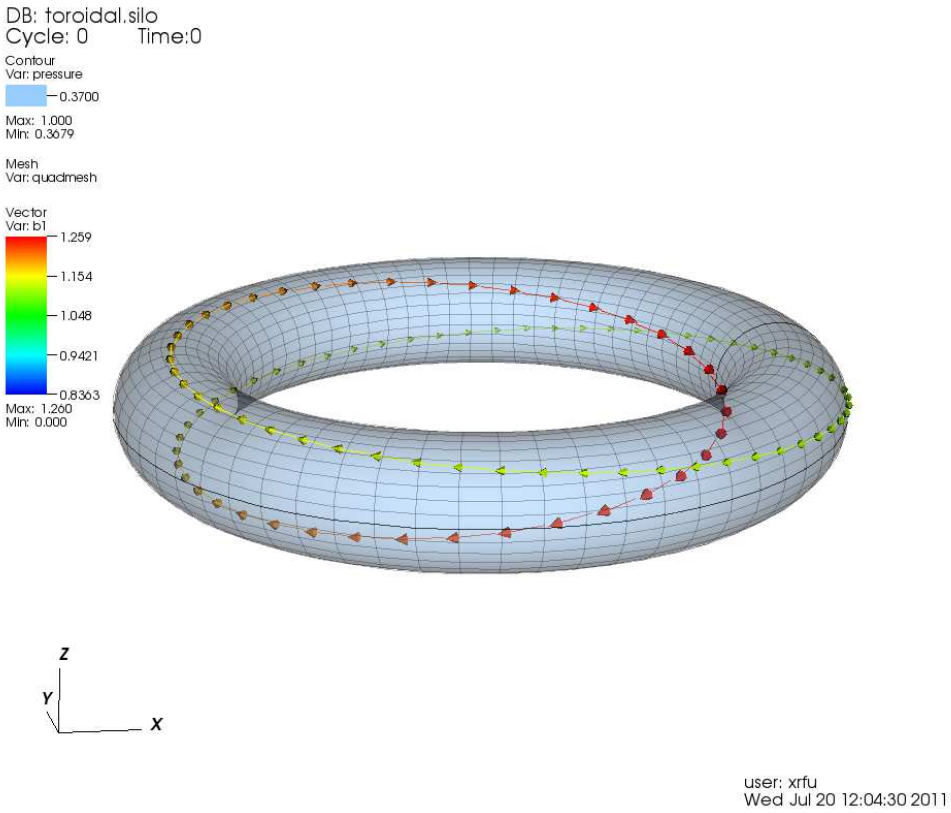


Figure 1.1: A closed magnetic field line in the tokamak, with $m = 2$, $n = 1$. Arrows point to the local direction of the magnetic field, and the color represents the strength of the $B$ field.

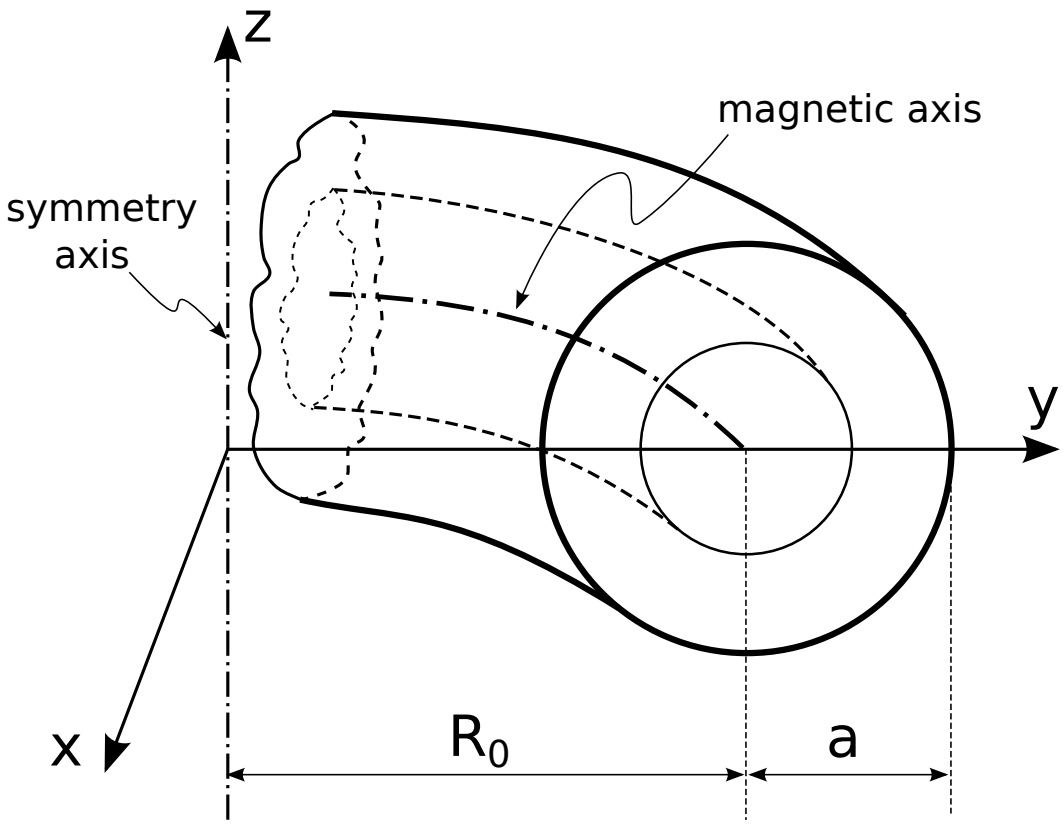


Figure 1.2: Tokamak with a circular cross section, with major radius $R_0$ and minor radius $a$.

## 1.2 Classical, Neoclassical and Turbulent Transport

Although the magnetic field is a very good insulator for plasmas, there always exist some sort of "leaking" even for closed magnetic field lines, i.e. particle, momentum or energy fluxes perpendicular to the magnetic field. In other words, there exist *transport* across magnetic field lines.

Let us take a look at a simple picture with an ion (proton) gyrating in a constant magnetic field, as shown in Fig. 1.3. In the collisionless case, the trajectory of a ion is a circle and the ion is "attached" to a field line. However, if there is a collision (e.g. with a neutral atom), the trajectory of the ion changes abruptly, causing the ion to jump from one field line to another. Thus, particles diffuse and spatial inhomogeneity is reduced by such an effect. In the absence of collisions the system is of Hamiltonian form with given complex electromagnetic fields. Collisions add a stochastic component to the dynamics that breaks the volume preserving flow in the single particle phase space.

Classical transport theory studies the transport of plasma due to (Coulomb) collisions in homogeneous magnetic fields, while neoclassical theory deals with transport in inhomogeneous magnetic fields, especially the effect of the tokamak geometry with both curvature and spatial variation of the magnetic field. Both classical and neoclassical theories are complete. However, turbulent transport, which is still an open and active area of research, studies the transport caused by fluctuating electric and magnetic fields. Drift wave or drift-wave like turbulence is one of the most important mechanisms for turbulent

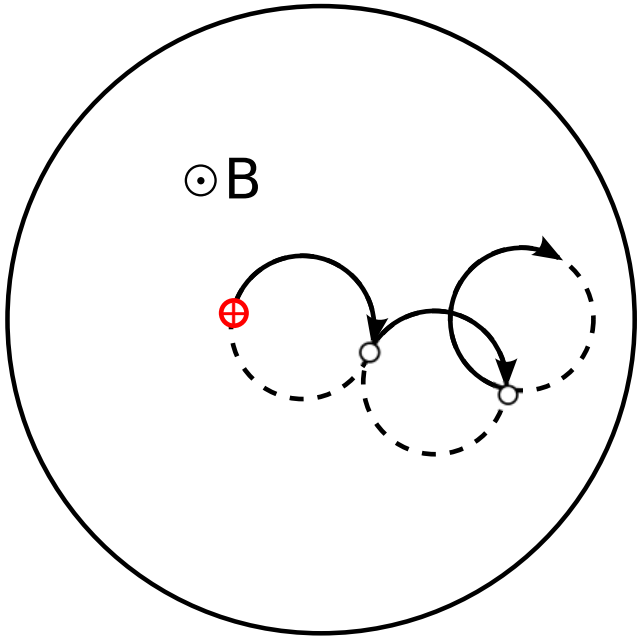


Figure 1.3: A gyrating ion undergoes collision with neutral atoms. The ion diffuses away, no longer being attached to a certain field line.

transport.

Comprehensive references for transport research are the three books by R. Balescu, covering classical[4], neoclassical[5] and turbulent[6] transport in plasmas. New progress on turbulent transport in magnetized plasmas can be found in a recent book by Horton [37].

## 1.3 Drift Wave Basics

In the magnetized inhomogeneous plasma, the bulk of the plasma moves in the direction of the diamagnetic drift

$$\mathbf{v}_* = \frac{\mathbf{b} \times \nabla p}{qnB}. \tag{1.2}$$

In the configuration shown in Fig. 1.4, the plasma density has a gradient in the $-x$ direction, the $\mathbf{B}$ field points in the $z$ direction out-of-plane and electrons drift in the $y$ direction.

The mechanism of turbulent particle transport driven by drift waves is as follows. Suppose a fluctuation of the electric potential $\phi$ produces an electric field $\mathbf{E}$ pointing out from the center of the excess, as in Fig. 1.4(a). Then, the plasma will rotate at the $\mathbf{E} \times \mathbf{B}$ velocity, causing the high and low density plasma to mix. If the density fluctuation $\delta n$ is in-phase with the electric potential fluctuation $\phi$, particle flux in positive $x$ direction cancels the particle flux in negative $x$ direction and there is no net flux. However, if there is phase difference between $\delta n$ and $\phi$ (due to dissipation, for example) as shown in Fig. 1.4(b), a net particle flux arises. The particle flux across the magnetic field in the $x$ direction is given by the average of the density fluctuation times the $\mathbf{E} \times \mathbf{B}$ drift velocity along the $y$ direction,

$$\Gamma = \langle \delta n \mathbf{v}_E \rangle \propto -\mathfrak{Im}(\delta n/\phi)|\phi|^2, \tag{1.3}$$

where $\mathbf{v}_E = c\mathbf{B} \times \nabla\phi/B^2$. The phase shift between $\delta n$ and $\phi$ determines the direction of the particle flux, as shown in Fig. 1.5. If $\phi$ leads $\delta n$, the net flux

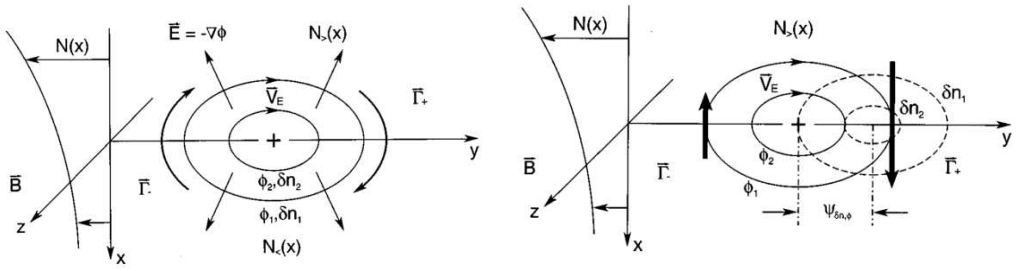


(a) in-phase (b) out-of-phase

Figure 1.4: Drift waves with (a) $\delta n$ and $\phi$ in phase (b) $\delta n$ and $\phi$ out of phase. A net flux of particles in the $x$ direction is generated in (b), while no net flux in (a).

is in positive $x$ direction, otherwise if $\phi$ lags $\delta n$, the net flux is in the negative $x$ direction.

The derivation of the drift wave equations and dispersion relation will be presented in the next chapter. A comprehensive reference of drift waves and transport is given by Horton [32].

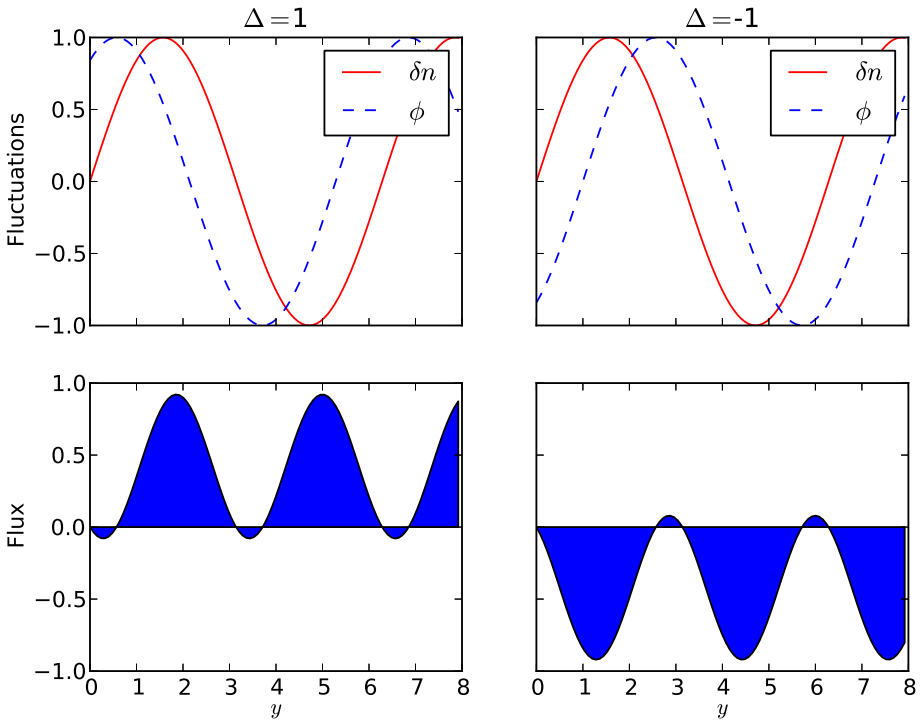


Figure 1.5: The role of the phase shift on the particle flux for fixed fluctuation amplitudes is shown by comparing the left figure, where the potential leads the density by 1 radian phase, with the right figure, where the potential lags the density by 1 radian for a wave propagating to the right. $\delta n = \sin(y)$, $\phi = \sin(y + \Delta)$.

# Chapter 2

# Methods and Models for Transport Study

In this chapter, the analytical and numerical methods used in this thesis are summarized. Also, various models for turbulent transport are introduced.

## 2.1 Kinetic Methods

Plasmas are complex with a huge number of degrees of freedom. Instead of describing the motions of individual particles, one can use a distribution function $f(\mathbf{x}, \mathbf{v}, t)$. Due to the conservation of particle number, the equation for the distribution function can be written as

$$\frac{df}{dt} \equiv \frac{\partial f}{\partial t} + \mathbf{v} \cdot \frac{\partial f}{\partial \mathbf{x}} + \frac{\mathbf{F}}{m} \cdot \frac{\partial f}{\partial \mathbf{v}} = 0 \tag{2.1}$$

where $\mathbf{F}(\mathbf{x}, t)$ is the Lorentz force acting on the particle of mass $m$.

### 2.1.1 Gyrokinetic Method

In the presence of strong magnetic fields, the gyration of charge particles can be orders of magnitude faster than motion across the magnetic field lines. Therefore if we are interested in plasma phenomena on time scales much slower than that of gyromotion, the gyromotion can be averaged out and only the motion of the guiding center traced. This process effectively reduces the

6-dimensional distribution function $f(\mathbf{x}, \mathbf{v})$ to a 5-dimensional phase space density $F(\mathbf{R}, \mu, v_\parallel)$. Also, due to the removal of the fast gyromotion, the time step can be much larger than gyrofrequencies, and thus save a lot of time for computer simulations. With present-day supercomputers, gyrokinetic particle simulations of the plasma in an entire plasma machine are made possible.

There are three approaches to derive the gyrokinetic equation:

1) Conventional: One performs a coordinate transformation from $(\mathbf{x}, \mathbf{v})$ space to guiding center space $(\mathbf{R}, \mu, v_\parallel, \phi)$, and then average over the phase angle $\phi$ based on the gyrokinetic ordering. For example, Lee [44] derived the gyrophase-averaged Vlasov equation and devised a new scheme for particle simulations.

2) Lie transform: The Lie transform method is based on the variational principle of the guiding center motion, which was first introduced by Littlejohn [49]. A recent review on nonlinear gyrokinetic equations can be found in Brizard and Hahm [9].

3) Mixed variable generating function: This method is based on Pfirsch-Morrison Hamilton-Jacobi action principle [57], and it was published in two papers [58, 13].

The electromagnetic gyrokinetic equation reads [31]:

$$\frac{d}{dt} f_\alpha \left(\mathbf{X}, \mu, v_\parallel, t\right) \equiv \left[\frac{\partial}{\partial t} + \dot{\mathbf{X}} \cdot \nabla + \dot{v}_\parallel \frac{\partial}{\partial v_\parallel} - \mathcal{C}_\alpha\right] f_\alpha = 0, \tag{2.2}$$

$$\begin{aligned} \dot{\mathbf{X}} &= v_\parallel \frac{\mathbf{B}}{B_0} + \mathbf{v}_E + \mathbf{v}_d \\ \dot{v}_\parallel &= -\frac{1}{m_\alpha} \frac{\mathbf{B}^*}{B_0} \cdot (\mu \nabla B_0 + Z_\alpha \nabla \phi) - \frac{Z_\alpha}{m_\alpha c} \frac{\partial A_\parallel}{\partial t}. \end{aligned} \tag{2.3}$$

where species index $\alpha = e, i$ for electron and ion. $Z_\alpha$ is the particle charge and $m_\alpha$ is the particle mass, $\mathbf{B}_0 \equiv B_0 \mathbf{b}_0$ is the spatially varying equilibrium magnetic field, $\mathbf{B} \equiv \mathbf{B}_0 + \delta\mathbf{B}$, and

$$\mathbf{B}^* = \mathbf{B}_0^* + \delta\mathbf{B} = \mathbf{B}_0 + \frac{B_0 v_\parallel}{\Omega_\alpha} \nabla \times \mathbf{b}_0 + \delta\mathbf{B}.$$

The gyrokinetic Poisson's equation and Ampere's law are

$$\frac{4\pi Z_i^2 n_i}{T_i} \left( \phi - \tilde{\phi} \right) = 4\pi \left( Z_i n_i - e n_e \right), \tag{2.4}$$

$$\nabla_\perp^2 A_\parallel = \frac{4\pi}{c} \left( e n_e u_{\parallel e} - Z_i n_i u_{\parallel i} \right), \tag{2.5}$$

where $\delta\mathbf{B} = \nabla \times A_\parallel \mathbf{b}_0$ is the magnetic fluctuation. In writing Eq. (2.4), we assume the Debye length is much smaller than the spatial scale of the fluctuation. $\tilde{\phi}$ is the gyro-averaged electric potential.

### 2.1.2 Drift Kinetic Method

The gyrokinetic description can be greatly simplified if the gyroradii are much smaller than the spatial scale of interest, which leads to the drift kinetic models. The derivation of drift-kinetic equations is in textbooks [e.g. 24]. For a simple low-$\beta$(electrostatic) slab plasma, the drift-kinetic equation for electrons is given by

$$\frac{\partial f_e}{\partial t} + \mathbf{v}_E \cdot \nabla_\perp f_e + v_z \frac{\partial f}{\partial z} - \frac{e}{m} E_z \frac{\partial f_e}{\partial v_z} = 0 \tag{2.6}$$

where $\mathbf{v}_E = c\mathbf{E} \times \mathbf{B}/B^2$.

## 2.2 Fluid Methods

By taking velocity moments of the kinetic equation, one can get a chain of coupled fluid equations. The first few moments are density, fluid velocity and temperature given by

$$\begin{aligned} n_\alpha(\mathbf{x}) &= \int f_\alpha(\mathbf{x},\mathbf{v}) d^3v \\ n_\alpha \mathbf{v}_\alpha(\mathbf{x}) &= \int \mathbf{v} f_\alpha(\mathbf{x},\mathbf{v}) d^3v \\ n_\alpha T_\alpha(\mathbf{x}) &= \frac{1}{3}\int m_\alpha(\mathbf{v}-\mathbf{v}_\alpha)^2 f_\alpha(\mathbf{x},\mathbf{v}) d^3v. \end{aligned}$$

These quantities are more accessible experimentally than the distribution function. However, since the argument of $f_\alpha$ is 6-dimensional, while the arguments of each moment are only 3-dimensional, we need an infinite number of moments to fully represent the distribution function. In fact, we usually only use the first few moments and truncate the chain of moment equations based on some assumptions or closures of higher moments.

In the presence of strong magnetic fields, the plasma fluid equations can be further reduced according to the drift ordering. In Sec. 2.4, we will derive some well known reduced fluid models.

## 2.3 Computer Simulations

Due to the complicated geometry of confining magnetic fields and the lack of mathematical tools for solving nonlinear equations, modern plasma physics research relies heavily on computer simulations. Writing computer

codes to solve nonlinear partial differential equations (PDEs) and simulate dynamics of plasmas has become important for understanding the behavior of plasmas and aiding the design of new machines. Computer simulations are widely used in the study of turbulent transport. Based on the analytic methods discussed above, various types of numerical codes have been developed. In this thesis, two major numerical methods are used.

### 2.3.1 Fluid Simulations

A set of PDE's for fluid moments will be solved numerically in a 2D or 3D domain. Fluid simulations are usually fast and global simulations are often performed. However, some important kinetic effects such as Landau damping, wave-particle interactions, are missing in such simulations.

In this thesis, a 2D pseudo-spectral Fortran code called DTRANS is used. In this code a set of PDEs is converted to ordinary differential equations (ODEs) by Fast Fourier Transform (FFT), and the equations are then solved by an ODE solver for the time advancement. The book by Boyd [8] is a comprehensive reference for spectral methods. Another book on spectral methods with a lot of examples in Matlab written by Trefethen [64] is a good introductory reference.

A second fluid code used in the thesis is the BOUT++ code [17], which is a 3D finite differencing fluid simulation framework, written in C++. The code is equipped with MPI parallelization and designed to separate physical equations from numerical schemes.

### 2.3.2 Gyrokinetic Simulations

The gyrokinetic distribution function is numerically solved. Kinetic effects such as velocity-space instabilities and finite gyro-radius effects are included. Due to the high dimensionality, large scale gyrokinetic simulations are very resource consuming (large memory and long running time).

In this thesis, we use the Gyrokinetic Toroidal Code (GTC) [31] to study electron turbulent transport. GTC is a 3D particle-in-cell code designed for simulations of low frequency micro-instabilities and turbulences in tokamak-like plasmas [31]. It uses field-aligned flux coordinates. A $\delta f$ algorithm is used to reduce noise. The GTC code has been highly optimized for parallel computing with both MPI and OpenMP. It is also equipped with the ADIOS library for advanced parallel I/O.

### 2.3.3 Computing Resources

The capability of personal computers has evolved very quickly in the past decades, which makes simulations of physical problems possible even on a laptop. However for realistic plasma simulations nowadays, the supercomputer is still a necessary tool. In this thesis, supercomputers at the Texas Advanced Computing Center (TACC) and the National Energy Research Scientific Computing Center (NERSC) are used to carry out large scale simulations. A large scale simulation task is often divided into a large number of small parallel tasks and distributed over many computing units (cores) to reduce the computing time. Message Passing Interface (MPI) and OpenMP are two major techniques

for parallel computing. MPI libraries provide functional calls for exchanging data and other information between different computing units which in general do not share memory, while OpenMP provides API for shared-memory parallel programming. Sophisticated codes usually take advantage of both techniques.

## 2.4 Turbulent Transport Models

In this section, several well known models for studying turbulence are derived and discussed. These models will be used as base models in Chapter 4 and 5.

In the presence of a strong magnetic field, the velocity of the guiding center of species $s$ is

$$\mathbf{v}_s = \mathbf{v}_E + \mathbf{v}_{ds} + \mathbf{v}_{ps} + \mathbf{v}_{\pi s} + \mathbf{v}_{\parallel s} \tag{2.7}$$

where $s = e, i, z$ for electrons, ions, and impurities, respectively. The drift velocities are defined as follows:

$$\mathbf{v}_E = \frac{c\hat{\mathbf{b}} \times \nabla\phi}{B} \tag{2.8}$$

$$\mathbf{v}_{*s} = \frac{cT_s\hat{\mathbf{b}} \times \nabla n_s}{q_s n_s B} \tag{2.9}$$

$$\mathbf{v}_{ds} = \frac{c\hat{\mathbf{b}} \times \nabla p_s}{q_s n_s B} = (1 + \eta_s)\mathbf{v}_{*s} \tag{2.10}$$

$$\mathbf{v}_{ps} = -\frac{c^2 m_s}{B^2 q_s}\left(\frac{\partial}{\partial t} + \mathbf{v}_s \cdot \nabla\right)\nabla\phi = \frac{c}{B\Omega_s}\frac{d\mathbf{E}}{dt} \tag{2.11}$$

$$\mathbf{v}_{\pi s} = \frac{c\hat{\mathbf{b}} \times \nabla \cdot \pi_s}{q_s n_s B} \tag{2.12}$$

Usually $\mathbf{v}_E$ is of the leading order in magnitude, $\mathbf{v}_{ds}$ could be of the same order as $\mathbf{v}_E$ or smaller, and $\mathbf{v}_{ps}$ is one order of magnitude smaller than $\mathbf{v}_E$.

We will restrict to the electrostatic limit and quasi-neutral limit ($\sum n_s q_s = 0$), unless otherwise specified.

### 2.4.1 Hasegawa-Mima Model

Hasegawa and Mima [27] proposed a simple 2D nonlinear model for turbulence in plasma to explain the spectrum observed in experiments. In the original model, both the magnetic field and the plasma are homogeneous. In the following, we include a background density profile with the density gradient scale length

$$L_n = -\frac{n_0}{\partial n_0/\partial x} \tag{2.13}$$

to study drift waves.

With following assumptions:

1. uniform $\mathbf{B} = B_0\hat{\mathbf{e}}_z$
2. quasi-neutral condition $\delta n_i = \delta n_e = \delta n$
3. adiabatic electron response

$$\frac{\delta n}{n_0} = \frac{e\phi}{T_e} \tag{2.14}$$

4. no ion parallel motion and

5. the parallel (to $\mathbf{B}$) wave number is much smaller than the perpendicular wave number, $k_{\parallel} \ll k_{\perp}$,

the model is simplified to one equation, i.e. the ion continuity equation

$$\frac{\partial \delta n}{\partial t} + (\mathbf{v}_E \cdot \nabla) n_0 + n \nabla_{\perp} \cdot \mathbf{v}_{pi} = 0. \tag{2.15}$$

In this equation, nonlinearity originates from the convective derivative of the polarization drift $\mathbf{v}_{pi}$.

The normalizations adapted by Hasegawa and Mima [27] are

$$\tilde{t} = t\omega_{ci}, \tilde{l} = l/\rho_s, \rho_s = c_s/\omega_{ci}, c_s = \sqrt{T_e/m_i}, \tilde{\phi} = e\phi/T_e \tag{2.16}$$

and the equation can be written as

$$\frac{\partial}{\partial \tilde{t}} \tilde{\phi} + \frac{\rho_s}{L_n} \frac{\partial}{\partial \tilde{y}} \tilde{\phi} - \frac{\partial}{\partial \tilde{t}} \tilde{\nabla}_{\perp}^2 \tilde{\phi} - [\tilde{\nabla}_{\perp} \tilde{\phi} \times \mathbf{z} \cdot \tilde{\nabla}_{\perp}] \tilde{\nabla}_{\perp}^2 \tilde{\phi} = 0 \tag{2.17}$$

or more compactly as

$$\frac{\partial}{\partial \tilde{t}} (\tilde{\phi} - \tilde{\nabla}_{\perp}^2 \tilde{\phi}) = -\frac{\rho_s}{L_n} \frac{\partial}{\partial \tilde{y}} \tilde{\phi} + \left[ \tilde{\phi}, \tilde{\nabla}_{\perp}^2 \tilde{\phi} \right] \tag{2.18}$$

where the Poisson bracket $[,]$ is defined as

$$[f, g] = \frac{\partial f}{\partial x} \frac{\partial g}{\partial y} - \frac{\partial g}{\partial x} \frac{\partial f}{\partial y}. \tag{2.19}$$

Rescaling quantities to drift wave units as follows:

$$\tilde{t} = \bar{t} \frac{L_n}{\rho_s}, \ \tilde{\phi} = \bar{\phi} \frac{\rho_s}{L_n}, \tag{2.20}$$

gives a new normalized equation

$$\frac{\partial}{\partial \bar{t}}(\bar{\phi} - \nabla_\perp^2 \bar{\phi}) = -\frac{\partial}{\partial \tilde{y}}\bar{\phi} + \left[\bar{\phi}, \nabla_\perp^2 \bar{\phi}\right]. \tag{2.21}$$

It can be shown that the following two quantities:

$$W = \frac{1}{2}\int [\phi^2 + (\nabla\phi)^2] dV \tag{2.22}$$

$$U = \frac{1}{2}\int [(\nabla\phi)^2 + (\nabla^2\phi)^2] dV \tag{2.23}$$

are conserved. In $k$-space, the equation reads

$$(1 + k_\perp^2)\frac{\partial}{\partial t}\phi_k = -ik_y\phi_k + [\phi, \nabla_\perp^2\phi]_k \tag{2.24}$$

where $k_\perp^2 = k_x^2 + k_y^2$, and energy conservation can be easily checked

$$\frac{dW}{dt} = \frac{d}{dt}\sum (1 + k_\perp^2)\phi_k\phi_k^* = 0 \tag{2.25}$$

where the Poisson brackets are summed up to a boundary term, which is zero for periodic boundary conditions. And, since there are no dissipative terms, there is no linear growth rate. The frequency, phase velocity and group velocity are given by

$$\omega = \frac{k_y}{1 + k_\perp^2} \tag{2.26}$$

$$\mathbf{v}_p = \frac{\omega}{k}\frac{\mathbf{k}}{k} = \frac{k_y k_x \hat{\mathbf{e}}_x + k_y^2 \hat{\mathbf{e}}_y}{(1 + k_\perp^2)k_\perp^2} \tag{2.27}$$

$$\mathbf{v}_g = \frac{d\omega}{d\mathbf{k}} = \frac{-2k_x k_y \hat{\mathbf{e}}_x + (1 + k_x^2 - k_y^2)\hat{\mathbf{e}}_y}{(1 + k_\perp^2)^2}. \tag{2.28}$$

### 2.4.2 Density-Gradient-Driven Drift Waves

Probably the simplest model to study transport by drift waves is the electrostatic drift wave driven by the density gradient in slab geometry. This type of drift wave is treated in detail in textbooks [e.g. 24, chap. 21], [or 28, chap. 6.6], and is usually called Hasegawa-Wakatani model [25]. In this subsection, I summarize the key results.

The model includes two dynamical equations, the electron continuity equation

$$\frac{\partial \delta n_e}{\partial t} + \mathbf{v}_E \cdot \nabla_\perp n_e + \nabla_\parallel (n_e v_\parallel) = 0 \tag{2.29}$$

and the ion continuity equation

$$\frac{\partial \delta n_i}{\partial t} + \mathbf{v}_E \cdot \nabla_\perp n_i + n_i (\nabla_\perp \cdot \mathbf{v}_{pi}) = 0, \tag{2.30}$$

and two constraints, the equation of electron parallel motion

$$0 = -T_e \nabla_\parallel n_e + n_e e \nabla_\parallel \phi - n_e m_e \nu_e v_\parallel \tag{2.31}$$

and the quasineutral condition $\delta n_e \approx \delta n_i$. Here $\nu_e = \nu_{ei}$ for Coulomb collisions or $\nu_e = k_\parallel v_{te}$ for electron Landau damping.

Assuming

1. homogeneous $\mathbf{B} = B_0 \hat{\mathbf{e}}_z$,
2. cold ions limit $T_i \approx 0$, and
3. no parallel motion of ions.

and normalization as in Eq. (2.16) and Eq. (2.20),

$$\tilde{x} = x\rho_s,\ \tilde{y} = y\rho_s,\ \tilde{z} = zL_n,\ \tilde{t} = t\frac{c_s}{L_n},\ \tilde{\phi} = \frac{e\phi}{T_e}\frac{\rho_s}{L_n},\ \tilde{n} = \frac{\delta_n}{n_0}\frac{\rho_s}{L_n}, \tag{2.32}$$

Eq. (2.29) and Eq. (2.30) become (bars removed)

$$-\frac{\partial}{\partial t}\nabla_\perp^2\phi - \left[\phi, \nabla_\perp^2\phi\right] - \tau\nabla_\parallel^2(\phi - n) = 0 \tag{2.33}$$

$$\frac{\partial}{\partial t}n + \frac{\partial}{\partial y}\phi + [\phi, n] + \tau\nabla_\parallel^2(\phi - n) = 0 \tag{2.34}$$

where

$$\tau = \frac{v_e^2}{\nu_e c_s L_n}. \tag{2.35}$$

The Hasegawa-Mima equation (Eq. (2.21)) can be obtained by summing the two equations above and equating $\phi$ with $n$.

The equations in $\mathbf{k}$-space are

$$\begin{pmatrix} k_\perp^2 & 0 \\ 0 & 1 \end{pmatrix}\frac{\partial \boldsymbol{\phi}}{\partial t} = \mathbf{C}\boldsymbol{\phi} + \mathrm{SNL}[\phi, \boldsymbol{\phi}] \tag{2.36}$$

where

$$\boldsymbol{\phi} = \begin{bmatrix} \phi \\ n \end{bmatrix},\ \mathbf{C} = \begin{bmatrix} -\nu_\parallel & \nu_\parallel \\ -ik_y k_n + \nu_\parallel & -\nu_\parallel \end{bmatrix} \tag{2.37}$$

$k_n = 1$ (retained as a reminder of the background density gradient), $\nu_\parallel = \tau k_\parallel^2$ and

$$\mathrm{SNL}[\phi, \boldsymbol{\phi}] = \begin{bmatrix} \mathrm{snl1}[\phi, \nabla^2\phi]_{\mathbf{k}} \\ -\mathrm{snl2}[\phi, n]_{\mathbf{k}} \end{bmatrix}. \tag{2.38}$$

The energy evolution of the system is

$$\frac{dW}{dt} = \frac{d}{dt}\frac{1}{2}\sum k_\perp^2\phi\phi^* + nn^* \tag{2.39}$$

$$= \frac{d}{dt}\frac{1}{2}\sum\left[-2\nu_\parallel|n - \phi|^2 + \mathrm{Re}(ik_y k_n n\phi^*)\right] \tag{2.40}$$

where the first part in the summation is the dissipative term (energy sink) while the second is the driving term (energy source). If there is no density gradient ($k_n = 0$), the system will relax to the equilibrium of $n = \phi$. One can prove that

$$\frac{dH}{dt} \leq 0, \text{ where } H = \int \frac{|\nabla\phi|^2}{2} + \frac{n^2}{2}. \tag{2.41}$$

Assuming $\phi = \phi_0 \exp(i\mathbf{k}\cdot\mathbf{x} - i\omega t)$, we solve the eigenvalue problem giving the dispersion relation

$$k_\perp^2\omega^2 + i\nu_\parallel[(1+k_\perp^2)\omega - k_y k_n] = 0 \tag{2.42}$$

When the collision rate $\nu_e$ is very small, $\nu_\parallel \to \infty$, and we get quasi-adiabatic response for the electrons.

$$\omega_1 = \frac{k_y k_n}{1+k_\perp^2} + \frac{i}{\nu_\parallel}\left(\frac{k_y k_n}{1+k_\perp^2}\right)^2, \ \omega_2 = -i\nu_\parallel\frac{1+k_\perp^2}{k_\perp^2} \tag{2.43}$$

where $\omega_1$ is the drift wave branch and the dependence of the growth rate on collisions is evident.

When $\nu_e$ is very large, $\nu_\parallel \to 0$, there is no parallel electron motion, and we get the hydrodynamic limit

$$\omega_1 = \frac{-1+i}{\sqrt{2}}\sqrt{\frac{\nu_\parallel k_y k_n}{k_\perp^2}}, \ \omega_2 = \frac{1-i}{\sqrt{2}}\sqrt{\frac{\nu_\parallel k_y k_n}{k_\perp^2}} \tag{2.44}$$

The frequency and growth rate versus $\nu_\parallel/\omega_*$ for the unstable mode $\omega_1$ is plotted in Fig. 2.1, with $k_\perp = k_y$ and $\omega_* = k_y k_n$.

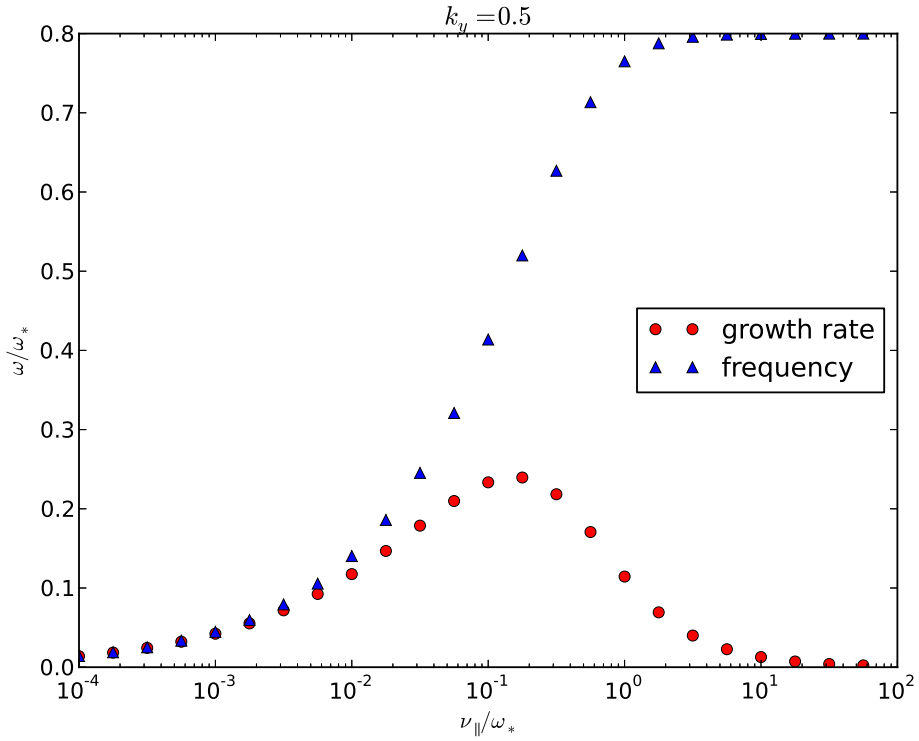


Figure 2.1: The growth rate and frequency of drift waves as a function of $\nu_\parallel$.

### 2.4.3 Ion Temperature Gradient Modes

So far we have considered density gradients as the energy source for instabilities. And the drift wave instability arises due to some dissipation (collision or Landau damping). In tokamaks, however, dissipation is usually weak in the core and the compression caused by temperature fluctuations can also trigger instability. The ion temperature gradient (ITG or $\eta_i$) mode is one of this type of instability. The key parameter for ITG is

$$\eta_i \equiv \frac{\nabla \ln T_i}{\nabla \ln n_i} = \frac{L_{ni}}{L_{Ti}}. \tag{2.45}$$

In order to model ITG, a new field $p_i$ or $T_i$ is needed. The simplest model is

$$\frac{\delta T_i}{T_i} = \frac{k_y}{\omega} \frac{1}{L_{Ti}} \frac{cT_e}{eB} \frac{e\phi}{T_e} \tag{2.46}$$

where the perturbation is driven by $\mathbf{E} \times \mathbf{B}$ convection in a background temperature gradient. A complete equation for $T_s$ is

$$\frac{3}{2} n_s \left( \frac{\partial}{\partial t} + \mathbf{v}_s \cdot \nabla \right) T_s + p_s \nabla \cdot \mathbf{v}_s = -\nabla \cdot q_s - \boldsymbol{\pi} : \nabla \mathbf{v}_s + \sum_{j \neq s} Q_{sj} \tag{2.47}$$

As shown by Weiland [66, chapter 5.11], the contribution of the diamagnetic drift $\mathbf{v}_{ds}$ to the convective derivative and part of $\nabla \cdot (n \mathbf{v}_{ds})$ will cancel the first part of the diamagnetic heat flux

$$\nabla \cdot q_{*i} = -\frac{5}{2} n \mathbf{v}_{*i} \cdot \nabla T_i + \frac{5}{2} n \mathbf{v}_{Di} \cdot \nabla T_i, \tag{2.48}$$

where the term with $v_{Ds}$ originate from the inhomogeneity of the magnetic field (see Chap 4.3.3). Therefore we can eliminate $\mathbf{v}_{ds}$ from $\mathbf{v}_s$ in the temperature equation too. Assuming simple parallel thermal diffusion, we obtain the

equation for $T_i$ in the toroidal geometry

$$\frac{3}{2}n_i\left(\frac{\partial}{\partial t}+\mathbf{v}_E\cdot\nabla\right)T_i+\mathbf{v}_{Di}\cdot\nabla p_i-en_i\mathbf{v}_{De}\cdot\nabla\phi+n_iT_i\nabla_\parallel v_{\parallel i} \\ +\frac{5}{2}n_i\mathbf{v}_{Di}\cdot\nabla T_i=\kappa_\parallel^i\nabla_\parallel^2T_i \qquad (2.49)$$

where $\kappa_\parallel^i=3.9n_iv_{ti}^2/\nu_{ii}$, and $\nu_{ii}$ is the ion-ion collision frequency. Parallel ion motion is included to model ion acoustic waves

$$m_in_i\frac{\partial v_{\parallel i}}{\partial t}=-en_i\nabla_\parallel\phi-T_i\nabla_\parallel n_i-n_i\nabla_\parallel T_i. \qquad (2.50)$$

With adiabatic electron response $\delta n_e/n_e=e\phi/T_e$ and quasi-neutrality condition, the ion continuity equation can be written as

$$\frac{en_e}{T_e}\frac{\partial}{\partial t}\phi+\mathbf{v}_E\cdot\nabla_\perp n_i+n_i(-\frac{e}{T_e}\mathbf{v}_{De}\cdot\nabla\phi+\mathbf{v}_{Di}\cdot\frac{\nabla p_i}{p_i}-\frac{c^2m_i}{eB^2}\frac{d}{dt}\nabla^2\phi \\ +\nabla_\parallel v_{\parallel i})+\frac{c^2\nu_in_i}{eB^2}\nabla^4\phi=0 \qquad (2.51)$$

Linearizing these three equations gives a matrix equation of the form

$$(-i\omega)\mathbf{A}\mathbf{\Phi}=\mathbf{C}\mathbf{\Phi} \qquad (2.52)$$

where

$$\mathbf{A}=\begin{bmatrix}1+k_\perp^2\rho_s^2 & 0 & 0\\ 0 & 1 & 0\\ 0 & 0 & 1\end{bmatrix},\ \Phi=\begin{bmatrix}\frac{e\phi}{T_e}\\ \frac{\delta T_i}{T_i}\\ \frac{v_{\parallel i}}{v_{ti}}\end{bmatrix} \qquad (2.53)$$

and

$$\mathbf{C}=\begin{bmatrix}i\omega_{*i}+i\omega_{De}(1+\tau_i)-\mu_ik_\perp^4\rho_s^2 & i\omega_{De}\tau_i & -ik_\parallel v_{ti}\\ i\omega_{Ti}+\frac{2}{3}[i\omega_{De}(1+\tau_i)] & i\frac{7}{3}\omega_{De}\tau_i-\frac{2}{3}\chi_\parallel^i & -ik_\parallel v_{ti}\\ -ik_\parallel v_{ti}(1+T_e/T_i) & -ik_\parallel v_{ti} & 0\end{bmatrix} \qquad (2.54)$$

A similar toroidal ITG model without parallel ion motion was given by Hu and Horton [40].

### 2.4.4 Trapped Electron Modes

In the toroidal geometry, the toroidal magnetic field ($|\mathbf{B}| \propto 1/R$) on the inner side of the torus is weaker than the field on the outer side, thus forming a magnetic mirror for charge particles. Because of the trapping, electrons cannot move freely along the field line to cancel charge separation, making drift waves unstable. Consider a trapped electron density $n_t = n_{e0} f_t + \delta n_t$, and a passing electron density $n_p = n_{e0} f_p + \delta n_p$, with $f_t + f_p = 1$ where $f_t$ and $f_p$ are the fractions of trapped and passing electrons, respectively. For a large aspect ratio $R_0/a$, the trapped fraction is

$$f_t = \left(1 - \frac{B_{\min}}{B_{\max}}\right)^{1/2} = \sqrt{\frac{2r}{R_0 + r}} \approx \sqrt{2\epsilon}, \tag{2.55}$$

where $\epsilon = r/R$. The equation governing trapped electrons is

$$\frac{\partial n_t}{\partial t} + (\mathbf{v}_E + \mathbf{v}_{De}) \cdot \nabla n_t + n_t(\nabla \cdot \mathbf{v}_E + \mathbf{v}_{De} \cdot \nabla T_e/T_e) = -\nu_{\text{eff}}(n_t - n_{t0}) \tag{2.56}$$

where $\nu_{\text{eff}} = \nu/\epsilon$ is the effective collision rate of trapped electron loss (to passing electrons). If we use the simplest model for temperature fluctuations

$$\frac{dT_e}{dt} \approx 0, \tag{2.57}$$

the responses of trapped and passing electrons are

$$\frac{\delta n_t}{n_e} = \frac{-i\omega_{*e} - i\omega_{De} - i\omega_{Te}\omega_{De}/\omega}{-i\omega + i\omega_{De} + \nu_{\text{eff}}} f_t \frac{e\phi}{T_e} \tag{2.58}$$

$$\frac{\delta n_p}{n_e} = f_p \frac{e\phi}{T_e}. \tag{2.59}$$

The linearized TEM equations are

$$\begin{bmatrix} -f_p & 1 & -1 & 0 \\ -i\omega_{*i} - i\omega_{De} - i\omega k_\perp^2 \rho_s^2 & -i\omega - i\omega_{De}\tau_i & 0 & 0 \\ i(\omega_{*e} + i\omega_{De}) f_t & 0 & -i\omega + i\omega_{De} + \nu_{\text{eff}} & i\omega_{De} \\ i\omega_{*e}\eta_e & 0 & 0 & -i\omega \end{bmatrix} \begin{bmatrix} \frac{e\Phi}{T_e} \\ \frac{\delta n_i}{n_i} \\ \frac{\delta n_t}{n_e} \\ \frac{\delta T_e}{T_e} \end{bmatrix} = \begin{bmatrix} 0 \\ 0 \\ 0 \\ 0 \end{bmatrix} \quad (2.60)$$

which can be reduced to the matrix equation

$$(-i\omega)\mathbf{A}\mathbf{\Phi} = \mathbf{C}\mathbf{\Phi} \quad (2.61)$$

where

$$\mathbf{A} = \begin{bmatrix} k_\perp^2 \rho_s^2 & 1 & 0 \\ -f_p & 1 & 0 \\ 0 & 0 & 1 \end{bmatrix}, \Phi = \begin{bmatrix} \frac{e\phi}{T_e} \\ \frac{\delta n_i}{n_i} \\ \frac{\delta T_e}{T_e} \end{bmatrix} \quad (2.62)$$

and

$$\mathbf{C} = \begin{bmatrix} i\omega_{*i} + i\omega_{De} & i\omega_{De}\tau_i & 0 \\ -i\omega_{*e} f_t - i\omega_{De}(f_t - f_p) + f_p \nu_{\text{eff}} & -i\omega_{De} - \nu_{\text{eff}} & -i\omega_{De} \\ i\omega_{*e}\eta_e & 0 & 0 \end{bmatrix}. \quad (2.63)$$

A simplified version of TEM without $T_e$ fluctuations can be easily obtained by removing the third row and the third column in the equations above.

### 2.4.5 Electron Temperature Gradient Modes

The fluid equations used to model the electrostatic electron temperature gradient (ETG) mode [33] are the electron continuity equation

$$\frac{\partial}{\partial t}\delta n_e + \mathbf{v}_E \cdot \nabla_\perp n_e + n_e \nabla_\perp \cdot \mathbf{v}_{pe} + \nabla_\parallel (n_e v_\parallel) = 0 \quad (2.64)$$

the electron parallel momentum equation

$$(\frac{\partial}{\partial t} + \mathbf{v}_E \cdot \nabla_\perp)v_\parallel + \frac{\nabla_\parallel p_e}{m_e n_e} - \frac{e}{m_e}\nabla_\parallel \phi + \nu_e v_\parallel = 0, \tag{2.65}$$

the thermal balance equation

$$\frac{\partial}{\partial t}T_e + \mathbf{v}_E \cdot \nabla T_e + (\Gamma - 1)T_e(\nabla_\perp \cdot \mathbf{v}_{pe} + \nabla_\parallel v_\parallel) = \kappa_\parallel \nabla_\parallel^2 T_e, \tag{2.66}$$

where $\Gamma = 5/3$,

$$\kappa_\parallel \nabla_\parallel^2 T_e = \begin{cases} -\dfrac{\alpha v_e^2}{\nu_e} k_\parallel^2 \delta T_e, & \text{when } k_\parallel^2 v_e^2 \le \nu_e^2 \\ -\alpha v_e |k_\parallel| \delta T_e, & \text{when } k_\parallel^2 v_e^2 > \nu_e^2 \end{cases}, \tag{2.67}$$

and $\alpha = 3.16$, and Poisson's equation

$$\delta n_e = \frac{\nabla^2 \phi}{4\pi e} + Z\delta n_i. \tag{2.68}$$

We consider a slab model with homogeneous magnetic field and assume a quasi-adiabatic ion response

$$\delta n_i \approx -n_i Z(1 - i\delta)e\phi/T_i \tag{2.69}$$

which leads to

$$\delta n_e/n_e = -A_p e\phi/T_e \tag{2.70}$$

where

$$A_p = Z^2 \frac{T_e}{T_i}(1 - i\delta) + k^2 \lambda_D^2. \tag{2.71}$$

Using the following normalization:

$$\tilde{n} = \frac{\delta n_e}{n_e}, \tilde{t} = t\omega_{ce}, \tilde{l} = l/\rho_e, \tilde{v}_\parallel = \frac{v_\parallel}{v_{te}}, \tilde{\phi} = \frac{e\phi}{T_e}, \tilde{T_e} = \frac{\delta T_e}{T_e}, \tilde{\kappa}_\parallel = \frac{\kappa_\parallel}{\rho_e v_{te}} \tag{2.72}$$

the normalized equations are

$$-A_p\frac{\partial}{\partial\tilde{t}}\tilde{\phi}+\frac{\rho_e}{L_n}\frac{\partial}{\partial\tilde{y}}\tilde{\phi}+\frac{\partial}{\partial\tilde{t}}\tilde{\nabla}_\perp^2\tilde{\phi}+\left[\tilde{\phi},\tilde{\nabla}_\perp^2\tilde{\phi}\right]+\tilde{\nabla}_\parallel\tilde{v}_\parallel=0 \tag{2.73}$$

$$\frac{\partial}{\partial\tilde{t}}\tilde{v}_\parallel-A_p\tilde{\nabla}_\parallel\tilde{\phi}+\frac{\nu_e}{\omega_{ce}}\tilde{v}_\parallel+\tilde{\nabla}_\parallel\tilde{T}_e+\left[\tilde{\phi},\tilde{v}_\parallel\right]=0 \tag{2.74}$$

$$\frac{\partial}{\partial\tilde{t}}\tilde{T}_e+\frac{\rho_e}{L_{Te}}\frac{\partial}{\partial\tilde{y}}\tilde{\phi}+\left[\tilde{\phi},\tilde{T}_e\right]+(\Gamma-1)\tilde{\nabla}_\parallel\tilde{v}_\parallel+\tilde{\kappa}_\parallel\tilde{\nabla}_\parallel^2\tilde{T}_e=0. \tag{2.75}$$

Since $\rho_e/L_n$ is usually very small, we can rescale all quantities as

$$\tilde{t}=\bar{t}\frac{L_n}{\rho_e},\ \tilde{\phi}=\bar{\phi}\frac{\rho_e}{L_n},\ \tilde{v}_\parallel=\bar{v}_\parallel\frac{\rho_e}{L_n},\ \tilde{T}_e=\bar{T}_e\frac{\rho_e}{L_n},\ \tilde{\nabla}_\parallel=\bar{\nabla}_\parallel\frac{\rho_e}{L_n},\ \tilde{\kappa}_\parallel=\bar{\kappa}_\parallel\frac{L_n}{\rho_e} \tag{2.76}$$

and obtain a set of equations suitable for computer simulations

$$-A_p\frac{\partial}{\partial\bar{t}}\bar{\phi}+\frac{\partial}{\partial\bar{y}}\bar{\phi}+\frac{\partial}{\partial\bar{t}}\bar{\nabla}_\perp^2\bar{\phi}+\left[\bar{\phi},\bar{\nabla}_\perp^2\bar{\phi}\right]+\bar{\nabla}_\parallel\bar{v}_\parallel=0 \tag{2.77}$$

$$\frac{\partial}{\partial\bar{t}}\bar{v}_\parallel-A_p\bar{\nabla}_\parallel\bar{\phi}+\frac{\nu_e L_n}{v_{te}}\bar{v}_\parallel+\bar{\nabla}_\parallel\bar{T}_e+\left[\bar{\phi},\bar{v}_\parallel\right]=0 \tag{2.78}$$

$$\frac{\partial}{\partial\bar{t}}\bar{T}_e+\eta_e\frac{\partial}{\partial\bar{y}}\bar{\phi}+\left[\bar{\phi},\bar{T}_e\right]+(\Gamma-1)\bar{\nabla}_\parallel\bar{v}_\parallel+\bar{\kappa}_\parallel\bar{\nabla}_\parallel^2\bar{T}_e=0 \tag{2.79}$$

where $\eta_e=\nabla(\ln T_e)/\nabla(\ln n_e)$.

By introducing a three component vector field

$$\boldsymbol{\phi}=(\phi_1,\phi_2,\phi_3)^T=(L_n/\rho_e)(e\phi/T_e,v_{\parallel e}/v_{te},\delta T_e/T_e)^T, \tag{2.80}$$

the equations in **k**-space can be written in matrix form as

$$\begin{pmatrix} A_p+k_\perp^2\rho_e^2 & 0 & 0\\ 0 & 1 & 0\\ 0 & 0 & 1\end{pmatrix}\frac{\partial\boldsymbol{\phi}}{\partial t}=\mathbf{C}\boldsymbol{\phi}+\mathrm{SNL}[\phi_1,\boldsymbol{\phi}] \tag{2.81}$$

where $A_p = Z^2 \frac{T_e}{T_i}(1 - i\delta) + k^2\lambda_D^2$,

$$\mathbf{C} = \begin{bmatrix} ik_y\rho_e & ik_\parallel L_n & 0 \\ ik_\parallel L_n A_p & -\nu_e L_n/v_{te} & -ik_\parallel L_n \\ -ik_y\rho_e\eta_e & -(\Gamma-1)ik_\parallel L_n & -\bar{\kappa}(k_\parallel L_n)^2 \end{bmatrix} \tag{2.82}$$

and

$$\mathrm{SNL}[\phi_1, \boldsymbol{\phi}] = \begin{bmatrix} \mathrm{snl1}[\phi_1, \nabla^2\phi_1]_{\mathbf{k}} \\ -\mathrm{snl2}[\phi_1, \phi_2]_{\mathbf{k}} \\ -\mathrm{snl3}[\phi_1, \phi_3]_{\mathbf{k}} \end{bmatrix} \tag{2.83}$$

where we introduce three parameters $snl1$, $snl2$, and $snl3$ (equal to either 1 or 0) to turn on or off the nonlinear effect.

We can check energy conservation by calculating the following quantities:

$$\begin{aligned} \frac{dW_1}{dt} &= \frac{1}{2}(A_p + k_\perp^2\rho_e^2)A_p\frac{\partial}{\partial t}\phi_1^*\phi_1 \\ &= \frac{1}{2}\sum_{\mathbf{k}} A_p(ik_y\rho_e\phi_1^*\phi_1 + C.C.) + P_{12} \end{aligned} \tag{2.84}$$

$$\frac{dW_2}{dt} = \frac{1}{2}\frac{\partial}{\partial t}\phi_2^*\phi_2 = P_{21} - \frac{\nu_e L_n}{v_{te}}\sum_{\mathbf{k}}\phi_2^*\phi_2 + P_{23} \tag{2.85}$$

$$\begin{aligned} \frac{dW_3}{dt} &= \frac{1}{2}\frac{1}{\Gamma-1}\frac{\partial}{\partial t}\phi_3^*\phi_3 \\ &= \frac{1}{2}\frac{1}{\Gamma-1}\sum_{\mathbf{k}}(ik_y\rho_e\eta_e\phi_1^*\phi_3 + C.C.) + P_{32} \\ &\quad -\frac{\bar{\kappa}(k_\parallel L_n)^2}{\Gamma-1}\sum_{\mathbf{k}}\phi_3^*\phi_3 \end{aligned} \tag{2.86}$$

where

$$P_{12} = \frac{1}{2}\sum_{\mathbf{k}} A_p(ik_\parallel L_n \phi_1^* \phi_2 + C.C.) \tag{2.87}$$

$$P_{21} = \frac{1}{2}\sum_{\mathbf{k}} A_p(ik_\parallel L_n \phi_2^* \phi_1 + C.C.) \tag{2.88}$$

$$P_{23} = \frac{1}{2}\sum_{\mathbf{k}} (ik_\parallel L_n \phi_2^* \phi_3 + C.C.) \tag{2.89}$$

$$P_{32} = \frac{1}{2}\sum_{\mathbf{k}} (ik_\parallel L_n \phi_3^* \phi_2 + C.C.) \tag{2.90}$$

so $P_{12} = -P_{21}$ and $P_{23} = -P_{32}$. Energy is conserved if dissipative terms and linear drive terms are turned off.

### 2.4.6 Drift Waves in Earth's ionosphere and magnetosphere

Drift waves are universal in inhomogeneous plasmas. The plasma surrounding the Earth is a good stage for drift waves. Here, I will show equations for drift waves in the ionosphere where plasma density varies with height. The resulting turbulence will affect the electromagnetic waves (e.g. GPS signals) traveling through the ionosphere. Here I will show an example in the E-layer where ions are unmagnetized due to the high collision rate with neutral particles and electrons remain magnetized. Therefore, the drift waves are on the electron scale. With $T_e = 300\text{K}$, $B = 0.3\,\text{G}$, the electron gyroradius is $\rho_e \approx 1.3\,\text{cm}$.

We use a slightly different coordinate system from previous subsections: the $x$-axis points to the west, $y$ points up, and $z$ points to the north, the direction of magnetic field in the earth's rest frame. This is the case when we

stand on the magnetic equator. The gradient of density $n_e$ is then in the $y$ direction. In addition, there is a strong eastward zonal wind in the E-layer, $\mathbf{v}_n = -v_0\hat{\mathbf{e}}_x$.

The three dynamical equations we need are the electron continuity equation

$$\frac{\partial \delta n_e}{\partial t} + \mathbf{v}_E \cdot \nabla(n_0 + \delta n_e) + \nabla \cdot (n_e \mathbf{v}_{pe}) + \nabla_\parallel (n_e v_{\parallel e}) = 0 \tag{2.91}$$

the ion continuity equation

$$\frac{\partial \delta n_i}{\partial t} + \nabla \cdot (n_i \mathbf{v}_i) = 0 \tag{2.92}$$

and the ion equation of motion

$$m_i \left( \frac{\partial \mathbf{v}_i}{\partial t} + \mathbf{v}_i \cdot \nabla \mathbf{v}_i \right) = e\mathbf{E} - \frac{\nabla p_i}{n_i} - m_i \nu_{in}(\mathbf{v}_i - \mathbf{v}_n) \tag{2.93}$$

where $\nu_{in}$ is the collision rate between ions and neutrals. For the parallel motion of electrons, from the dynamical equation

$$m_e \frac{dv_{e\parallel}}{dt} = e\nabla_\parallel \phi - \frac{\nabla_\parallel p_e}{n_e} - m_e \nu_{en}(v_{e\parallel} - v_{n\parallel}) \tag{2.94}$$

one can derive

$$v_{e\parallel} = \frac{T_e}{m_e \nu_{en}} \nabla_\parallel \left( \frac{e\phi}{T_e} - \frac{\delta n_e}{n_e} \right) \tag{2.95}$$

when the collision frequency is much larger the dynamical frequency, i.e. $\nu_{en} \gg \omega$.

Now we transform to the reference frame of the neutral wind. According to the special relativity, the new electromagnetic fields are

$$\mathbf{E}' = \gamma\left(\mathbf{E} + \frac{\mathbf{v}_n \times \mathbf{B}}{c}\right) \tag{2.96}$$

$$\mathbf{B}' = \gamma\left(\mathbf{B} - \frac{\mathbf{v}_n \times \mathbf{E}}{c}\right). \tag{2.97}$$

It can be shown that the $E \times B$ drift is invariant under this transformation. For $v_n \ll c$, one can approximate the fields as

$$\mathbf{E}' \approx \mathbf{E} + \frac{\mathbf{v}_n \times \mathbf{B}}{c}, \tag{2.98}$$

$$\mathbf{B}' \approx \mathbf{B}. \tag{2.99}$$

For example, given $v_n/c \sim 10^{-6}$ and $B = 1$ Gauss, $\Delta E = E' - E \sim 10$ mV/m. While given $E \sim 10$ mV/m, $\Delta B = B' - B \sim 10^{-12}$ Gauss, is negligible. Other terms in the continuity equation and the momentum equation are invariant under the Galilean transformation.

The ion equation of motion (a vector equation) in this frame can be further simplified if we assume

$$\mathbf{v}_i' = \mathbf{v}_i - \mathbf{v}_n = -\nabla\chi \tag{2.100}$$

where only compressional ion motions (sound wave like motion) are allowed and no vortex is formed. Thus we have(from now on the "′" will be dropped)

$$\mathbf{v}_i \cdot \nabla\mathbf{v}_i = \frac{1}{2}\nabla(\mathbf{v}_i \cdot \mathbf{v}_i) = \frac{1}{2}\nabla(\nabla\chi \cdot \nabla\chi) \tag{2.101}$$

$$-\nabla \cdot (n\mathbf{v}_i) = \nabla n_0 \cdot \nabla\chi + n_0\nabla^2\chi + \nabla\delta n \cdot \nabla\chi + \delta n\nabla^2\chi \tag{2.102}$$

and Eq. (2.93) reads

$$\frac{\partial \chi}{\partial t} - \frac{1}{2}\nabla\chi \cdot \nabla\chi = \frac{e}{m_i}(\phi_0 + \phi) + \frac{T_i}{m_i}\ln n_i - \nu_{in}\chi \tag{2.103}$$

where a $\nabla$ has been removed from both sides of the equation, $\phi_0$ is the background potential, and $\ln n_i = \ln n_0 + \ln(1 + \delta n/n_0)$.

Equations (2.91), (2.92) and (2.95) can be combined into the vortex equation

$$\begin{aligned}\frac{c^2 m_e}{eB^2}\left(\frac{\partial}{\partial t}\nabla_\perp^2\phi + \frac{c}{B}[\phi, \nabla_\perp^2\phi]\right) + \frac{c}{B}\frac{\partial\phi}{\partial x}\frac{dn_0}{dy} - \frac{c}{B}\frac{\partial\phi_0}{\partial y}\frac{\partial\delta n}{\partial x} \\ + \frac{c}{B}[\phi, \delta n] + \frac{n_0 T_e}{m_e\nu_{en}}\nabla_\parallel^2\left(\frac{e\phi}{T_e} - \frac{\delta n}{n_0}\right) + \frac{dn_0}{dy}\frac{\partial\chi}{\partial y} + n_0\nabla^2\chi \\ + \nabla\delta n \cdot \nabla\chi + \delta n\nabla^2\chi = 0\end{aligned} \tag{2.104}$$

Upon normalization of the independent variable with drift wave units

$$x = \bar{x}\rho_s,\ y = \bar{y}\rho_s,\ z = \bar{z}L_n,\ t = \bar{t}L_n/v_e \tag{2.105}$$

and the fields as

$$\bar{n} = \frac{\delta n}{n_0}\frac{L_n}{\rho_e} \tag{2.106}$$

$$\bar{\phi} = \frac{e\phi}{T_e}\frac{L_n}{\rho_e} \tag{2.107}$$

$$\bar{\chi} = \frac{\chi}{\rho_e^2 v_e/L_n}\frac{L_n}{\rho_e} \tag{2.108}$$

the vortex Eq. (2.104) in the dimensionless form (with bars removed) becomes:

$$\begin{aligned}\frac{\partial}{\partial t}\nabla_\perp^2\phi + [\phi, \nabla_\perp^2\phi] + \frac{\partial\phi}{\partial x} - \frac{\partial\phi_0}{\partial y}\frac{\partial n}{\partial x} + [\phi, n] + \frac{1}{\nu_{en}}\nabla_\parallel^2(\phi - n) \\ + \nabla^2\chi + \frac{\rho_e}{L_n}\left(\frac{\partial\chi}{\partial y} + \nabla n \cdot \nabla\chi + n\nabla^2\chi\right) = 0,\end{aligned} \tag{2.109}$$

where terms in the second line are of magnitude of $\rho_e/L_n$ smaller. The normalized ion continuity equation is

$$\frac{\partial n}{\partial t} - \frac{\rho_e}{L_n}\nabla n \cdot \nabla\chi - \nabla^2\chi = 0 \tag{2.110}$$

and the normalized ion equation of motion reads

$$\frac{\partial \chi}{\partial t} - \frac{1}{2}\frac{\rho_e}{L_n}\left|\nabla\chi\right|^2 = c_s^2(\phi_0 + \phi) + v_i^2(\ln n_0 + n) - \nu_{in}\chi, \tag{2.111}$$

where velocities are normalized by $\rho_e v_e/L_n$. Notice that the equilibrium will require terms for which $\phi_0$ and $n_0$ cancel.

Equations (2.109), (2.110), and (2.111) form a complete set of equations for modeling drift waves in the E-layer.

Introducing a three component vector field

$$\boldsymbol{\phi} = (\phi_1, \phi_2, \phi_3)^T = (\bar{\phi}, \bar{n}, \bar{\chi})^T \tag{2.112}$$

in $\mathbf{k}$-space these equations become

$$\begin{pmatrix} k_\perp^2 & 0 & 0 \\ 0 & 1 & 0 \\ 0 & 0 & 1 \end{pmatrix} \frac{\partial \boldsymbol{\phi}}{\partial t} = \mathbf{C}\boldsymbol{\phi} + \mathrm{SNL} \tag{2.113}$$

where

$$\mathbf{C} = \begin{bmatrix} -ik_x - \nu_\parallel & ik_y\phi_0 + \nu_\parallel & -k^2 \\ 0 & 0 & -k^2 \\ c_s^2 & v_i^2 & -\nu_{in} \end{bmatrix} \tag{2.114}$$

and

$$\mathrm{SNL} = \begin{bmatrix} \mathrm{snl1}[\phi_1, \nabla^2\phi_1]_{\mathbf{k}} + \mathrm{snl2}[\phi_1, \phi_2]_{\mathbf{k}} \\ \mathrm{snl3}(\nabla\phi_2 \cdot \nabla\phi_3)_{\mathbf{k}} \\ \mathrm{snl4}(\nabla\phi_3 \cdot \nabla\phi_3)_{\mathbf{k}} \end{bmatrix}. \tag{2.115}$$

Here we denote nonlinear effects by $snl1$, $snl2$, $snl3$ and $snl4$.

| Inside | Outside |
|---|---|
| $n = 200$ cm$^{-3}$ | $n = 10$ cm$^{-3}$ |
| $\rho_i = 3 \times 10^4$ cm | |
| $B = 500$ nT (at $4R_E$) | |
| $T_i = T_e = 1$ eV | |
| $L_n = 0.1R_E$ | |
| $k_\parallel = \pi/L_\parallel \approx 5 \times 10^{-10}$ cm | |

Table 2.1: Typical parameters inside and outside the plasmapause. The location of the plasmapause is at $\sim 4R_E$.

Another place where drift waves could be important is in the plasmapause. The dense and cold plasma in the plasmasphere terminated at the sharp boundary that occurs at $\sim 3-5R_E$, where the density drops from $\sim 10^3$ to a few electrons per cubic centimeter (Table 2.1). The possibility of drift wave instability at the plasmapause was first studied by Hasegawa [26]. Typical parameters are shown in Table 2.1. The drift wave linear frequency and growth rate are (in CGS units)

$$\omega_* \sim 3 \times 10^3 k_\perp, \quad \gamma \sim \omega_*; \tag{2.116}$$

with $k_\perp \rho_i \leq 1$, the frequency is $\sim 10^{-2}$ rad/s. However, direct evidence of drift waves at the plasmapause is sparse, owing to their low frequency and small spatial scales. A review of the plasmapause data is given in Frey [19]. The drift wave instability has also been proposed to explain large-scale auroral undulations observed by IMAGE satellite [46].

# Chapter 3

# Particle Transport in Mirror Machines

## 3.1 Gamma-10 at the University of Tsukuba

Although tokamaks are the dominant configurations for magnetic fusion, linear mirror machines have several advantages over the toroidal fusion systems:

- No toroidal curvature. The linear magnetic geometry avoids many plasma instabilities induced by the curvature of the magnetic field.
- Weak internal current. Many instabilities associated with plasma currents, like kink modes, tearing modes, etc. do not exist in linear machines. In mirror machines all The magnetic fields are generated by external coils.
- Natural open divertor. Linear machines have two ends serving as natural way of diverting plasmas, which is convenient to convert fusion energy into electricity–the ultimate goal of fusion research.
- Easy control of the radial electric field. It has been confirmed that the radial $E_r$-shear can suppress turbulence and thus enhance confinement.

In mirror machines, the radial potential profile can be modified by selectively heating electrons at the desired radial position.

The linear machine has its disadvantages too. The end loss is a major concern for plasma confinement. Historically, the United States pursued linear machines in the 1970s and dropped the approach in the 1980s to concentrate on the tokamak approach to fusion power.

Gamma-10 is a tandem mirror system located in the Plasma Research Center at University of Tsukuba, Japan. A schematic of Gamma-10 machine is shown in Fig. 3.1. The 27m long mirror machine has a central cell of 6m length, and several anchor and plug coils to minimize the end loss. We focus on the radial particle transport in the central cell and assume a homogeneous **B** field.

## 3.2 Drift Waves in the Mirror Machine

In this chapter we focus on the radial loss of plasma due to drift wave turbulences. A simple model for the density $n(r)$ in the linear machine is

$$n(r) = n_0 \exp(-r^2/2a^2) \tag{3.1}$$

and the drift frequency is independent of radius $r$

$$\omega_{*e} = \frac{k_y T_e}{eBL_n} = \frac{T_e}{eB}\frac{m}{a^2}, \tag{3.2}$$

where $L_n = -n/\nabla n$ and $k_y = m/r$.

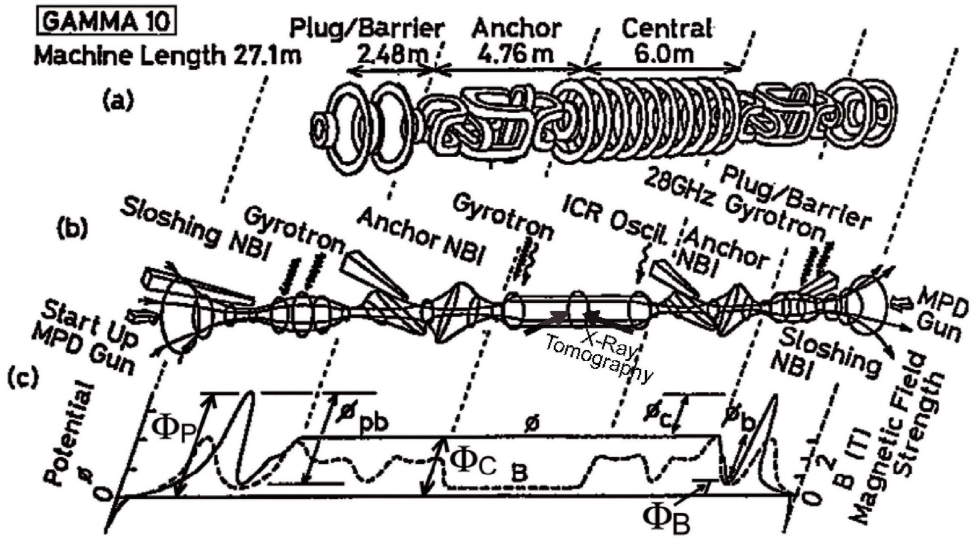


Figure 3.1: A schematic of the Gamma-10 machine: (a) the coils that generate confining magnetic field, (b) the magnetic flux surface, and (c) the electric potential $\Phi$ and the magnetic field $B$ on the axis.

## 3.3 Particle Transport in Gamma-10

Now we study the particle transport in the presence of turbulent drift waves in Gamma-10 [35]. The radial profiles of measured electric potential $\Phi$ are shown in Fig. 3.2. Filled circles and the solid line represent the profile of $\Phi$ with the injection of electron cyclotron heating and hollow circles and the dashed line shows the normal profile without any heating. Experiments showed that the turbulent transport was greatly reduced by the injection and a transport barrier is formed [12].

Particle guiding center motion in cylindrical devices like Gamma-10 can

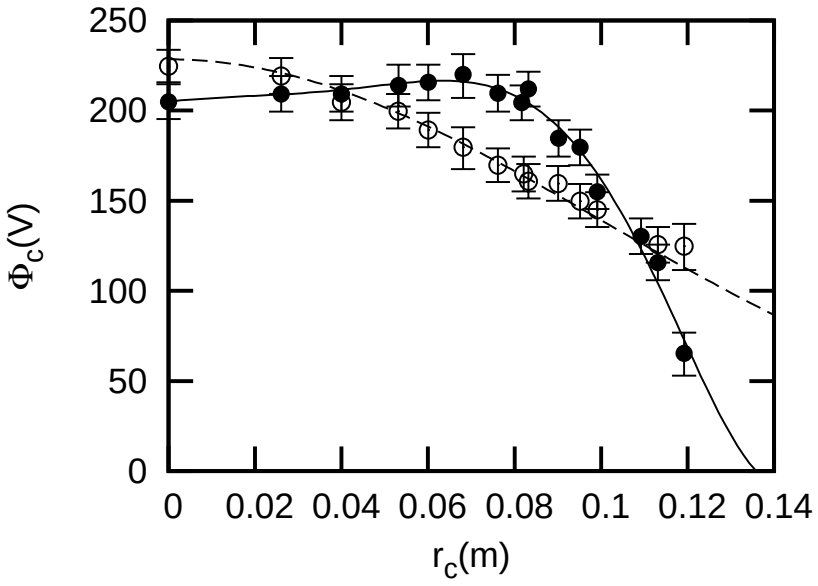


Figure 3.2: Radial profile of the electric potential $\Phi$ measured in Gamma-10 (Reproduced from Ref. [12].)

be described by

$$\frac{d\vec{x}}{dt} = \frac{\hat{e}_z \times \nabla\Phi}{B}, \text{ or } (\dot{r}, r\dot{\theta}, \dot{z}) = (\frac{-1}{rB}\frac{\partial\Phi}{\partial\theta}, \frac{1}{B}\frac{\partial\Phi}{\partial r}, 0). \tag{3.3}$$

Upon defining $I \equiv r^2/2$ and $H \equiv \Phi/B$, one find the equations of motion are Hamiltonian

$$\frac{d\theta}{dt} = \frac{\partial H}{\partial I}, \tag{3.4}$$

$$\frac{dI}{dt} = -\frac{\partial H}{\partial \theta}. \tag{3.5}$$

The total electric field consist of the background field and the fluctuating part from drift waves

$$\Phi(r,\theta) = \Phi_0(r) + \sum_m \phi_m \cos(m\theta - \omega_m t + \xi_m) \tag{3.6}$$

where $\omega_m = \omega_{*e}$ is the drift wave frequency for mode $m$, $\phi_m$ is the wave amplitude, and $\xi_m$ is the relative phase. Given the spectrum $\phi_m$ and phases $\xi_m$, the particle dynamics is determined. However, obtaining the spectrum, which requires nonlinear simulations or sophisticated measurements, is not an easy task.

Instead, we examine an over-simplified case in which we assume an infinite coherent spectrum for drift waves, and it turns out that the set of ODEs are reduced to a map. Before doing this reduction, assume $\phi$, $I$, $\omega_m$ and $H$ are normalized as

$$\Phi \to e\Phi/T_e,\ I \to r^2/2a^2,\ \omega_m \to m, H \to HeB/T_e. \tag{3.7}$$

Summing over all waves with equal amplitude and phase, and different frequencies $n\omega_m$ where $n \in \mathbb{Z}$, the normalized Hamiltonian becomes

$$H(\theta, I, t) = \Phi_0(I) + \sum_{n=-\infty}^{\infty} \phi_m \cos(m\theta - nmt). \tag{3.8}$$

Using the following:

$$\begin{aligned} \sum_{n=-\infty}^{\infty} \cos(m\theta - nmt) &= \cos(m\theta) \sum_{n=-\infty}^{\infty} \cos(nmt) & (3.9) \\ &= \cos(m\theta) \sum_{n=-\infty}^{\infty} \delta(t - \frac{2n\pi}{m}), & (3.10) \end{aligned}$$

and the property of the $\delta$-function enables us to obtain a "kick" map:

$$\begin{aligned} I_{n+1} &= I_n + m\phi_m \sin(m\theta_n) & (3.11) \\ \theta_{n+1} &= \theta_n + \frac{d\Phi_0(I_{n+1})}{dI} & (3.12) \end{aligned}$$

where $\theta_n$ is defined at $t = t_n = 2n\pi/\omega_m$ and $I_n$ is defined during $t_{n-1} < t < t_n$.

Two models for the electric potential $\Phi$ representing the experiments are the $E_r$-positive (monotonic potential) model

$$\Phi_1(I) = -0.3I^2 + 0.56, \tag{3.13}$$

and the $E_r$-reversed (twist) model

$$\Phi_2(I) = -0.8I(I - 0.5) + 0.51 \tag{3.14}$$

shown in Fig. 3.3. We also consider a third "nontwist" model with

$$\Phi_3(I) = -I(I - 0.25)(I - 0.5) + 0.51, \text{ where } \frac{d\Phi^2}{dI^2} = 0 \text{ at } I = 0.17. \tag{3.15}$$

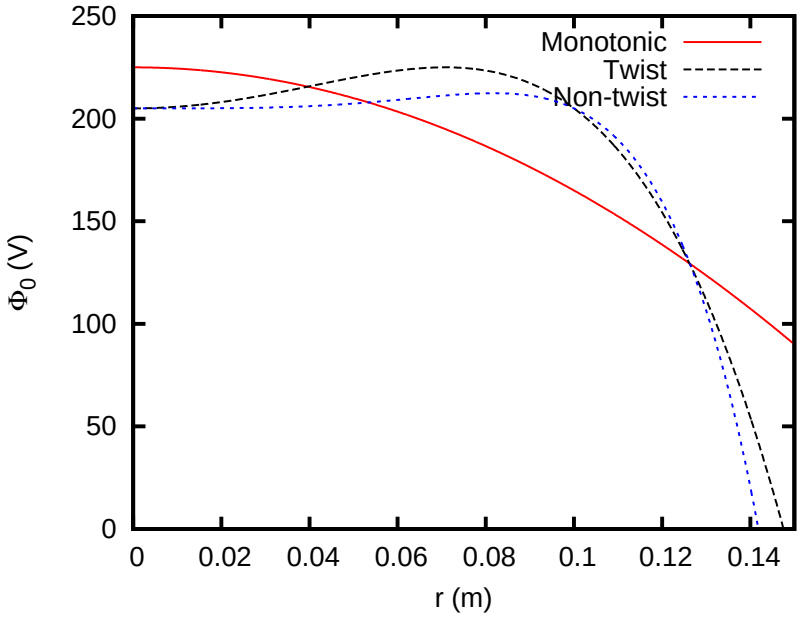


Figure 3.3: Models for the electric potential $\Phi$ in Gamma-10

This name is given due to the fact that the twist condition $dH^2/dI^2 \neq 0$, which is a prerequisite for many theorems (e.g. KAM and Poincaré-Birkhoff), is violated in a generic way [14]. The $I - \theta$ maps for these three models are shown in Fig. (3.4)-(3.6). For the $E_r$-reversed potential, a transport barrier is formed at $I = 0.25$ where $dH/dI = 0$. The behavior of particle in the nontwist map is quite different from the other two maps. Even for small amplitude drift waves $\phi_m = 0.01$, particles are not well confined.

Marcus et al. [51] study the reduction of particle transport driven by drift waves in sheared flows. A similar Hamiltonian structure was obtained with two drift waves, the minimum number necessary for chaos. It was shown that a robust barrier is formed near the location where the shear vanishes.

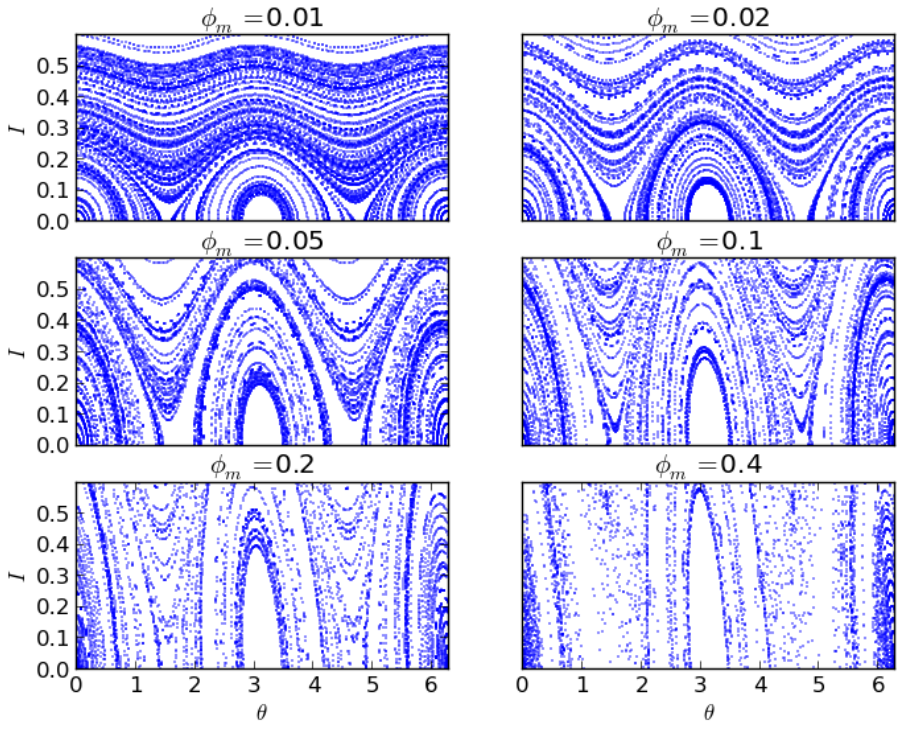


Figure 3.4: $I - \theta$ phase space map for the monotonic potential $\Phi_1$, with $e\phi_m/T_e = 0.01, 0.02, 0.05, 0.1, 0.2, 0.4$, using Eqs. (3.11)-(3.12).

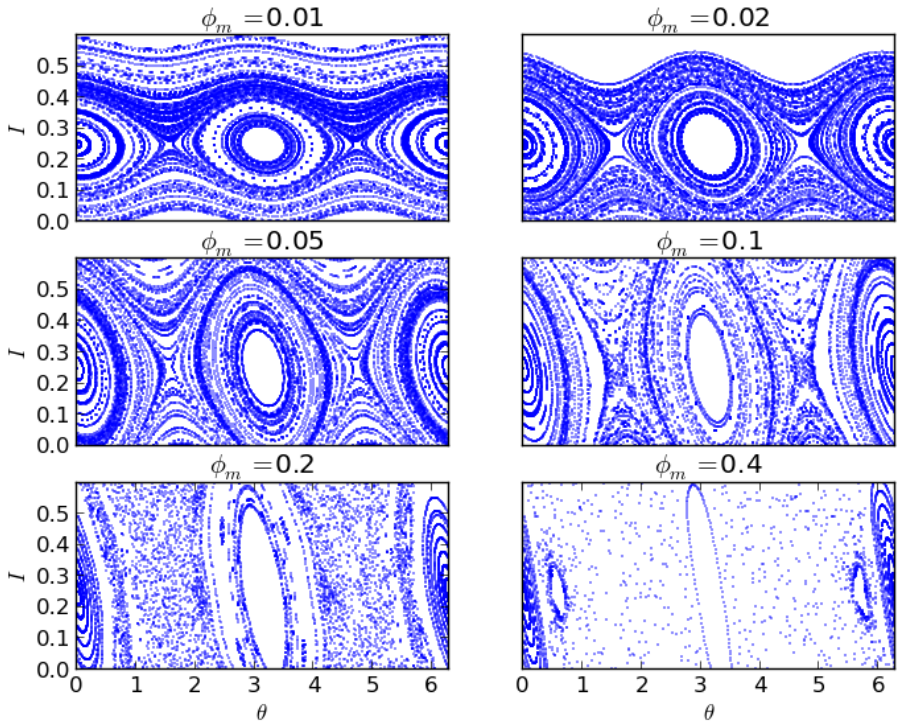


Figure 3.5: $I - \theta$ phase space map for the $E_r$-reversed potential $\Phi_2$.

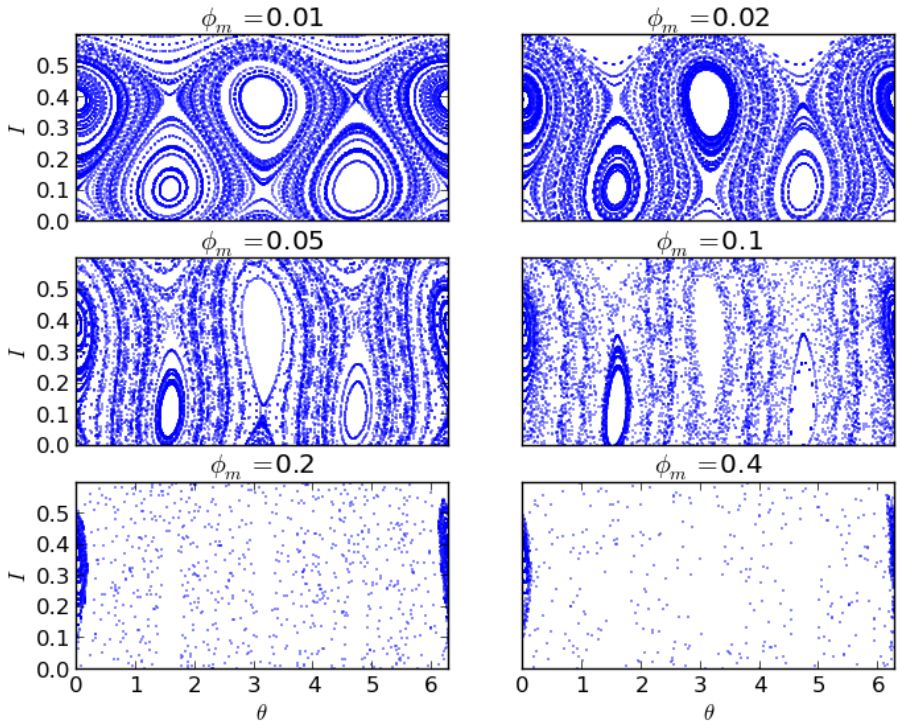


Figure 3.6: $I - \theta$ phase space map for the nontwist potential $\Phi_3$.

The reduction of turbulent transport by reversed $E_r$-shear is observed in many experiments, e.g. TCABR [51], LAPD [56], Helimak [63], GAMMA-10 [11] etc.

# Chapter 4

# Impurity Transport in Tokamaks

## 4.1 Impurity Transport

Turbulent transport from drift waves is a key problem for fusion physics across all magnetic confinement geometries. In contrast to particle and heat transport of electrons and main ions, the understanding of impurity transport is limited. Impurity accumulation in the core leads to fuel dilution and radiation losses, potentially degrading the performance of fusion reactors. From this perspective, the use of light impurities, including helium(He), beryllium(Be), boron(B) and carbon(C), are better choices for impurity content of the burning plasma when such choices are practical. In JET, enhanced performance with low effective charge $Z_{\text{eff}} < 2$ was obtained by changing the plasma facing components (PFC) from graphite to beryllium as shown by Dietz and Team [16]. For basically this reason, the choice of the plasma facing components in the ITER machine is beryllium [10], an alkaline-earth metal with Z=4, A=9 and a melting point of $\sim 1300^{\circ}$ C. On the other hand, the injection of argon at the edge of the plasma is widely considered as a method to create an edge localized radiation belt for continuous heat exhaust that reduces the thermal load on the divertor plates[50]. This favorable role of impurities must be balanced with possible accumulation of impurities in the core plasma. Therefore,

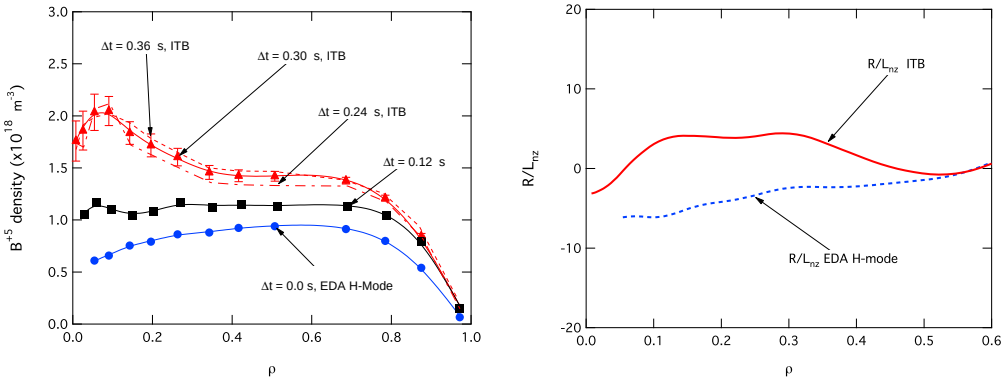


(a) (b)

Figure 4.1: (a)Time evolution of boron density profile in the C-Mod discharge with 3.5 MW ICRF heating, from the H-mode (blue circles), transition (black squares), to ITB (red triangles); (b) boron density gradient profile in H-mode (blue dash) and ITB (red solid).[60]

we see that it is crucial to understand the conditions needed for impurities to accumulate in the core.

## 4.2 C-Mod Impurity Experiments

Recently, Rowan et al. [60] show that the light impurity boron peaks strongly in the core of the ICRF driven ITB plasmas, as had been shown earlier for argon in C-Mod, JET and JT-60U. Figure 4.1 shows the time evolution of the fully stripped boron density profile from the H-mode to the ITB. Figure 4.1(a) shows the change of the boron density profile from hollow at $t = 0$ (circles) through the transition with flat profile at $t = 0.12$ (squares), to the peaked profile in the ITB regime $t = 0.24$ to 0.36s (diamonds). The normalized density gradient scale length of boron $B^{5+}$ is shown in Fig. 4.1(b)

from negative in the H-mode to positive in the ITB regime.The peak of the ICRF power deposition is at $\rho = 0.5$, just outside the ITB region that starts at $\rho = 0.4$. One interpretation is that the ITG-TEM modes are transporting the boron with convection velocity (also called pinch velocity) $V = -D/L_n$. The change in the electron density profile from flat $R/L_{ne} \sim 0$ in the H-mode regime to peaked $R/L_{ne} \sim 5$ in the ITB regime weakens the ITG and enhances the density gradient driven TEM mode. This density profile change motivates us to investigate density-gradient-driven drift waves.

## 4.3 Quasilinear Theory

To analyze plasmas with impurities, we extend the multi-fluid models given in Futatani et al. [23]. A set of fluid equations is used to find the eigenmodes and eigenfrequencies of a nonuniform, magnetized plasma with a fluctuation vector $\mathbf{X}_k$ composed of fluctuations of the electron density $\delta n_e$, the main ion (working gas) density $\delta n_i$, the impurity density $\delta n_z$ and the electrostatic potential $\phi$. From the eigenmodes and eigenvectors we compute the out-of-phase part of the density-to-potential fluctuations and derive the quasilinear particle fluxes driven by the plasma gradients. The fluctuation power spectrum is taken from nonlinear simulations and their parameterization. This quasilinear method can be much faster than nonlinear gyrokinetic simulations and it enable us to develop a fast code for impurity transport estimation.

We then use data from Alcator C-Mod with boronized walls to obtain a wide range of realistic plasma gradients for the wide range of confinement

regimes. Multiple types of drift wave modes exist in such plasmas. In the nonlinear state the modes are coupled in a complex manner. For weakly turbulent states, we use the quasilinear theory to calculate particle fluxes for separate modes. The qualitative changes of the particle fluxes with variation of the sign and strength of the density gradients are compared with C-Mod plasmas in the H-mode, ITB, and I-mode regimes. We show that the impurity gradient driven drift wave is unstable for the impurity profile peaked toward the plasma edge and produces inward transport of impurities and an outward flux of main ions. Similar results are reported in [2, 36] from quasilinear models.

### 4.3.1 Density Gradient Driven Drift Waves

Now let us introduce the equations needed to model ordinary drift waves, i.e. density gradient driven drift waves, in three component plasmas. We assume the temperature profile is flat and temperature fluctuations are negligible.

First, the ion continuity equation reads

$$\frac{\partial \delta n_i}{\partial t} + \nabla_\perp \cdot n_i(\mathbf{v}_E + \mathbf{v}_{di} + \mathbf{v}_{pi} + \mathbf{v}_{\pi i}) + \frac{c^2 \eta_i}{eB^2}\nabla^4 \phi = 0, \tag{4.1}$$

where we use the low frequency assumption $\omega \ll \omega_{ci}$, so that $\mathbf{v}_E \gg \mathbf{v}_{pi}$. The viscosity originates from the off-diagonal terms of the stress tensor

$$-\nabla \cdot \boldsymbol{\pi} = \eta \nabla^2 \mathbf{v}. \tag{4.2}$$

The ion viscosity $\eta_i$ can be estimated as (e.g. p38 NRL 2007)

$$\eta_i = \frac{3n_i T_i}{10\omega_{ci}^2 \tau_i}. \tag{4.3}$$

Second, the impurity continuity equation is similar

$$\frac{\partial \delta n_z}{\partial t} + \nabla_\perp \cdot n_z(\mathbf{v}_E + \mathbf{v}_{dz} + \mathbf{v}_{pz} + \mathbf{v}_{\pi z}) + \frac{c^2 \eta_z}{ZeB^2}\nabla^4 \phi = 0, \tag{4.4}$$

where the impurity viscosity is

$$\eta_z = \frac{3n_z T_z}{10\omega_{cz}^2 \tau_z}. \tag{4.5}$$

Third, in the electron continuity equation

$$\frac{\partial \delta n_e}{\partial t} + \nabla \cdot n_e(\mathbf{v}_E + \mathbf{v}_{de}) + n_e \nabla_\parallel v_{\parallel e} = 0, \tag{4.6}$$

we neglect the electron polarization term. Lastly, the equation of electron parallel motion

$$0 = -T_e \nabla_\parallel n_e + n_e e \nabla_\parallel \phi - n_e m_e \nu_{ei} v_{\parallel e}, \tag{4.7}$$

where $\nu_{ei}$ is the electron-ion collision rate(p33 NRL 2007),

$$\nu_{ei} = \frac{\sqrt{2} n_i e^4 \ln \Lambda}{12\pi^{3/2}\epsilon_0^2 m_e^{1/2} T_e^{3/2}} \approx 2.9 \times 10^{-6} n_i (\ln \Lambda) T_e^{-3/2}. \tag{4.8}$$

This gives Ohm's law

$$j_\parallel = -e n_e v_{\parallel e} = \sigma_\parallel \left( -\nabla_\parallel \phi + \frac{T_e}{e n_e} \nabla_\parallel n_e \right), \tag{4.9}$$

where

$$\sigma_\parallel = \frac{e^2 n_e}{m_e \nu_{ei}}. \tag{4.10}$$

Here we neglect the acceleration term on the left hand side of Eq. (4.7) based on the low frequency assumption that $|\omega| \ll \nu_{ei}$. In the case of very low collisionality, dissipation due to electron Landau damping can be important. We model this kinetic effect by a fluid-like effective collision rate $\nu_{\text{eff}} \sim |k_\parallel| v_e$.

It is usually convenient to replace one of the continuity equations by the vortex equation when applying the quasineutrality condition

$$\nabla_\perp \cdot [n_i \mathbf{v}_{di} + Z n_z \mathbf{v}_{dz} - n_e \mathbf{v}_{de}] + \nabla_\perp \cdot [n_i(\mathbf{v}_{pi} + \mathbf{v}_{\pi i}) + Z n_z(\mathbf{v}_{pz} + \mathbf{v}_{\pi z})] + \frac{1}{e}\nabla_\parallel j_\parallel = 0. \quad (4.11)$$

### 4.3.2 Slab Geometry

In slab geometry, coordinates are setup so that the magnetic field is along $z$ direction $\mathbf{B} = B\hat{\mathbf{e}}_z$, $x$ is the direction of the minor radius, and $y$ is the poloidal direction. The background density only has a gradient in the $x$ direction. Therefore, the equations are simplified as

$$\nabla \cdot \mathbf{v}_E = 0 \quad (4.12)$$

$$\nabla \cdot (n_s \mathbf{v}_{ds}) = 0 \quad (4.13)$$

$$\nabla \cdot n_s(\mathbf{v}_{ps} + \mathbf{v}_{\pi s}) \approx -i n_s k_\perp^2 \rho_s^2 (\omega - \omega_{ds}) \frac{e\phi}{T_e}, \quad (4.14)$$

where the gyro-viscosity cancellation is used in the last equation.

Now consider small perturbations of the densities $\delta n_s = n_s - n_{s0}$ (subscript 0 denotes equilibrium quantities) and electric potential $\phi$ (zero equilibrium potential). Quasi-neutrality requires

$$\delta n_i + Z \delta n_z = \delta n_e. \quad (4.15)$$

Let

$$\tilde{n}_s = \frac{\delta n_s}{n_s}, \tilde{\phi} = \frac{e\phi}{T_e}, \tag{4.16}$$

then we have equations for the ordinary drift waves

$$\frac{d\tilde{n}_i}{dt} - v_{*i}\frac{T_i}{T_e}\frac{\partial}{\partial y}\tilde{\phi} - \frac{d}{dt}\rho_s^2\nabla^2\tilde{\phi} + \tilde{\mu}_i\rho_s^4\nabla_\perp^4\tilde{\phi} = 0 \tag{4.17}$$

$$\frac{d\tilde{n}_z}{dt} - v_{*z}\frac{ZT_z}{T_e}\frac{\partial}{\partial y}\tilde{\phi} - \frac{A}{Z}\frac{d}{dt}\rho_s^2\nabla^2\tilde{\phi} + \frac{A}{Z}\tilde{\mu}_z\rho_s^4\nabla_\perp^4\tilde{\phi} = 0 \tag{4.18}$$

$$\frac{d\tilde{n}_e}{dt} + v_{*e}\frac{\partial}{\partial y}\tilde{\phi} + \frac{T_e}{m_e\nu_{ei}}\nabla_\parallel(-\nabla_\parallel\tilde{n}_e + \nabla_\parallel\tilde{\phi}) = 0 \tag{4.19}$$

where

$$\frac{d}{dt} \equiv \frac{\partial}{\partial t} + \mathbf{v}_E \cdot \nabla. \tag{4.20}$$

Using the following normalization

$$\tilde{t} = t\omega_{ci}, \tilde{l} = l/\rho_s, \rho_s = c_s/\omega_{ci}, c_s = \sqrt{T_e/m_i}, \tag{4.21}$$

and defining the density scale length

$$L_{ns} = -\frac{n_{s0}}{\frac{dn_{s0}}{dx}}, \tag{4.22}$$

the equations become

$$\frac{\partial\tilde{n}_i}{\partial\tilde{t}} + \frac{\rho_s}{L_{n_i}}\frac{\partial}{\partial\tilde{y}}\tilde{\phi} + \left[\tilde{\phi}, \tilde{n}_i\right] - \left(\frac{\partial}{\partial\tilde{t}}\tilde{\nabla}_\perp^2\tilde{\phi} + \left[\tilde{\phi}, \tilde{\nabla}_\perp^2\tilde{\phi}\right]\right) + \tilde{\mu}_i\tilde{\nabla}_\perp^4\tilde{\phi} = 0 \tag{4.23}$$

$$\frac{\partial\tilde{n}_z}{\partial\tilde{t}} + \frac{\rho_s}{L_{n_z}}\frac{\partial}{\partial\tilde{y}}\tilde{\phi} + \left[\tilde{\phi}, \tilde{n}_z\right] - \frac{A}{Z}\left(\frac{\partial}{\partial\tilde{t}}\tilde{\nabla}_\perp^2\tilde{\phi} + \left[\tilde{\phi}, \tilde{\nabla}_\perp^2\tilde{\phi}\right]\right) + \frac{A}{Z}\tilde{\mu}_z\tilde{\nabla}_\perp^4\tilde{\phi} = 0 \tag{4.24}$$

$$\frac{\partial \tilde{n}_e}{\partial \tilde{t}} + \frac{\rho_s}{L_{n_e}} \frac{\partial}{\partial \tilde{y}} \tilde{\phi} + \left[ \tilde{\phi}, \tilde{n}_e \right] + \frac{m_i}{m_e} \frac{\omega_{ci}}{\nu_{ei}} \tilde{\nabla}_\parallel (-\tilde{\nabla}_\parallel \tilde{n}_e + \tilde{\nabla}_\parallel \tilde{\phi}) = 0, \tag{4.25}$$

where

$$\tilde{\mu}_i = \frac{\eta_i}{m_i n_i} \frac{1}{\rho_s c_s}, \;\; \tilde{\mu}_z = \frac{\eta_z}{m_z n_z} \frac{1}{\rho_s c_s}, \tag{4.26}$$

and the Poisson bracket is defined as

$$[f, g] = \frac{\partial f}{\partial \tilde{x}} \frac{\partial g}{\partial \tilde{y}} - \frac{\partial g}{\partial \tilde{x}} \frac{\partial f}{\partial \tilde{y}}. \tag{4.27}$$

Equation (4.25) can be replaced by Eq. (4.11)

$$\left( \frac{n_i}{n_e} + A \frac{n_z}{n_e} \right) \left( -\frac{\partial}{\partial \tilde{t}} \tilde{\nabla}_\perp^2 \tilde{\phi} - \left[ \tilde{\phi}, \tilde{\nabla}_\perp^2 \tilde{\phi} \right] \right) + (\tilde{\mu}_i \frac{n_i}{n_e} + \tilde{\mu}_z A \frac{n_z}{n_e}) \tilde{\nabla}_\perp^4 \tilde{\phi}$$
$$- \frac{m_i}{m_e} \frac{\omega_{ci}}{\nu_{ei}} (\tilde{\nabla}_\parallel^2 \tilde{\phi} - \frac{n_i}{n_e} \tilde{\nabla}_\parallel^2 \tilde{n}_i - Z \frac{n_z}{n_e} \tilde{\nabla}_\parallel^2 \tilde{n}_z) = 0. \tag{4.28}$$

Equations (4.23) (4.24) (4.28) describe the ordinary drift waves in a three-component plasma.

#### 4.3.2.1 Linear Analysis

For a linear analysis, we assume the time dependence $e^{-i\omega t}$, drop nonlinear terms (Poisson brackets), and rewrite the linearized equations for ordinary drift waves in slab geometry in the following matrix form:

$$\begin{bmatrix} 0 & \frac{n_i}{n_e} & Z\frac{n_z}{n_e} & -1 \\ -i\omega_{*i} - i\omega k_\perp^2 \rho_s^2 + \mu_i k_\perp^4 \rho_s^2 & -i\omega & 0 & 0 \\ -iZ\omega_{*z} - i\omega \frac{A}{Z} k_\perp^2 \rho_s^2 + \mu_z \frac{A}{Z} k_\perp^4 \rho_s^2 & 0 & -i\omega & 0 \\ i\omega_{*e} - \nu_\parallel & 0 & 0 & -i\omega + \nu_\parallel \end{bmatrix}$$
$$\begin{bmatrix} \frac{e\Phi}{T_e} \\ \frac{\delta n_i}{n_i} \\ \frac{\delta n_z}{n_z} \\ \frac{\delta n_e}{n_e} \end{bmatrix} = \begin{bmatrix} 0 \\ 0 \\ 0 \\ 0 \end{bmatrix} \tag{4.29}$$

The drift frequencies are defined by

$$\omega_{*i} \equiv k_y \frac{cT_e}{eB}\frac{1}{n_i}\frac{\partial n_{i0}}{\partial x} = -k_y\rho_s\frac{c_s}{L_{n_i}} = k_y\frac{T_e}{T_i}v_{*i} \tag{4.30}$$

$$\omega_{*z} \equiv k_y \frac{cT_e}{ZeB}\frac{1}{n_z}\frac{\partial n_{z0}}{\partial x} = -k_y\rho_s\frac{c_s}{ZL_{n_z}} = k_y\frac{T_e}{T_z}Zv_{*z} \tag{4.31}$$

$$\omega_{*e} \equiv -k_y \frac{cT_e}{eB}\frac{1}{n_e}\frac{\partial n_{e0}}{\partial x} = k_y\rho_s\frac{c_s}{L_{n_e}} = k_y v_{*e} \tag{4.32}$$

$$\nu_\parallel = \frac{T_e k_\parallel^2}{m_e\nu_{ei}}, \tag{4.33}$$

and therefore

$$\frac{1}{L_{ne}} = \frac{n_i}{n_e}\frac{1}{L_{ni}} + Z\frac{n_z}{n_e}\frac{1}{L_{nz}} \tag{4.34}$$

or

$$\omega_{*e} + \frac{n_i}{n_e}\omega_{*i} + Z^2\frac{n_z}{n_e}\omega_{*z} = 0. \tag{4.35}$$

Here we let ion and electron drift frequencies have opposite signs to emphasize the different diamagnetic-drift directions for different species.

By using the quasi-neutrality condition, we can eliminate $\frac{\delta n_e}{n_e}$ and get

$$\begin{bmatrix} -i\omega & 0 & a_{13} \\ 0 & -i\omega & a_{23} \\ 0 & 0 & a_{33} \end{bmatrix} \begin{bmatrix} \frac{\delta n_i}{n_i} \\ \frac{\delta n_z}{n_z} \\ \frac{e\phi}{T_e} \end{bmatrix} = \begin{bmatrix} 0 \\ 0 \\ 0 \end{bmatrix} \tag{4.36}$$

where

$$a_{13} = -i\omega_{*i} + \mu_i k_\perp^4\rho_s^2 - i\omega k_\perp^2\rho_s^2 \tag{4.37}$$

$$a_{23} = -iZ\omega_{*z} + \frac{A}{Z}\mu_z k_\perp^4\rho_s^2 - i\omega\frac{A}{Z}k_\perp^2\rho_s^2 \tag{4.38}$$

$$a_{33} = \frac{\nu_\parallel - i\omega}{i\omega}(k_\perp^4\rho_s^2\mu_\tau - i\omega k_\perp^2\rho_s^2 n_\tau + i\omega_{*e}) + (i\omega_{*e} - \nu_\parallel) \tag{4.39}$$

$$n_\tau = \frac{n_i}{n_e} + A\frac{n_z}{n_e} \tag{4.40}$$

$$\mu_\tau = \frac{n_i}{n_e}\mu_i + A\frac{n_z}{n_e}\mu_z. \tag{4.41}$$

The dispersion relation, obtained by setting the determinant (which is the product of diagonal terms for upper triangle matrices) to be zero, is

$$\omega(A\omega^2 + B\omega + C) = 0 \tag{4.42}$$

where

$$A = k_\perp^2 \rho_s^2 n_\tau \tag{4.43}$$

$$B = i[k_\perp^4 \rho_s^2 \mu_\tau + \nu_\parallel (1 + k_\perp^2 \rho_s^2 n_\tau)] \tag{4.44}$$

$$C = -(k_\perp^4 \rho_s^2 \mu_\tau + i\omega_{*e})\nu_\parallel. \tag{4.45}$$

For the $\omega = 0$ mode, there is no potential fluctuation and $\phi = 0$, which implies

$$\delta n_i + Z\delta n_z = 0. \tag{4.46}$$

There are two non-zero roots. We can estimate the growth rate and frequency in the limit of zero viscosities by substituting $\omega = \omega_r + i\gamma$ into Eq. (4.42). First we assume $|\gamma| \ll \omega_r, \nu_\parallel$, balance the real and imaginary parts and get

$$\omega_r = \frac{\omega_{*e}}{1 + k_\perp^2 \rho_s^2 n_\tau}, \tag{4.47}$$

$$\gamma = \frac{\omega_{*e}^2 k_\perp^2 \rho_s^2 n_\tau}{(1 + k_\perp^2 \rho_s^2 n_\tau)^3 \nu_\parallel}, \tag{4.48}$$

and the polarization

$$\frac{\delta n_i}{n_i} \Big/ \frac{e\phi}{T_e} = -\left[1 - i\frac{k_\perp^2 \rho_s^2 n_\tau}{(1 + k_\perp^2 \rho_s^2 n_\tau)^2} \frac{\omega_{*e}}{\nu_\parallel}\right] (1 + k_\perp^2 \rho_s^2 n_\tau) \frac{\omega_{*i}}{\omega_{*e}} - k_\perp^2 \rho_s^2. \tag{4.49}$$

Note that this is the unstable mode driven by the electron density gradient. Secondly for $|\gamma| \gg \omega$, we can get a strongly damped mode with

$$\omega_r = -\frac{\omega_{*e}}{1 + k_\perp^2 \rho_s^2 n_\tau}, \tag{4.50}$$

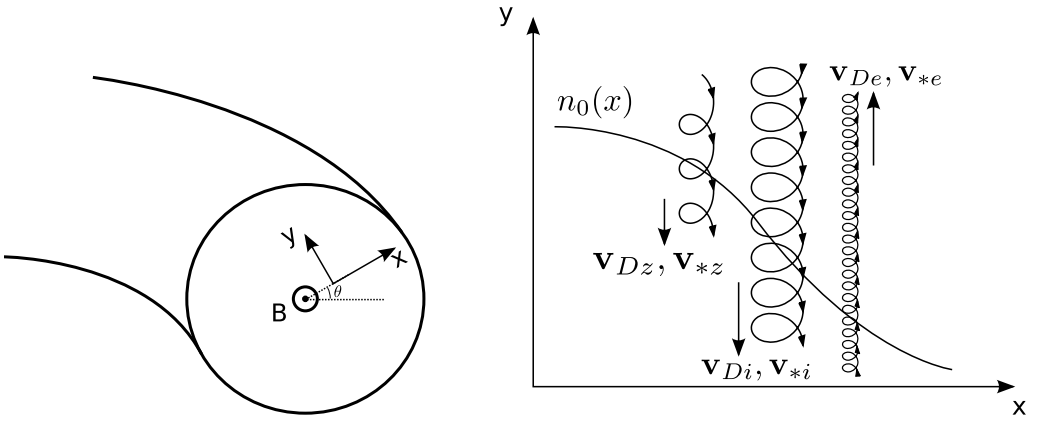


$$\gamma = -\nu_{\parallel} \frac{1 + k_{\perp}^2 \rho_s^2 n_{\tau}}{k_{\perp}^2 \rho_s^2 n_{\tau}}. \tag{4.51}$$

Equation (4.36) can also be written as

$$(-i\omega)\mathbf{A}\mathbf{\Phi} = \mathbf{C}\mathbf{\Phi} \tag{4.52}$$

where

$$\mathbf{A} = \begin{bmatrix} k_{\perp}^2 \rho_s^2 n_{\tau} & 0 & 0 \\ k_{\perp}^2 \rho_s^2 & 1 & 0 \\ \frac{A}{Z} k_{\perp}^2 \rho_s^2 & 0 & 1 \end{bmatrix}, \Phi = \begin{bmatrix} \frac{e\phi}{T_e} \\ \frac{\delta n_i}{n_i} \\ \frac{\delta n_z}{n_z} \end{bmatrix} \tag{4.53}$$

and

$$\mathbf{C} = \begin{bmatrix} -\nu_{\parallel} - k_{\perp}^4 \rho_s^2 \mu_{\tau} & \nu_{\parallel} \frac{n_i}{n_e} & \nu_{\parallel} Z \frac{n_z}{n_e} \\ i\omega_{*i} - \mu_i k_{\perp}^4 \rho_s^2 & 0 & 0 \\ iZ\omega_{*z} - \mu_z \frac{A}{Z} k_{\perp}^4 \rho_s^2 & 0 & 0 \end{bmatrix}. \tag{4.54}$$

### 4.3.3 Toroidal Effects

In tokamaks, the toroidal fields are generated by external coils, so

$$\mathbf{B}_t = B_0 \hat{\mathbf{z}} \frac{R_0}{R} = \frac{B_0 \hat{\mathbf{z}}}{1 + \frac{r}{R_0} \cos\theta} \tag{4.55}$$

and $\nabla \times \mathbf{B}_t = 0$, where $B_0$ and $R_0$ are the magnetic field and the major radius at the center, respectively. In this geometry, assuming $\mathbf{B} \approx \mathbf{B}_t$, we have

$$\begin{aligned}
\nabla \cdot \mathbf{v}_E &= (\nabla \frac{1}{B^2}) \cdot (c\mathbf{B} \times \nabla\phi) + \frac{c}{B^2} \nabla \cdot (\mathbf{B} \times \nabla\phi) && (4.56)\\
&= \frac{2\hat{\mathbf{x}}}{B^2 R} \cdot c\mathbf{B} \times \nabla\phi + 0 && (4.57)\\
&= \frac{q_s}{T_s} \mathbf{v}_{Ds} \cdot \nabla\phi, && (4.58)
\end{aligned}$$

where

$$\mathbf{v}_{Ds} = \frac{2cT_s}{q_s BR} \hat{\mathbf{x}} \times \hat{\mathbf{b}} \tag{4.59}$$

and if $\nabla n$ is in $\hat{\mathbf{x}}$ direction, then $\mathbf{v}_{Ds} = 2\epsilon_n \mathbf{v}_{*s}$, where $\epsilon_n = L_n/R$. Also,

$$\begin{aligned}
\nabla \cdot \mathbf{v}_{ds} &= \frac{c}{q_s} \nabla \cdot \frac{\mathbf{B} \times \nabla p_s}{n_s B^2} && (4.60)\\
&= \frac{c}{q_s} \left[ \nabla \frac{1}{B^2} \cdot \frac{\mathbf{B} \times \nabla p_s}{n_s} + \frac{1}{B^2} \nabla \cdot (\frac{\mathbf{B} \times \nabla p_s}{n_s}) \right] && (4.61)\\
&= \frac{c}{q_s} \left[ \frac{2\hat{\mathbf{x}} \times \hat{\mathbf{b}}}{BRn_s} \cdot \nabla p_s - \frac{1}{B^2} \frac{\nabla n_s}{n_s^2} \cdot \mathbf{B} \times \nabla p_s \right] && (4.62)\\
&= \mathbf{v}_{Ds} \cdot \frac{\nabla p_s}{p_s} - \mathbf{v}_{ds} \cdot \frac{\nabla n_s}{n_s} && (4.63)\\
&= \mathbf{v}_{Ds} \cdot \frac{\nabla p_s}{p_s} + \mathbf{v}_{ds} \cdot \frac{\nabla T_s}{T_s} && (4.64)
\end{aligned}$$

where in the last step we make use of $\nabla n_s \times \nabla p_s = \nabla n_s \times n_s \nabla T_s = \nabla p_s \times n_s \nabla T_s / T_s$. The second to last line shows the cancellation of the diamagnetic convection so that $\nabla \cdot n_s \mathbf{v}_{ds} = \mathbf{v}_{Ds} \cdot \nabla p_s / p_s$. The gyro-viscosity cancellation is used to eliminate the diamagnetic contribution in $\nabla \cdot \mathbf{v}_{p_s}$,

$$\nabla \cdot n_s (\mathbf{v}_{ps} + \mathbf{v}_{\pi s}) \approx -i n_s k_\perp^2 \rho_s^2 (\omega - \omega_{ds}) \frac{e\phi}{T_e}. \tag{4.65}$$

Therefore, assuming constant temperatures, the continuity equations are

$$\frac{d\tilde{n}_i}{dt} - (v_{*i}\frac{T_e}{T_i} + v_{De})\frac{\partial}{\partial y}\tilde{\phi} - \frac{T_i}{T_e}v_{De}\frac{\partial}{\partial y}\tilde{n}_i - \frac{d}{dt}\rho_s^2\nabla^2\tilde{\phi} + \mu_i\rho_s^2\nabla_\perp^4\tilde{\phi} = 0 \quad (4.66)$$

$$\frac{d\tilde{n}_z}{dt} - (v_{*z}\frac{ZT_e}{T_z} + v_{De})\frac{\partial}{\partial y}\tilde{\phi} - \frac{T_z}{ZT_e}v_{De}\frac{\partial}{\partial y}\tilde{n}_z - \frac{A}{Z}\frac{d}{dt}\rho_s^2\nabla^2\tilde{\phi} + \frac{A}{Z}\mu_z\rho_s^2\nabla_\perp^4\tilde{\phi} = 0 \quad (4.67)$$

$$\frac{d\tilde{n}_e}{dt} + (v_{*e} - v_{De})\frac{\partial}{\partial y}\tilde{\phi} + v_{De}\frac{\partial}{\partial y}\tilde{n}_e + \frac{T_e}{m_e\nu_{ei}}\nabla_\parallel(-\nabla_\parallel\tilde{n}_e + \nabla_\parallel\tilde{\phi}) = 0 \quad (4.68)$$

And the last equation can be replaced by the vortex equation

$$-(\frac{n_i}{n_e} + A\frac{n_z}{n_e})\frac{d}{dt}\rho_s^2\nabla^2\phi - v_{De}[\frac{n_i}{n_e}(\frac{T_i}{T_e} + 1)\frac{\partial}{\partial y}\tilde{n}_i + \frac{n_z}{n_e}(\frac{T_z}{T_e} + Z)\frac{\partial}{\partial y}\tilde{n}_z] \quad (4.69)$$
$$+(\frac{n_i}{n_e}\mu_i + A\frac{n_z}{n_e}\mu_z)\rho_s^2\nabla_\perp^4\phi + \frac{T_e}{m_e\nu_{ei}}\nabla_\parallel^2(\frac{n_i}{n_e}\tilde{n}_i + Z\frac{n_z}{n_e}\tilde{n}_z - \tilde{\phi}) = 0.$$

In matrix form, these equations are

$$(-i\omega)\mathbf{A}\mathbf{\Phi} = \mathbf{C}\mathbf{\Phi} \quad (4.70)$$

where

$$\mathbf{A} = \begin{bmatrix} k_\perp^2\rho_s^2 n_\tau & 0 & 0 \\ k_\perp^2\rho_s^2 & 1 & 0 \\ \frac{A}{Z}k_\perp^2\rho_s^2 & 0 & 1 \end{bmatrix}, \Phi = \begin{bmatrix} \frac{e\phi}{T_e} \\ \frac{\delta n_i}{n_i} \\ \frac{\delta n_z}{n_z} \end{bmatrix} \quad (4.71)$$

and

$$\mathbf{C} = \begin{bmatrix} -\nu_\parallel - k_\perp^4\rho_s^2\mu_\tau & \frac{n_i}{n_e}(\nu_\parallel + i\omega_{De}\tau_i') & \frac{n_z}{n_e}(\nu_\parallel Z + i\omega_{De}\tau_z') \\ i\omega_{*i} + i\omega_{De} - \mu_i k_\perp^4\rho_s^2 & i\omega_{De}\tau_i & 0 \\ iZ\omega_{*z} + i\omega_{De} - \mu_z\frac{A}{Z}k_\perp^4\rho_s^2 & 0 & i\omega_{De}\frac{\tau_z}{Z} \end{bmatrix} \quad (4.72)$$

Here $\omega_{De} = k_y v_{De}$, $\tau_s = T_s/T_e$, $\tau_s' = T_s/T_e + Z_s$.

#### 4.3.3.1 Without Impurity

The dispersion relation is a cubic equations with three roots in general. If we first take the limit with no impurity, then a simplified dispersion relation is obtained by considering only the first two columns and the first two rows of both matrices $A$ and $C$:

$$k_\perp^2\rho_s^2\omega^2 + i\omega[\nu_\parallel(1+k_\perp^2\rho_s^2) + ik_\perp^2\rho_s^2\omega_{De}Z_i]$$
$$+i(\nu_\parallel + i\omega_{De}\tau_i')(\omega_{*i}+\omega_{De}) + i\nu_\parallel\omega_{De}\tau_i = 0. \quad (4.73)$$

Assuming $\gamma \ll \omega_r, \nu_\parallel$, and $\omega_{De} \ll \nu_\parallel$, the approximate solution is $\omega = \omega_r + i\gamma$ where

$$\omega_r = \frac{-\omega_{*i} - \omega_{De}(1+\tau_i)}{1+k_\perp^2\rho_s^2}, \quad (4.74)$$

$$\gamma = \frac{\omega_r(\omega_r - \omega_{De})k_\perp^2\rho_s^2 - (\omega_{*i}+\omega_{De})\omega_{De}\tau_i'}{\nu_\parallel(1+k_\perp^2\rho_s^2)}. \quad (4.75)$$

Sometimes we may further restrict $\omega_{De} \ll \omega_{*i}$, in which case the mode is destablized when $\omega_{De}\omega_{*i} < 0$ (bad curvature) and stablized when $\omega_{De}\omega_{*i} > 0$ (good curvature). But in real tokamaks, often $\omega_{De}$ is comparable to $\omega_{*i}$. In C-Mod H mode discharges, $\omega_{De}$ is even larger than $\omega_{*i}$ for flat density profiles, and the above dispersion relation will give damping for small $k_\perp\rho_s$ regardless of the sign of $\omega_{De}$.

For another limit with $|\gamma| \gg |\omega_r|, \omega_{De}, \omega_{*i}$, we find the frequency and growth rate of a strongly damped mode with

$$\omega_r = \frac{(1+k_\perp^2\rho_s^2)\omega_{De}Z_i + \omega_{*i} + \omega_{De}(1+\tau_i)}{1+k_\perp^2\rho_s^2}, \quad (4.76)$$

$$\gamma = -\frac{\nu_\parallel(1+k_\perp^2\rho_s^2)}{k_\perp^2\rho_s^2}. \quad (4.77)$$

#### 4.3.3.2 With Impurity

When a significant amount of impurity is present, a third "impurity mode" emerges. The frequency and growth rate of this mode can be estimated as

$$\omega_r \approx -\omega_{De}\frac{\tau_z}{Z} = k_y v_{Dz}, \tag{4.78}$$

$$\gamma \approx -\frac{n_z}{n_e}\omega_{De}\tau_z k_\perp^2\rho_s^2[\omega_{De}(1-\frac{A\tau_z}{Z^2}k_\perp^2\rho_s^2)+Z\omega_{*z}]. \tag{4.79}$$

The properties of the impurity mode change with the curvature effect. In the limit of a slab geometry($1/R \to 0$), the frequency of this mode is zero for all $k_y$, and the eigenvector shows $Z\delta n_z+\delta n_i = 0$ and $\phi = 0$, therefore no transport results. The curvature effect breaks this symmetry between the main ions and the impurity ions, and give rises to significant particle transport.

Before showing numerical results, we list the reference parameters for ITER and Alcator C-Mod in Table 4.1. For the rest of this chapter, numerical results are based on C-Mod parameters unless otherwise specified.

The dispersion relation of these modes for a set of typical C-Mod parameters with peaked impurity profile are shown in Fig. 4.2. Although the growth rate of the impurity mode is relatively small compared to the ITG mode (Fig. 4.4), it can still be important in nonlinear wave interactions and contribute to the impurity flux as we will see later.

The dimensionless eigenvectors $\mathbf{X}(\mathbf{k}) = \mathbf{\Phi}T_e/e\phi$ (we call them "polarization vectors") corresponding to these three modes, determine the particle

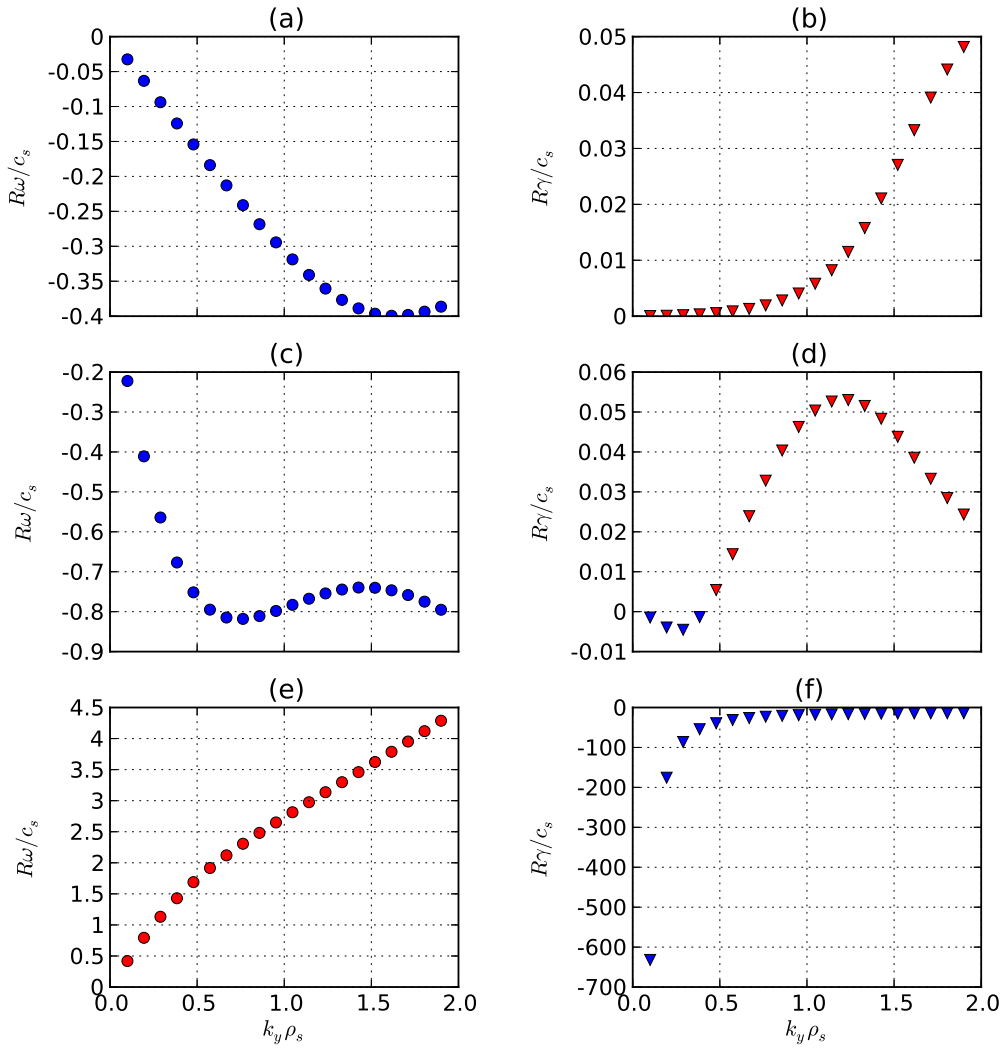


Figure 4.2: The frequencies and growth rates versus $k_y\rho$ for the three modes for the density-gradient-driven drift wave, based on typical C-Mod parameters in plasmas with peaked impurity profiles. (a)-(b) The frequency and growth rate of the impurity mode. (c)-(d) The frequency and growth rate of the electron drift wave mode. (e)-(f) The frequency and growth rate of the damped mode.

| | | ITER | C-Mod |
|---|---|---|---|
| $B$ | G | 50000 | 50000 |
| $T_i \approx T_e$ | eV | 1000 | 3000 |
| $R$ | cm | 600 | 76 |
| $a$ | cm | 200 | 22 |
| $Z$ | | 4 (beryllium) | 5 (boron) |
| $A$ | | 9 (beryllium) | 10 (boron) |
| $n_e$ | $\mathrm{cm}^{-3}$ | $10^{14}$ | $10^{14}$ |
| $n_z$ | $\mathrm{cm}^{-3}$ | $10^{12}$ | $5 \times 10^{11}$ |
| $Z_{\mathrm{eff}}$ | | 1.12 | 1.1 |

Table 4.1: Reference parameters of ITER and C-Mod.

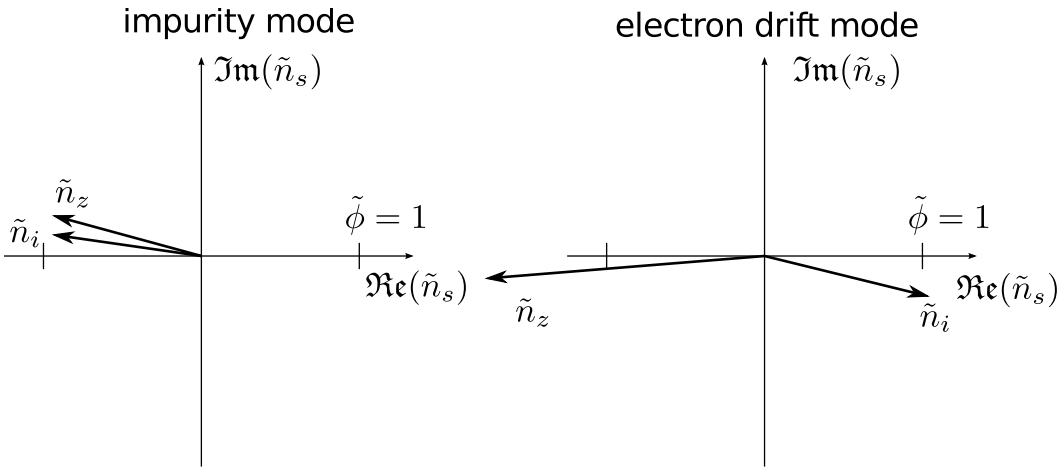


Figure 4.3: Polarization diagram of two eigenmodes of the drift wave model.

fluxes. As we will see later, the quasilinear flux is proportional to the phase difference between $\delta n_s$ and $\phi$ or $\mathfrak{Im}\,\mathbf{X}(\mathbf{k})$. We show these $\mathbf{X}(\mathbf{k})$ in Fig. 4.3 on the complex plane for a typical case with $L_{nz} > 0$. The phase angle of the vector with respect to the potential fluctuation is the polar angle of the vector with respect to the positive x-axis in the figure and the length of the vector gives the magnitude of the response with respect to the normalized potential fluctuation $e\phi/T_e$. For the case given in Fig. 4.3, the impurity mode gives rise to positive particle fluxes while the electron drift wave mode gives negative fluxes.

## 4.4 Impurity Drift Waves

### 4.4.1 Ion Parallel Motion

In the above analysis, we assumed that the parallel motion of ions and impurities are negligible. For low frequency modes, we may include the parallel ion motion described by

$$0 = -T_i \nabla_\parallel \delta n_i - n_i e \nabla_\parallel \phi - n_i m_i \nu_i v_{i\parallel}, \tag{4.80}$$

where $\nu_i \approx |k_\parallel| v_{ti}$ is the effective ion collision rate due to the ion Landau damping. Upon substituting parallel ion velocity $v_{i\parallel}$ into the continuity equation, we get a new term

$$\nabla_\parallel v_{i\parallel} = -\frac{c_s^2}{\nu_i} \nabla_\parallel^2 \left( \frac{e\phi}{T_e} + \frac{T_i}{T_e} \frac{\delta n_i}{n_i} \right) = \nu_{\parallel i} \frac{e\phi}{T_e} + \nu_{\parallel i} \frac{T_i}{T_e} \frac{\delta n_i}{n_i}. \tag{4.81}$$

Similarly, for impurities

$$\nabla_\parallel v_{z\parallel} \;=\; \nu_{\parallel z} Z \frac{e\phi}{T_e} + \nu_{\parallel z} \frac{T_z}{T_e} \frac{\delta n_z}{n_z} \tag{4.82}$$

where $\nu_z \approx \nu_{zi}$ is due to collisions with main ions.

### 4.4.2 Impurity Drift Waves

In the case of $\nu_\parallel \to \infty$, the electron response is adiabatic, i.e.

$$\frac{\delta n_e}{n_e} = \frac{e\Phi}{T_e}. \tag{4.83}$$

In this case we have impurity drift wave (IDW) equations

$$\begin{bmatrix} -1 & \frac{n_i}{n_e} & Z\frac{n_z}{n_e} \\ -i\omega_{*i} - i\omega_{De} - i\omega k_\perp^2\rho_s^2 + \mu_i k_\perp^4\rho_s^2 + \nu_{\|i} & -i\omega - i\omega_{De} + \frac{T_i}{T_e}\nu_{\|i} & 0 \\ -iZ\omega_{*z} - i\omega_{De} - i\omega\frac{A_1}{Z}k_\perp^2\rho_s^2 + \mu_z\frac{A_1}{Z}k_\perp^4\rho_s^2 + Z\nu_{\|z} & 0 & -i\omega - i\omega_{De} + \frac{T_z}{T_e}\nu_{\|z} \end{bmatrix} \begin{bmatrix} \frac{e\Phi}{T_e} \\ \frac{\delta n_i}{n_i} \\ \frac{\delta n_z}{n_z} \end{bmatrix} = \begin{bmatrix} 0 \\ 0 \\ 0 \end{bmatrix} \quad (4.84)$$

which are reduced to

$$\begin{bmatrix} \frac{n_i}{n_e}(-i\omega_{*i} - i\omega_{De} - i\omega k_\perp^2\rho_s^2 + \mu_i k_\perp^4\rho_s^2 + \nu_{\|i}) - i\omega - i\omega_{De} + \frac{T_i}{T_e}\nu_{\|i} & -Z\frac{n_z}{n_e}(-i\omega - i\omega_{De} + \frac{T_i}{T_e}\nu_{\|i}) \\ -iZ\omega_{*z} - i\omega_{De} - i\omega\frac{A_1}{Z}k_\perp^2\rho_s^2 + \mu_z\frac{A_1}{Z}k_\perp^4\rho_s^2 + Z\nu_{\|z} & -i\omega - i\omega_{De} + \frac{T_z}{T_e}\nu_{\|z} \end{bmatrix} \begin{bmatrix} \frac{e\Phi}{T_e} \\ \frac{\delta n_z}{n_z} \end{bmatrix} = \begin{bmatrix} 0 \\ 0 \end{bmatrix} \quad (4.85)$$

by substituting

$$\frac{\delta n_i}{n_i} = (\frac{e\phi}{T_e} - Z\frac{n_z}{n_e}\frac{\delta n_z}{n_z})\frac{n_e}{n_i}. \quad (4.86)$$

The system can be written as

$$(-i\omega)\bar{\mathbf{A}}\mathbf{\Phi} = \bar{\mathbf{C}}\mathbf{\Phi}, \tag{4.87}$$

where

$$\bar{\mathbf{A}} = \begin{bmatrix} 1 + k_\perp^2 \rho_s^2 \frac{n_i}{n_e} & -Z\frac{n_z}{n_e} \\ \frac{A_1}{Z} k_\perp^2 \rho_s^2 & 1 \end{bmatrix}, \Phi = \begin{bmatrix} \frac{e\phi}{T_e} \\ \frac{\delta n_z}{n_z} \end{bmatrix} \tag{4.88}$$

and

$$\bar{\mathbf{C}} = \begin{bmatrix} i\omega_{*i}\frac{n_i}{n_e} + i\omega_{De}(\frac{n_i}{n_e}+1) - \nu_{\parallel i}(\frac{n_i}{n_e}+\tau_i) - \mu_i \frac{n_i}{n_e} k_\perp^4 \rho_s^2 & Z\frac{n_z}{n_e}(\tau_i \nu_{\parallel i} - i\omega_{De}) \\ iZ\omega_{*z} + i\omega_{De} - \mu_z \frac{A_1}{Z} k_\perp^4 \rho_s^2 - Z\nu_{\parallel z} & -\nu_{\parallel z}\frac{T_z}{T_e} + i\omega_{De} \end{bmatrix} \tag{4.89}$$



The ion response has two limits

$$\frac{\delta n_i}{n_i} = \left( \frac{i\omega_{*i} + i\omega_{De} + i\omega k_\perp^2 \rho_s^2 - \nu_{\parallel i}}{-i\omega - i\omega_{De} + \nu_{\parallel i} T_i/T_e} \right) \frac{e\phi}{T_e} \tag{4.90}$$

$$= \begin{cases} -\dfrac{e\phi}{T_i} & \text{adiabatic when } \nu_{\parallel i} \to \infty \\ -\dfrac{\omega_{*i}}{\omega}\dfrac{e\phi}{T_e} & \text{hydrodynamic when } \nu_{\parallel i} \to 0 \end{cases} \tag{4.91}$$

## 4.5 Passive Impurity Transport

Usually the concentration of impurity is very small, so in the limit of $n_z \ll n_e$ our model should go back to the passive limit, where the impurity is not involved in the dynamics, but evolves passively due to the potential fluctuations.

The density, parallel velocity and temperature equations for the impurity are

$$(-i\omega + i\omega_{Dz})\bar{n}_z - (i\omega_{*z} + i\omega_{De} + i\omega\frac{A}{Z}k_\perp^2\rho_s^2)\bar{\phi} + i\omega_{Dz}\bar{T}_z + ik_\parallel c_s\bar{v}_\parallel = 0 \tag{4.92}$$

$$\frac{A}{Z}(-i\omega)\bar{v}_\parallel + (ik_\parallel c_s\bar{n} + ik_\parallel c_s\bar{T}_z)\frac{\tau_z}{Z} + ik_\parallel c_s\bar{\phi} = 0 \tag{4.93}$$

$$\left[\frac{3}{2}(-i\omega) - \frac{7}{2}i\omega_{De}\frac{\tau_z}{Z}\right]\bar{T}_z - (\frac{3}{2}i\omega_{*T} + i\omega_{De})\bar{\phi} - i\omega_{De}\frac{\tau_z}{Z}\bar{n}_z + ik_\parallel c_s\bar{v}_\parallel = 0, \tag{4.94}$$

which can be written as a system of linear inhomogeneous equations

$$\mathbf{A}\mathbf{x} = \mathbf{b} \tag{4.95}$$

where

$$\mathbf{x} = \begin{pmatrix} \bar{n}_z \\ \bar{T}_z \\ \bar{v}_\parallel \end{pmatrix}/\bar{\phi},\ \mathbf{b} = \begin{pmatrix} Z\omega_{*z} + \omega_{De} + \omega\frac{A}{Z}k_\perp^2\rho_s^2 \\ \frac{3}{2}\omega_{*T} + \omega_{De} \\ -k_\parallel c_s \end{pmatrix}, \tag{4.96}$$

$$\mathbf{A} = \begin{pmatrix} -\omega - \frac{\tau_z}{Z}\omega_{De} & -\omega_{De}\frac{\tau_z}{Z} & k_\parallel c_s \\ -\omega_{De}\frac{\tau_z}{Z} & -\frac{3}{2} - \frac{7}{2}\omega_{De}\frac{\tau_z}{Z} & k_\parallel c_s \\ k_\parallel c_s\frac{\tau_z}{Z} & k_\parallel c_s\frac{\tau_z}{Z} & -\omega\frac{A}{Z}. \end{pmatrix} \tag{4.97}$$

In the case of passive impurity, $\omega$ can be given by linear instability analysis for two-component plasmas. Then, we can solve the equations above for the vector $\mathbf{x}$, and calculate quasilinear fluxes for the impurity.

## 4.6 Neoclassical Impurity Transport

As mentioned in Chapter 1, the neoclassical theory predicts transport due to Coulomb collisions in plasmas in the toroidal geometry. Although the neoclassical theory usually underestimates the transport in present day tokamaks, the theory sets a good reference point for turbulent transport studies.

The neoclassical transport theory of plasmas with impurity is well documented in Wenzel and Sigmar [67] and exact formulas are quite complicated. Simplified analytic formulas for the impurity flux in the Pfirsch-Schlüter regime is given by Rutherford [61]

$$\Gamma_z^{PS} = \frac{q^2 n_i \rho_i^2 \nu_{iz}}{Z} \left[ C_n \left( \frac{\partial \ln n_i}{\partial r} - \frac{1}{Z} \frac{\partial \ln n_z}{\partial r} \right) - C_T \frac{\partial \ln T_i}{\partial r} \right], \tag{4.98}$$

where

$$\nu_{iz} = \frac{16\sqrt{\pi} e^4 \ln \Lambda}{3 m_i^2 v_{ti}^3} n_z Z^2 \tag{4.99}$$

$$C_n = 1 - \frac{0.52\alpha}{0.59 + \alpha + 1.34 g^{-2}} \tag{4.100}$$

$$C_T = 0.5 - \frac{0.29 + 0.68\alpha}{0.59 + \alpha + 1.34 g^{-2}}, \tag{4.101}$$

and $\alpha = n_z Z^2 / n_i$, $g = \epsilon^{3/2} \nu_*$ is the collisionality parameter of the working gas. Therefore,

$$D_z^{PS} = \frac{q^2 \rho_i^2 \nu_{zi}}{Z} \frac{m_z}{m_i} C_n \frac{1}{Z} \tag{4.102}$$

$$V_z^{PS} = \frac{q^2 \rho_i^2 \nu_{zi}}{Z} \frac{m_z}{m_i} \left( -\frac{C_n}{L_{ni}} + \frac{C_T}{L_{Ti}} \right), \tag{4.103}$$

where $\nu_{zi} = \nu_{iz} \frac{n_i}{n_z} \frac{m_i}{m_z}$.

## 4.7 Kinetic Theory of Fluctuations

We can also get a dispersion relation from kinetic theory

$$D_k(\omega) = k^2\lambda_{De}^2 + (1 - i\delta_k^e) + \frac{n_i T_e}{n_e T_i}\left[1 + \frac{\omega - \omega_{*i}}{|k_\parallel| v_i} Z\left(\frac{\omega}{|k_\parallel| v_i}\right)\Gamma_0(b_i)\right] + \frac{n_z Z^2 T_e}{n_e T_z}\left[1 + \frac{\omega - \omega_{*z}}{|k_\parallel| v_z} Z\left(\frac{\omega}{|k_\parallel| v_z}\right)\Gamma_0(b_z)\right] + \frac{n_{z2} Z_2^2 T_e}{n_e T_{z2}}\left[1 + \frac{\omega - \omega_{*z2}}{|k_\parallel| v_{z2}} Z\left(\frac{\omega}{|k_\parallel| v_{z2}}\right)\Gamma_0(b_{z2})\right] \quad (4.104)$$

where

$$\omega_{*s} = \frac{k_y c T_s}{e_s B}\frac{d\ln n_s}{dr} \quad (4.105)$$

$$v_s = \sqrt{\frac{2T_s}{m_s}} \quad (4.106)$$

$$b_s = k_\perp^2 \rho_s^2 \quad (4.107)$$

with $\rho_s^2 = m_s T_s / e^2 B^2$. Here we use the "$i\delta_k$" model of Terry-Horton to simplify the non-adiabatic electron response. For the collisional drift waves or the trapped electron instability, the full electron response $\chi_e(k,\omega)$ can be restored when required. Similarly, the ion response can be generalized to include the $\eta_s = d\ln T_s / d\ln n_s$ parameter when the ITG mode is strong.

## 4.8 Turbulent Particle Transport

### 4.8.1 Quasilinear Flux

Due to fluctuations, particle fluxes in the $x$ (radial) direction are

$$\begin{aligned}\Gamma_i &= < v_x \delta n_i >= \mathrm{Re}\left[\sum_k \frac{ik_y c\Phi_k^*}{B}\delta n_i\right] \\ &= -\sum_k k_y \rho_s c_s n_i \left|\frac{e\Phi}{T_e}\right|^2 \mathrm{Im}X_2 \qquad (4.108)\\ \Gamma_z &= < v_x \delta n_z >= \mathrm{Re}\left[\sum_k \frac{ik_y c\Phi_k^*}{B}\delta n_z\right] \\ &= -\sum_k k_y \rho_s c_s n_z \left|\frac{e\Phi}{T_e}\right|^2 \mathrm{Im}X_3 \qquad (4.109)\end{aligned}$$

where

$$\mathbf{X} = \begin{pmatrix} X_1 \\ X_2 \\ X_3 \end{pmatrix} = \begin{pmatrix} 1 \\ \frac{\delta n_i}{n_i}/\frac{e\Phi}{T} \\ \frac{\delta n_z}{n_z}/\frac{e\Phi}{T} \end{pmatrix}. \qquad (4.110)$$

### 4.8.2 Impurity Transport in the Slab Geometry

From the linear analysis above, we have

$$\frac{\delta n_z/n_z}{e\phi/T_e} = \frac{-iZ\omega_{*z} - i\omega\frac{A}{Z}k_\perp^2\rho_s^2}{i\omega}. \qquad (4.111)$$

The impurity particle flux in the $x$ direction is

$$\begin{aligned}\Gamma_z/n_z &= -c_s\sum_k k_y\rho_s \mathrm{Im}\left[\frac{\delta n_z/n_z}{e\phi/T_e}\right]\left|\frac{e\phi_k}{T_e}\right|^2 \qquad (4.112)\\ &= -c_s\sum_k k_y\rho_s \frac{Z\gamma\omega_{*z}}{\omega_r^2+\gamma^2}\left|\frac{e\phi_k}{T_e}\right|^2 \qquad (4.113)\\ &\approx -c_s\sum_k k_y\rho_s \frac{Zk_\perp^2\rho_s^2}{(1+k_\perp^2\rho_s^2)\nu_{\|e}}\omega_{*z}\left|\frac{e\phi_k}{T_e}\right|^2 \qquad (4.114)\end{aligned}$$

where we make use of Eq. (4.47) and Eq. (4.48) in the case of $\gamma \ll \omega_r$. Phenomenological models for particle flux are usually expressed as

$$\Gamma_z = -D_z \frac{\partial n_z}{\partial x} + V_z n_z \tag{4.115}$$

or

$$\Gamma_z / n_z = D_z / L_{nz} + V_z. \tag{4.116}$$

Therefore

$$D_z = c_s^2 \sum_k \frac{k_y^2 \rho_s^2 k_\perp^2 \rho_s^2}{(1 + k_\perp^2 \rho_s^2)\nu_{\|e}} \left| \frac{e\phi_k}{T_e} \right|^2 \tag{4.117}$$

$$V_z = 0, \tag{4.118}$$

from Eq. (4.114). Note there is no pinch velocity in slab geometry and the temperature gradient is not involved in the transport.

### 4.8.3 Impurity Transport in the Toroidal Geometry

In toroidal geometry, due to the effect of curvature, the pinch velocity is no longer zero. Linearizing Eq. (4.67) gives:

$$-i\omega\tilde{n}_z - i\omega_{*z}\tilde{\phi} - i\omega_{De}\tilde{\phi} + i\omega_{Dz}\tilde{p}_z - i\omega\frac{A}{Z}k_\perp^2\rho_s^2\tilde{\phi} - \frac{k_\|^2 v_z^2}{i\omega}\frac{T_e}{T_z}(\tilde{\phi} + \tilde{p}_z) = 0 \tag{4.119}$$

For the evolution of the impurity pressure, we can use $dp_z/dt \approx 0$ and get

$$\frac{\delta p_z}{p_z} = -\frac{\omega_{*z}}{\omega}(1 + \eta_z)\frac{e\phi}{T_e}. \tag{4.120}$$

Therefore

$$\frac{\delta n_z/n_z}{e\phi/T_e} = \frac{1}{\omega}\left[-\omega_{*z} - \omega_{De} - \frac{\omega_{Dz}\omega_{*z}}{\omega}(1+\eta_z)\right] + \frac{k_\parallel^2 v_z^2}{\omega^2}\frac{T_e}{T_z}[1 - \frac{\omega_{*z}}{\omega}(1+\eta_z)] - \frac{A}{Z}k_\perp^2\rho_s^2. \quad (4.121)$$

In the limit of no parallel motion, we find that the impurity particle flux is proportional to (assuming $\gamma \ll \omega_r$)

$$-\mathrm{Im}\left(\frac{\delta n_z/n_z}{e\phi/T_e}\right) = \frac{\gamma}{\omega_r^2}\left[\frac{cT_e}{eB}\frac{k_y}{L_{n_z}}(1+\frac{2}{\omega_r}k_y v_{Dz}) + \frac{cT_e}{eB}\frac{k_y}{L_{T_z}}\frac{2}{\omega_r}k_y v_{Dz} - k_y v_{De}\right] \quad (4.122)$$

and the transport coefficients are

$$D_z = c_s^2\sum_k (k_y\rho_s)^2\frac{\gamma}{\omega_r^2}(1+\frac{2}{\omega_r}k_y v_{Dz})\left|\frac{e\phi_k}{T_e}\right|^2, \quad (4.123)$$

$$V_z = c_s\sum_k (k_y\rho_s)\frac{\gamma}{\omega_r^2}\left[\frac{cT_e}{eB}\frac{k_y}{L_{T_z}}\frac{2}{\omega_r}k_y v_{Dz} - k_y v_{De}\right]\left|\frac{e\phi_k}{T_e}\right|^2. \quad (4.124)$$

The curvature pinch term and the thermal pinch term (related to $1/L_{Tz}$) compete to determine the direction of pinch when $\omega_r < 0$. For large $\omega_{De}$, the pinch changes from inward to outward if

$$\frac{R}{Z}\frac{T_i}{T_i+T_e} > L_{Ti}. \quad (4.125)$$

### 4.8.4 Fluctuation Spectrum

Now we need a model for the fluctuation level $\frac{e\Phi_k}{T_e}$, an example of which is

$$\left|\frac{e\Phi_k}{T_e}\right| = \frac{\Phi_0}{(1+k_\perp^2\rho_s^2)^{m/2}}. \quad (4.126)$$

We call this the 1-parameter spectral model with the parameter $m = 3-5$. The constant $\Phi_0$ can be determined by experiments or simulations if we integrate over all $\mathbf{k}$:

$$\int \left|\frac{e\Phi_k}{T_e}\right|^2 d\mathbf{k} = \int_0^\infty \int_0^\infty \left(\frac{\Phi_0}{(1+k_\perp^2\rho_s^2)^{3/2}}\right)^2 dk_x dk_y \tag{4.127}$$

$$= \frac{\pi}{2}\int_0^\infty \left(\frac{\Phi_0}{(1+k_\perp^2\rho_s^2)^{3/2}}\right)^2 k_\perp dk_\perp = \frac{\pi\Phi_0^2}{8} \tag{4.128}$$

$$\approx \sum_{m=1}^{N}\sum_{n=1}^{N}\left(\frac{\Phi_0}{(1+k_\perp^2\rho_s^2)^{3/2}}\right)^2 \Delta k_x \Delta k_y \tag{4.129}$$

where $k_\perp = \sqrt{k_x^2+k_y^2}$, $k_x = m\Delta k_x$, $k_y = n\Delta k_y$, $\Delta k_x = \Delta k_y = k_{\max}/N$. For $k_{\max}\rho_s = 5$ and $N = 400$, the above summation yields $0.385\Phi_0^2$. Typical values for $\Phi_0$ are 0.01-0.1.

Another model is a 2-parameter fluctuation model with a roll-over wave number $k_c$

$$\left|\frac{e\phi}{T_e}\right| = \frac{\Phi_0}{(1+k_\perp^2/k_c^2)^{m/2}}. \tag{4.130}$$

When $k_c^2\rho_s^2 \ll 1$, the spectrum is close to a power law distribution.

## 4.9 Ion Temperature Gradient

Now let us consider a simplified ITG model with impurities, but without ion parallel motion:

$$\frac{\delta n_i}{n_i}\frac{n_i}{n_e} + Z\frac{\delta n_z}{n_z}\frac{n_z}{n_e} = \frac{\delta n_e}{n_e} = \frac{e\phi}{T_e} \tag{4.131}$$

Assuming $T_i \approx T_z$, the linearized equations are:

$$\begin{bmatrix} -1 & \frac{n_i}{n_e} & Z\frac{n_z}{n_e} & 0 \\ -i\omega_{*i} - i\omega_{De} - i\omega k_\perp^2\rho_s^2 + \mu_i k_\perp^4\rho_s^2 & -i\omega - i\omega_{De}\tau_i & 0 & -i\omega_{De}\tau_i \\ -iZ\omega_{*z} - i\omega_{De} - i\omega\frac{A}{Z}k_\perp^2\rho_s^2 + \mu_z\frac{A}{Z}k_\perp^4\rho_s^2 & 0 & -i\omega - i\omega_{De}\tau_z/Z & -i\omega_{De}\tau_z/Z \\ -i\omega_{Ti} - i\frac{2}{3}\omega_{De} & -i\frac{2}{3}\omega_{De}\tau_i & 0 & -i\omega - i\frac{7}{3}\omega_{De}\tau_i \end{bmatrix} \begin{bmatrix} \frac{e\Phi}{T_e} \\ \frac{\delta n_i}{n_i} \\ \frac{\delta n_z}{n_z} \\ \frac{\delta T_i}{T_i} \end{bmatrix} = \begin{bmatrix} 0 \\ 0 \\ 0 \\ 0 \end{bmatrix} \quad (4.132)$$



By eliminating $\delta n_z/n_z$, one gets

$$(-i\omega)\mathbf{A}\mathbf{\Phi} = \mathbf{C}\mathbf{\Phi} \quad (4.133)$$

where

$$\mathbf{A} = \begin{bmatrix} k_\perp^2\rho_s^2 & 1 & 0 \\ \frac{A}{Z}k_\perp^2\rho_s^2 + \frac{1}{Zn_z/n_e} & -\frac{n_i/n_e}{Zn_z/n_e} & 0 \\ 0 & 0 & 1 \end{bmatrix}, \Phi = \begin{bmatrix} \frac{e\phi}{T_e} \\ \frac{\delta n_i}{n_i} \\ \frac{\delta T_i}{T_i} \end{bmatrix} \quad (4.134)$$

and

$$\mathbf{C} = \begin{bmatrix} i\omega_{*i} + i\omega_{De} & i\omega_{De}\tau_i & i\omega_{De}\tau_i \\ iZ\omega_{*z} + i\omega_{De}(1 + \frac{\tau_z}{Z^2 n_z/n_e}) & -i\omega_{De}\frac{\tau_z}{Z^2 n_z/n_e}\frac{n_i}{n_e} & i\omega_{De}\tau_z/Z \\ i\omega_{Ti} + i\frac{2}{3}\omega_{De} & i\frac{2}{3}\omega_{De}\tau_i & i\frac{7}{3}\omega_{De}\tau_i \end{bmatrix}. \quad (4.135)$$

The dispersion relation for ITG modes is shown in Fig. 4.4.

## 4.10 Trapped Electron Mode

Without $\delta T_e$, the trapped electron mode with one impurity is given by

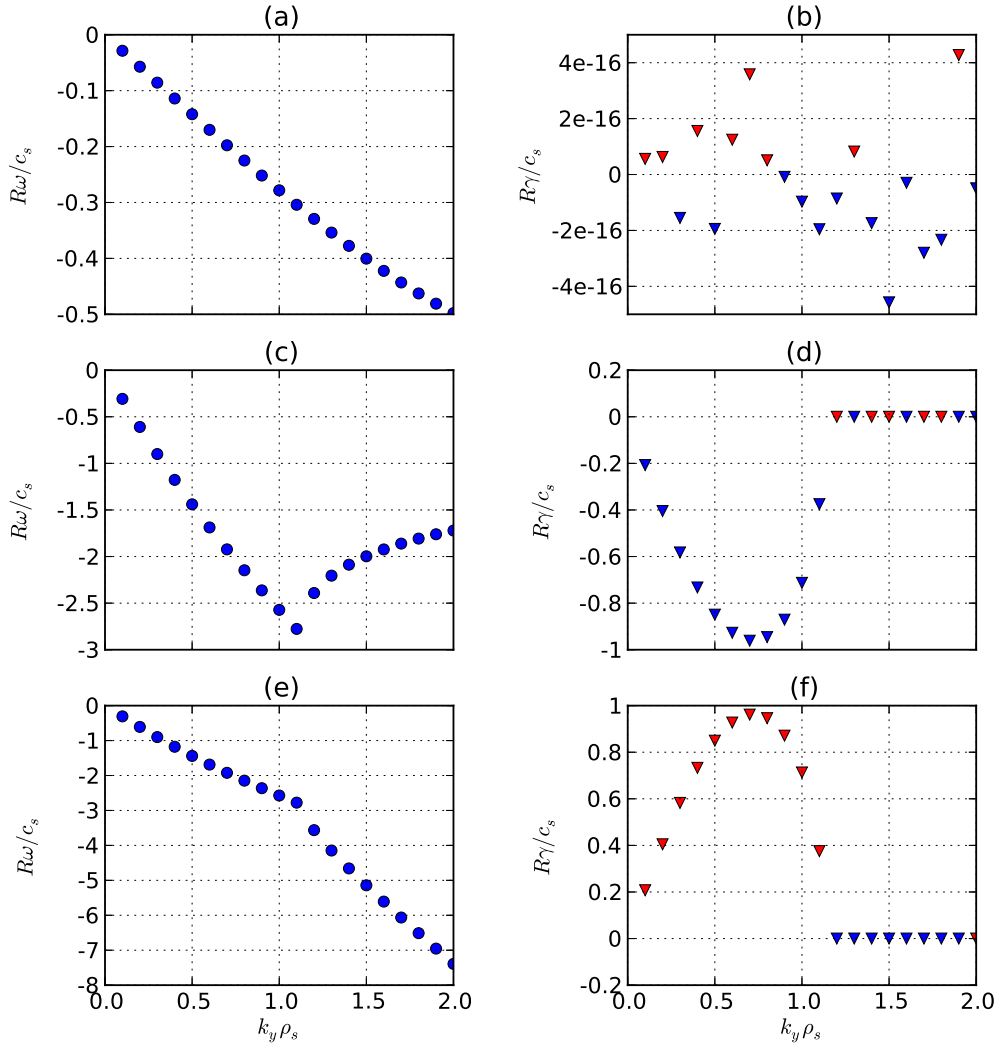


Figure 4.4: The frequencies and growth rates versus $k_y\rho$ for the three modes for the ITG model (same parameters as in Fig. 4.2).

$$\begin{bmatrix} -f_p & \frac{n_i}{n_e} & Z\frac{n_z}{n_e} & -1 \\ -i\omega_{*i} - i\omega_{De} - i\omega k_\perp^2\rho_s^2 + \mu_i k_\perp^4\rho_s^2 & -i\omega - i\omega_{De}\tau_i & 0 & 0 \\ -iZ\omega_{*z} - i\omega_{De} - i\omega\frac{A}{Z}k_\perp^2\rho_s^2 + \mu_z\frac{A}{Z}k_\perp^4\rho_s^2 & 0 & -i\omega - i\omega_{De}\tau_z/Z & 0 \\ i\omega_{*e}f_t + i\omega_{De}f_t & 0 & 0 & -i\omega + i\omega_{De} + \nu_{\text{eff}} \end{bmatrix} \begin{bmatrix} \frac{e\Phi}{T_e} \\ \frac{\delta n_i}{n_i} \\ \frac{\delta n_z}{n_z} \\ \frac{\delta n_t}{n_e} \end{bmatrix} = \begin{bmatrix} 0 \\ 0 \\ 0 \\ 0 \end{bmatrix} \quad (4.136)$$



In order to get the eigenvalues and eigenvectors, we eliminate $\delta n_t/n_e$ and get the following equations in matrix form:

$$(-i\omega)\mathbf{A}\mathbf{\Phi} = \mathbf{C}\mathbf{\Phi} \quad (4.137)$$

where

$$\mathbf{A} = \begin{bmatrix} -f_p & \frac{n_i}{n_e} & Z\frac{n_z}{n_e} \\ k_\perp^2\rho_s^2 & 1 & 0 \\ \frac{A}{Z}k_\perp^2\rho_s^2 & 0 & 1 \end{bmatrix}, \Phi = \begin{bmatrix} \frac{e\phi}{T_e} \\ \frac{\delta n_i}{n_i} \\ \frac{\delta n_z}{n_z} \end{bmatrix} \quad (4.138)$$

and

$$\mathbf{C} = \begin{bmatrix} f_p(\nu_{\text{eff}} + i\omega_{De}) - (i\omega_{*e} + i\omega_{De})f_t & -(\nu_{\text{eff}} + i\omega_{De})\frac{n_i}{n_e} & -(\nu_{\text{eff}} + i\omega_{De})Z\frac{n_z}{n_e} \\ i\omega_{*i} + i\omega_{De} - \mu_i k_\perp^4\rho_s^2 & i\omega_{De}\tau_i & 0 \\ iZ\omega_{*z} + i\omega_{De} - \mu_z\frac{A}{Z}k_\perp^4\rho_s^2 & 0 & i\omega_{De}\tau_z/Z \end{bmatrix} \quad (4.139)$$

Table 4.2: Parameters for C-Mod experiments

| | $T_e$ | $n_e$ | $n_z$ | $R/L_{Te}$ | $R/L_{ne}$ | $R/L_{nz}$ |
|---|---|---|---|---|---|---|
| | keV | $10^{20}\mathrm{m}^{-3}$ | $10^{18}\mathrm{m}^{-3}$ | | | |
| $r/a = 0.3$ | | | | | | |
| H-mode | 1.4 | 2.5 | 0.97 | 3.5 | 0.076 | -6.9 |
| ITB | 1.4 | 3.3 | 2.9 | 3.4 | 2.1 | 3.8 |
| I-mode | 3.1 | 2.1 | 0.33 | 4.4 | 0.53 | 0.57 |
| $r/a = 0.7$ | | | | | | |
| H-mode | 0.76 | 2.4 | 1.9 | 7.7 | 0.65 | 4.2 |
| ITB | 0.78 | 2.5 | 2.8 | 7.9 | 2.1 | -4.1 |
| I-mode | 1.5 | 1.8 | 0.24 | 7.8 | 2.0 | 3.3 |

The dispersion relation of the trapped electron mode (TEM) is

$$\begin{aligned}(-i\omega)^3(-f_p - k_\perp^2\rho_{s,\tau}^2) + (-i\omega)^2[-f_p(i\omega_{*e} + i\omega_{De} + \nu_{\text{eff}}) \\ -(\mu_i k_\perp^4\rho_{s,i}^2 + Z^2\mu_z k_\perp^4\rho_{s,z}^2) - (i\omega_{De} + \nu_{\text{eff}})k_\perp^2\rho_{s,\tau}^2] + \\ (-i\omega)(i\omega_{De} + \nu_{\text{eff}})\left[-i\omega_{*e} - \mu_i k_\perp^4\rho_{s,i}^2 - Z^2\mu_z k_\perp^4\rho_{s,z}^2\right] = 0 \end{aligned} \tag{4.140}$$

To illustrate the applicability of our model, we select three discharges in the high confinement regimes: the EDA H-mode, ITB, and I-mode, typical for C-Mod [21]. Electron density and temperature profiles used here are measured by Thomson Scattering diagnostics [42]. The boron density profiles are measured by the core-CXRS system [59]. The rest of the local parameters were extracted from the C-Mod database. The ion temperature $T_i$ is assumed to be equal to the electron temperature $T_e$, since the collisionality is high and there is no direct measurement of $T_i$. The confinement regimes are characterized by the plasma gradient parameters as follows. (1) For the H-mode, the

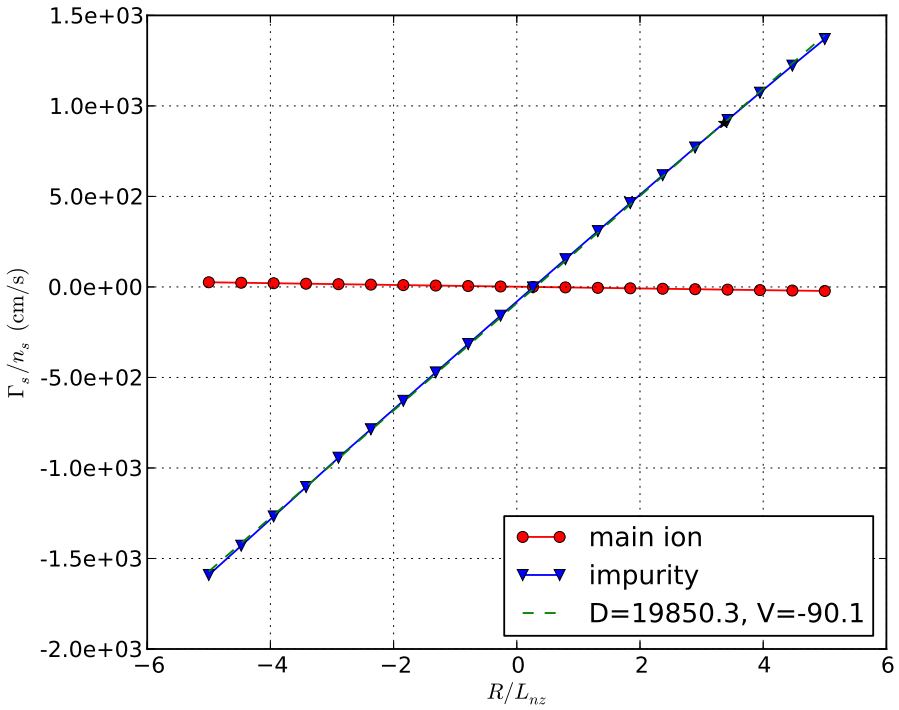


Figure 4.5: Main ion turbulent flux and impurity flux versus impurity density gradients ($R/L_{nz}$) for a set of typical C-Mod parameters, for the ITG mode. From the slope and the intercept of the curve we can extract the transport coefficients $D$ and $V$. The negative values of $R/L_{nz}$ correspond to hollow impurity profiles with inward impurity particle fluxes.

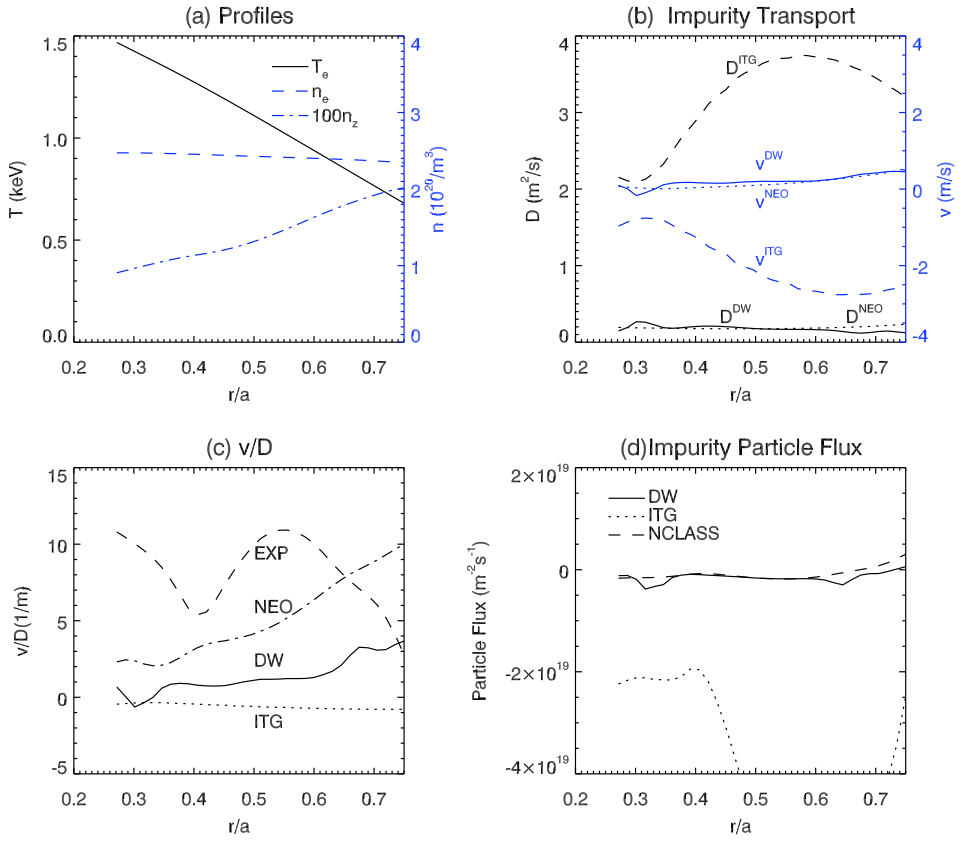


Figure 4.6: C-Mod shot #1070831028 H-mode (a) plasma density, electron temperature, and boron density profiles, (b) calculated diffusion coefficients (black curves) and convection velocity (blue curves), (c) comparison of neoclassical $V/D$ with experimental results ($= -1/L_{nz}$) and (d) neoclassical and turbulent particle fluxes for impurities ("DW" means impurity drift wave, "ITG" means the ITG mode, "NEO" means neoclassical results, and "EXP" means experimental results).

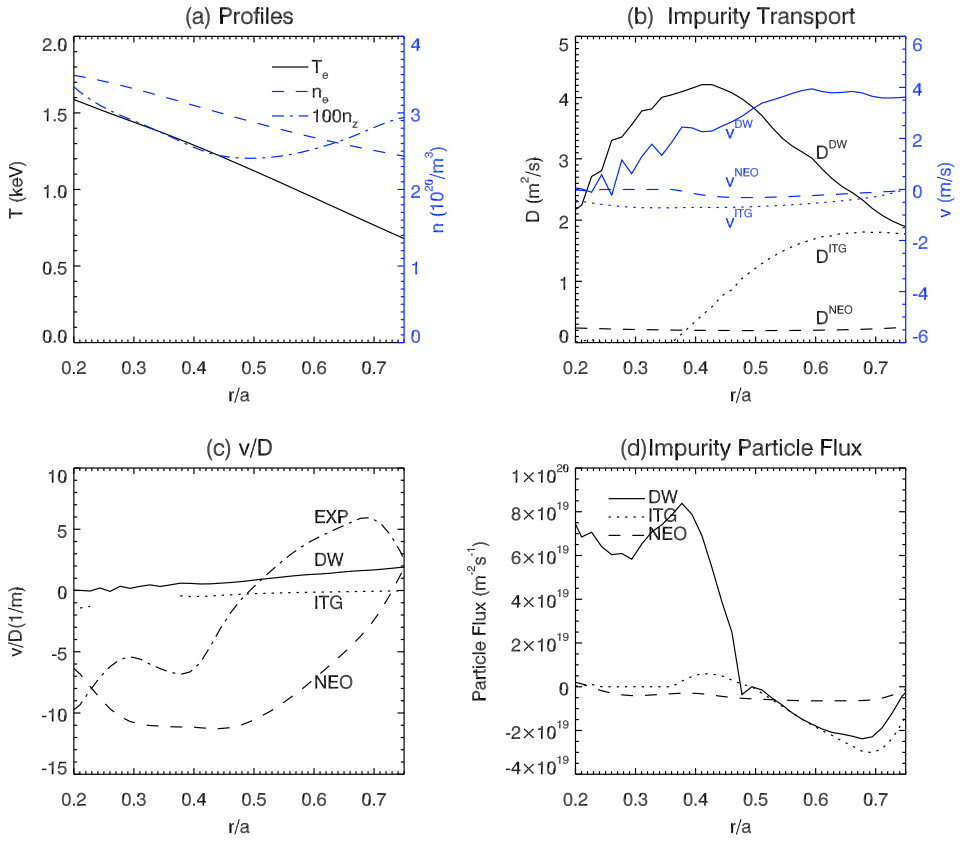


Figure 4.7: C-Mod shot #1070831028 ITB regime (a) plasma density, electron temperature, and boron density profiles, (b) calculated diffusion coefficient and convection velocity, (c) comparison of neoclassical $V/D$ with experimental results and (d) neoclassical and turbulent particle fluxes for impurities (same notation as in Fig. 4.6).

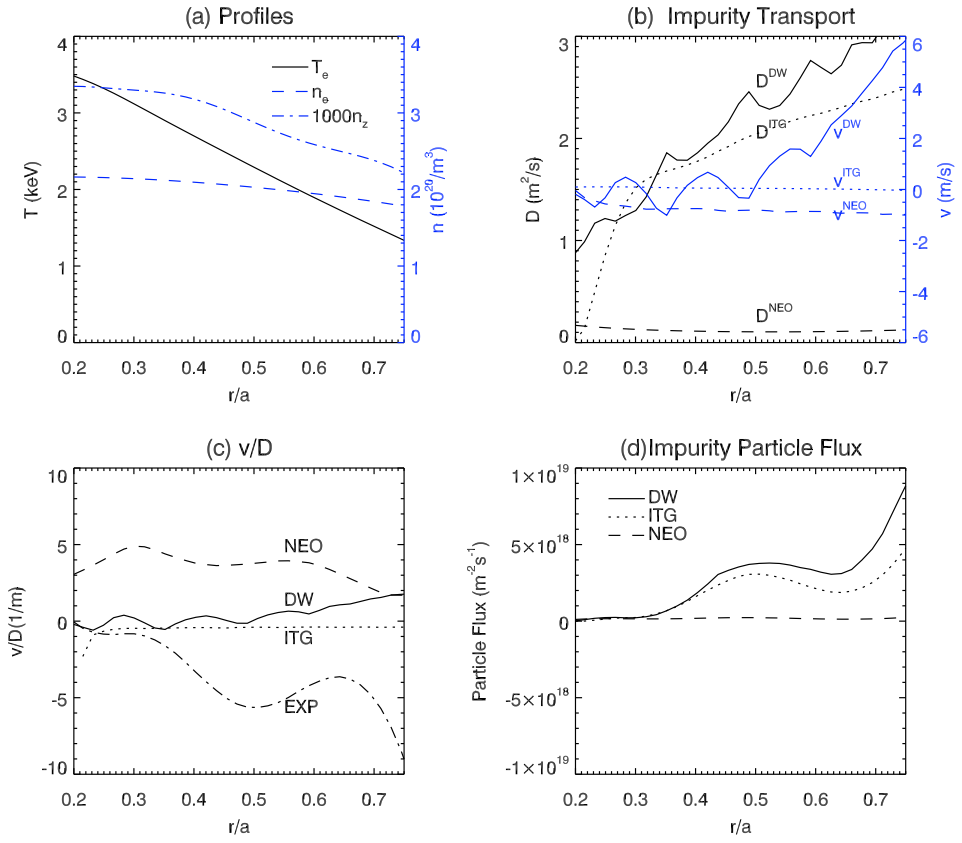


Figure 4.8: C-Mod shot #1101209010 I-mode (a) plasma density, electron temperature, and boron density profiles, (b) calculated diffusion coefficient and convection velocity, (c) comparison of neoclassical $V/D$ with experimental results and (d) neoclassical and turbulent particle fluxes for impurities (same notation as in Fig. 4.6).

electron density profile is flat and the low Z impurity profile is often hollow as shown in Fig. 4.6(a). We take $R/L_{ne} \approx 0$, and $R/L_{nz} = -7$ at $r/a = 0.3$. (2) The ITB profiles have three radial subintervals: inside the barrier, in the barrier ($\rho \approx 0.5$) and outside the barrier. Inside the ITB, both the electron density and the impurity density are strongly peaked with $R/L_{ne} = 3.3$ and $R/L_{nz} = 3.8$ and outside the ITB we take $R/L_{ne} = 2.5$ and $R/L_{nz} = -4.1$, as shown in Fig. 4.7(a). (3) The I-mode, which is a regime of operation recently discovered on C-Mod [41], has an edge thermal transport barrier, but not a particle transport barrier. The I-mode is characterized by H-mode like temperature profiles and L-mode like density profiles. The density gradients are quite flat in the core with $R/L_{ne} = R/L_{nz} = 0.5$ and steep near the edge, as shown in Fig. 4.8(a). The parameter differences between these regimes are listed in Table 4.2.

Figure 4.6(a) shows the profiles of electron density, electron temperature and boron density profiles for the H-mode. Based on these profiles, we estimate the particle diffusivity and the pinch velocity in Fig. 4.6(b). For the neoclassical calculation, we use the NCLASS [39] and NEO codes [7]. The NCLASS code is based on analytic formulae, which do not accurately include plasma shaping or self-consistent interspecies coupling over all collisionality regimes. The NEO code is fully numerical and may provide a more accurate solution for the impurity flux. The results show that at $r/a = 0.6$, the ITG turbulent diffusivity $D^{\mathrm{ITG}} \approx 4\,\mathrm{m}^2/\mathrm{s}$ is significantly larger than the neoclassical diffusivity $D^{\mathrm{NEO}} \approx 0.2\,\mathrm{m}^2/\mathrm{s}$ and the impurity drift wave diffusivity $D^{\mathrm{DW}}$. The

ITG pinch velocity ($V^{\mathrm{ITG}} \approx -2\,\mathrm{m/s}$) is also larger, and in the opposite direction of the neoclassical and impurity drift wave pinch velocities. The ratio of the pinch velocity to the diffusivity (also called "peaking factor") $V/D$ from all models are compared to $-1/L_{nz}$ extracted from the profile in Fig. 4.6(c). Note, one can get the ratio $V/D = -1/L_{nz}$ by assuming zero impurity particle flux. The ITG mode gives a negative $V/D$, while the impurity drift wave gives a positive $V/D$, closer to the ratio inferred from the experiment. Although the impurity fluxes due to the impurity drift wave are smaller than ITG, as shown in Fig. 4.6(d), the impurity drift wave predicts a better peaking factor than ITG. Figure 4.7 shows results for an ITB regime. Similar to the H-mode, the turbulent $D$'s are significantly larger than neoclassical $D$. But in this case, impurity drift wave dominates over ITG for the turbulent flux. Inside ITB $r/a < 0.35$, the ITG mode is suppressed, but the impurity drift wave is very strong. The quantity $V/D$ from the impurity drift wave matches the experiment at about $r/a = 0.5$. In Fig. 4.8, we analyze an I-mode shot. The impurity drift wave and the ITG turbulences are now comparable. The ITG turbulence gives a negative $V/D$ ratio, which is closer to the experiment, as shown in Fig. 4.8(c). This suggest that in the I-mode, ITG may be the dominant mode responsible for the anomalous transport.

Many authors (e.g.[1]) discuss the effect of different modes on the direction of the pinch velocity. We also see in our calculations that, in some regimes, the impurity drift wave model predicts a pinch velocity in the opposite direction to the ITG pinch velocity. However the contributions from

different modes are determined by their fluctuation levels, which cannot be determined by quasilinear theory. And, the coupling between different modes needs to be addressed by constructing a complex model including all possible modes.

Recent impurity transport experiments on LHD [69] show that when strong ion heating is applied to the plasma, carbon impurity is pushed outward and a hollow carbon profile forms. The change of the peaking factor can be understood from the transport coefficients for the impurity given by

$$D_z = c_s^2 \sum_k (k_y \rho_s)^2 \frac{\gamma}{\omega_r^2} (1 + \frac{2}{\omega_r} k_y v_{Dz}) \left| \frac{e\phi_k}{T_e} \right|^2 \tag{4.141}$$

$$V_z = c_s \sum_k (k_y \rho_s) \frac{\gamma}{\omega_r^2} \left[ \frac{cT_e}{eB} \frac{k_y}{L_{T_z}} \frac{2}{\omega_r} k_y v_{Dz} - k_y v_{De} \right] \left| \frac{e\phi_k}{T_e} \right|^2, \tag{4.142}$$

where $\gamma(k) \ll \omega_r(k)$ is used. The two terms in Eq. (4.142) are competing to determine the direction of pinch velocity. If we take $\omega_r$ from Eq. (4.74), the pinch $V_z$ changes for inward to outward when

$$\frac{R}{L_{Ti}} > \frac{ZT_e}{T_i} \left( 1 + \frac{T_i}{T_e} - \frac{R}{2L_{ne}} \right), \tag{4.143}$$

assuming $T_z \approx T_i$. However the parameters for C-Mod and LHD are different, as listed in Table 4.3. Further studies of LHD data are ongoing.

## 4.11 Conclusions

We have developed codes for solving systems of drift wave turbulence equations for multi-component fusion plasmas and for calculating quasilinear

Table 4.3: Comparison of C-Mod and LHD parameters

| | C-Mod | LHD |
|---|---|---|
| Major Radius $R$ | 0.67 m | 3.6 m |
| Minor Radius $a$ | 0.22 m | 0.4 m |
| Magnetic field $B$ | 5 T | 2 T |
| Electron Temperature $T_e$ | 3 keV | 1 keV |
| Plasma Density $n_e$ | $10^{20}\,\mathrm{m}^{-3}$ | $10^{19}\,\mathrm{m}^{-3}$ |
| Impurity | $B^{5+}$ | $C^{6+}$ |
| $Z_{\mathrm{eff}}$ | 1.1 | 1.6 |

particle fluxes. The calculations are much faster than nonlinear simulations and may be suitable for real-time analysis and feedback control of tokamak plasmas.

We used an analytic model (motivated by nonlinear simulations) of the potential spectrum along with the polarization eigenvectors from the linear eigenmodes to compute the diffusivities and convection velocities as a function of plasma parameters. Our calculations for the C-Mod H-mode, I-mode, and ITB regime shots show that turbulent impurity diffusivity $D_z$ from impurity drift wave and ITG mode are a order of magnitude larger than the neoclassical results. The pinch velocity $V_z$ predicted by two turbulent models shows different character in different confinement regimes. For the hollow profiles in H-mode plasmas and the outer region of the ITB regime, the impurity drift wave gives a better prediction of the $V/D$ ratio, while in the I-mode, the ITG mode works better. We also find for all regimes, when turbulent flux drops, the $V/D$ from experiments gets closer to the neoclassical $V/D$.

In the current work, we considered mainly the density gradient driven

mode and the ITG mode for impurity transport. However, the code can be extended to include more modes and couple them together to get a more complete description of the turbulence in the plasma. There is also an intrinsic rotation for ICRF heated plasmas that generates a radial electric field, as shown in Ref. [18]. The strong $E_r$-shear can suppress the turbulent transport (see Chapter 3). The effect of $E_r$-shear will be included in the future. Measurement of impurity profiles with high time resolution will help better understand the impurity transport and enable direct comparison between experiment and theory. Lastly, the validity of our quasilinear models can be also checked by nonlinear simulations.

# Chapter 5

# Electrostatic Electron Temperature Gradient Mode

The standard model for universal turbulent electron transport across various magnetic confinement geometries is the electron temperature gradient (ETG) form of drift wave turbulence. The driving mechanism for this turbulence is the electron temperature gradient and the physical mechanism can be understood in terms of a Carnot cycle made up from the $\mathbf{E} \times \mathbf{B}$ convection of the plasma in drift wave vortices [37]. The ETG instability involves convection of the thermal electron distribution and does not require a magnetically trapped electron distribution. The electron temperature gradient is expressed by $dT_e/dr = -T_e/L_{Te}$ where $L_{Te}$ is the local electron temperature gradient scale length. The instability is robust with a fast growth rate on the order of a few tenths of $v_{te}/L_{Te}$ (when $k_\perp \lambda_{De} << 1$), where $v_{te}$ is the electron thermal velocity. The resulting turbulence has been used to explain electron transport in many tokamak confinement systems including NSTX[34, 43], Tore-Supra[30], and TCV[3]. However, the fluctuations in these experiments were not directly measured. Recently, Mazzucato et al. [52] used reflectometry in NSTX to measure part of the $k$-spectrum for ETG.

## 5.1 Kinetic theory for the ETG mode

The ETG mode can be derived from reduced fluid equations, drift kinetic equations, and gyrokinetic equations. There are both electrostatic and electromagnetic version of ETG modes, and the geometry of the background magnetic field lines also plays an important role in determining the properties of the modes (e.g. the threshold for instability). In this section, we will derive a simple drift-kinetic model for the slab ETG.

The drift-kinetic equation for electrons reads

$$\frac{\partial f_e}{\partial t} + \mathbf{v}_E \cdot \nabla f_e + v_z \frac{\partial f_e}{\partial z} - \frac{e}{m_e} E_z \frac{\partial f_e}{\partial v_z} = 0 \tag{5.1}$$

Assuming a Maxwellian distribution for electrons, $f_{e0} = n_{e0} \left(\frac{m}{2\pi T_{e0}}\right)^{3/2} e^{-\frac{m}{2T_{e0}}(v_\perp^2 + v_z^2)}$, with inhomogeneity in $x$-direction

$$\frac{df_{e0}}{dx} = f_{e0} \left[ \frac{dn_{e0}}{dx} \frac{1}{n_{e0}} + \left( \frac{m_e(v_\perp^2 + v_z^2)}{2T_{e0}} - \frac{3}{2} \right) \frac{dT_{e0}}{dx} \frac{1}{T_{e0}} \right], \tag{5.2}$$

and integration of the distribution function over $v_\perp$ gives

$$\iint f_{e0} 2\pi v_\perp dv_\perp dv_z = \iint f_{e0} \left( \frac{m_e v_\perp^2}{T_{e0}} \right) 2\pi v_\perp dv_\perp dv_z = \int F_{e0} dv_z, \tag{5.3}$$

where the 1-D Maxwellian distribution is

$$F_{e0} = n_{e0} \left( \frac{m_e}{2\pi T_{e0}} \right)^{1/2} e^{-m_e v_z^2 / 2T_{e0}}. \tag{5.4}$$

Using

$$\frac{\partial f_{e0}}{\partial v_z} = -f_{e0} \frac{m_e v_z}{T_{e0}}, \tag{5.5}$$

we obtain the linear response of electron density induced by the electrostatic potential $\phi$,

$$\delta n_e = \frac{e\phi}{T_e}\int 1 - \frac{\omega - k_y v_{*e}\left[1+\eta_e\left(\frac{m_e v_z^2}{T_{e0}}-\frac{1}{2}\right)\right]}{\omega - k_z v_z} F_{e0} dv_z. \tag{5.6}$$

The integral over the singular point can be represented by the plasma dispersion function

$$\int_{-\infty}^{+\infty} \frac{F_{e0}dv_z}{\omega - k_z v_z} = -\frac{n_{e0}}{|k_z|v_{te}} Z\left(\frac{\omega}{|k_z|v_{te}}\right), \tag{5.7}$$

where $v_{te} = \sqrt{2T_{e0}/m_e}$, and

$$\begin{aligned}
&\int_{-\infty}^{+\infty} \frac{F_{e0} 2v_z^2/v_{te}^2}{\omega - k_z v_z} dv_z \\
= &\sqrt{\frac{m}{2\pi T_{e0}}}\frac{2n_{e0}}{k_z^2 v_{te}^2}\int_{-\infty}^{+\infty} \frac{(\omega - k_z v_z)^2 + 2\omega(k_z v_z - \omega) + \omega^2}{\omega - k_z v_z} e^{-\left(\frac{v_z}{v_{te}}\right)^2} dv_z \\
= &-\frac{2n_{e0}}{k_z^2 v_{te}^2}\left[\omega + \frac{\omega^2}{|k_z|v_{te}} Z\left(\frac{\omega}{|k_z|v_{te}}\right)\right].
\end{aligned} \tag{5.8}$$

Therefore the electron response is given by

$$\begin{aligned}
\delta n_e = \frac{e\phi n_{e0}}{T_{e0}}\Bigg[1 + &\frac{\omega - \omega_{*e}(1-\eta_e/2)}{|k_z|v_{te}} Z\left(\frac{\omega}{|k_z|v_{te}}\right) \\
&-\frac{\eta_e \omega_{*e}}{|k_z|v_{te}}\left(\frac{\omega}{|k_z|v_{te}} + \frac{\omega^2}{k_z^2 v_{te}^2} Z\left(\frac{\omega}{k_z v_{te}}\right)\right)\Bigg].
\end{aligned} \tag{5.9}$$

We can obtain similar results for ions from the drift-kinetic equation, except that ion finite Larmor radius effects should be kept for modes with $k_\perp \rho_i \gtrsim 1$. Any field $f$ averaged over an ion gyro-orbit is reduced by a factor of $J_0$:

$$\langle f \rangle = \sum_k f_k J_0(k_\perp \rho_i) e^{i\mathbf{k}\cdot\mathbf{x}_{\rm gc}}. \tag{5.10}$$

Since both the distribution function of ions $f_i$ and the electric potential $\phi$ are reduced, the ion response (without ion temperature gradient effect) is given by

$$\delta n_i = -\frac{e\phi n_{i0}}{T_{e0}}\left[\tau + \frac{\tau\omega + \omega_{*e}}{|k_z|v_{ti}} Z\left(\frac{\omega}{|k_z|v_{ti}}\right) I_0(b_i) e^{-b_i}\right], \tag{5.11}$$

where $b_i = k_\perp^2 \rho_i^2/2$, and $\tau = T_{e0}/T_{i0}$.

The dispersion relation is then

$$\begin{aligned} D(\mathbf{k},\omega) = 1 + k^2\lambda_{De}^2 + \frac{\omega - \omega_{*e}(1-\eta_e/2)}{|k_z|v_{te}} Z\left(\frac{\omega}{|k_z|v_{te}}\right) \\ -\frac{\eta_e\omega_{*e}}{|k_z|v_{te}}\left[\frac{\omega}{|k_z|v_{te}} + \frac{\omega^2}{k_z^2 v_{te}^2} Z\left(\frac{\omega}{|k_z|v_{te}}\right)\right] \\ +\tau + \frac{\tau\omega + \omega_{*e}}{|k_z|v_{ti}} Z\left(\frac{\omega}{|k_z|v_{ti}}\right) I_0(b_i) e^{-b_i} = 0. \end{aligned} \tag{5.12}$$

Similar dispersion relations for ETG with electron finite Larmor radius effects and adiabatic ions can be found in [45].

Now let us consider some limits. First, when $|\omega| \gg |k_z|v_{te} \gg |k_z|v_{ti}$, with the asymptotic property of $Z$-function $Z(\zeta) \approx -1/\zeta(1 + 1/2\zeta^2 + \dots)$ when $|\zeta| \gg 1$, we find the dispersion relation

$$-\frac{k_z^2 v_{te}^2}{2\omega^2}\left[1 - \frac{\omega_{*e}}{\omega}(1-\eta_e/2)\right] + \frac{\omega_{*e}}{\omega} + \tau = 0 \tag{5.13}$$

or

$$\tau\omega^3 + \omega^2\omega_{*e} - \frac{k_z^2 v_{te}^2}{2}\omega = \frac{k_z^2 v_{te}^2}{2}\omega_{*e}(\frac{\eta_e}{2} - 1). \tag{5.14}$$

The three roots of this dispersion relation as a function of $\eta_e$ are plotted in Fig. 5.1 with frequencies normalized to $v_{te}/L_{ne}$. Notice that only the solution

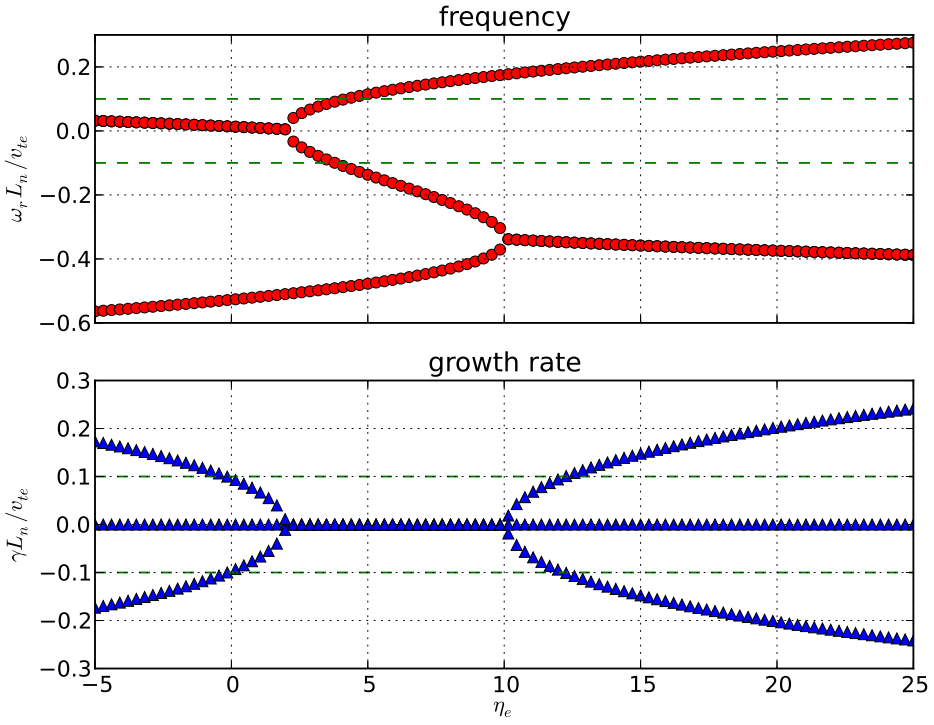


Figure 5.1: The frequency and growth rate of ETG as a function of $\eta_e$ using Eq. (5.14). The parameters are $k_y\rho_e = 0.5$, $k_z\rho_e = 0.01$, $\rho_e/L_{ne} = 0.1$. The dashed lines in the upper and lower panels show $|\omega_r| = k_z v_{te}$ and $|\gamma| = k_z v_{te}$, respectively.

with $|\omega| \gg |k_z| v_{te}$ is consistent with the high frequency assumption. In the limit of $k_z = 0$, we get basic drift waves with $\omega = -\omega_{*e}/\tau = \omega_{*i}$.

Next, we examine the usual drift wave with $|k_z| v_{te} \gg |\omega| \gg |k_z| v_{ti}$. To the first order approximation for both ion and electron response, we find the dispersion relation

$$1 + k^2 \lambda_{De}^2 + i\sqrt{\pi} \frac{\omega - \omega_{*e}(1 - \eta_e/2)}{|k_z| v_{te}} - \frac{\omega_{*e}}{\omega} - \frac{k_z^2 c_s^2}{\omega^2} = 0 \qquad (5.15)$$

where we also assume $\tau \gg 1$ and $\omega \approx \omega_{*e}$. A similar result is given in [24] chap 26.4. The ion acoustic wave $\omega^2 = k_z^2 c_s^2 / (1 + k^2 \lambda_{De}^2)$ can be easily recovered by setting $\omega_{*e} = 0$.

## 5.2 ETG modes in the CLM experiments

Basic steady-state university-scale hydrogen plasma experiments on the Columbia linear machine (CLM) have been carried out. These experiments directly measure fluctuations with specially designed low capacitance probes that allow the measurement of plasma potentials up to MHz frequencies. The conditions for the ETG instability are created uses a new kind of plasma source that has a two-part acceleration/heating mesh with a higher and variable voltage on the inner disk mesh $r < r_1$ and lower voltage on the outer ring mesh $r_1 < r < a$. This arrangement allows the formation of electron temperature profiles with a continuous range of temperature gradient scale lengths $L_{Te}$. The plasma density profile can be maintained as flat in the CLM, which simplifies the theory of the ETG instability. Using high speed data acquisition equip-

| | |
|---|---|
| Machine Length | $L = 150$ cm |
| Minor radius | $a = 3.3$ cm |
| Electron Temperature (on axis) | $T_{e0} = 16.5$ eV |
| Ion Temperature | $T_i = 3.1$ eV |
| Electron Density | $n_e = 3.2 \times 10^9$ cm$^{-3}$ |
| Magnetic Field | $B = 1000$ G |
| Electron Temperature Scale Length (r=1.8 cm) | $L_{Te} = 0.33$ cm |
| Parallel Wave Number | $k_z = 0.003$ cm$^{-1}$ |
| Electron Gyro-frequency | $\omega_{ce} = 1.76 \times 10^{10}$ rad/s |
| Plasma Frequency | $\omega_{pe} = 3.09 \times 10^9$ rad/s |
| Electron Thermal Velocity (on axis) | $v_{te0} = 1.70 \times 10^8$ cm/s |
| Ion Sound Speed | $c_s = 3.97 \times 10^6$ cm/s |
| Electron Gyro-radius (on axis) | $\rho_{e0} = 0.0097$ cm |
| Ion Gyro-radius | $\rho_i = 0.18$ cm |
| Debye Length (on axis) | $\lambda_{De0} = 0.055$ cm |

Table 5.1: Machine and plasma parameters for a typical ETG experiment in the Columbia Linear Machine.

ment, Wei et al. [65] obtain steady-state fluctuation data and report that the spectrum is consistent with the ETG instability. In Table 5.1 we summarize the parameters of the CLM hydrogen plasma used in these experiments.

As we will show, the fluctuations in the rest frame of the plasma are in the range of 100-500 kHz and the wavenumbers are high, ranging up to $k_y\rho_e \sim 0.5$ for the fastest growing modes in the case of sharp electron temperature gradients. However, the probe data show that fluctuations with much longer wavelengths dominate the spectrum; thus, there is clearly a need for nonlinear simulations of the system to understand the experimental data.

The CLM is a cylindrical linear machine that is capable of producing steady-state collisionless hydrogen plasmas confined by an external magnetic

field. The plasma is produced by a DC discharge in the source region. To heat the electrons a tungsten mesh is biased in the transition region with a suitably positive potential to accelerate the plasma electrons. These electrons then thermalize on the neutrals to create a higher temperature in the center ($\sim 15$ eV) relative to the edge ($< 1\,\mathrm{eV}$) and create a sharp electron temperature gradient. The resulting low density hydrogen plasma ($\sim 10^9/\mathrm{cm}^3$) flows into the experiment (central) cell which is about 1.5 m long and 3 cm in radius and immersed in a 0.1 T homogeneous magnetic field. Ion temperature remains low ($\sim 2$ eV). The relevant parameters are summarized in Table 5.1 and the radial profiles of plasma density $n_e(r)$, electron temperature $T_e(r)$ and ion temperature $T_i(r)$ obtained are shown in Fig. 5.2(a). The density profile is almost flat in the region of turbulence.

Specially designed high-resolution twin Langmuir probes are placed inside the plasma to measure the electric potential. The power spectrum of signals from the twin probes is shown in Fig. 5.2(b). When the electron temperature gradient is above a threshold ($L_{T_e} < 0.428\,\mathrm{cm}$), strong signals are found around 2.2 MHz. After subtracting the $\mathbf{E} \times \mathbf{B}$ rotational frequency due to the bias potential, the frequency of the mode in the plasma rest frame is about 0.3 MHz. The radial profiles of potential fluctuation are measured and show that the maximum fluctuation is located close to the point of the sharpest electron temperature gradient (smallest $L_{Te}$), as in Fig. 5.3. Detailed analysis of the signals shows that three azimuthal modes $m = 14, 15, 16$ are dominant in the steady-state fluctuation signal [65].

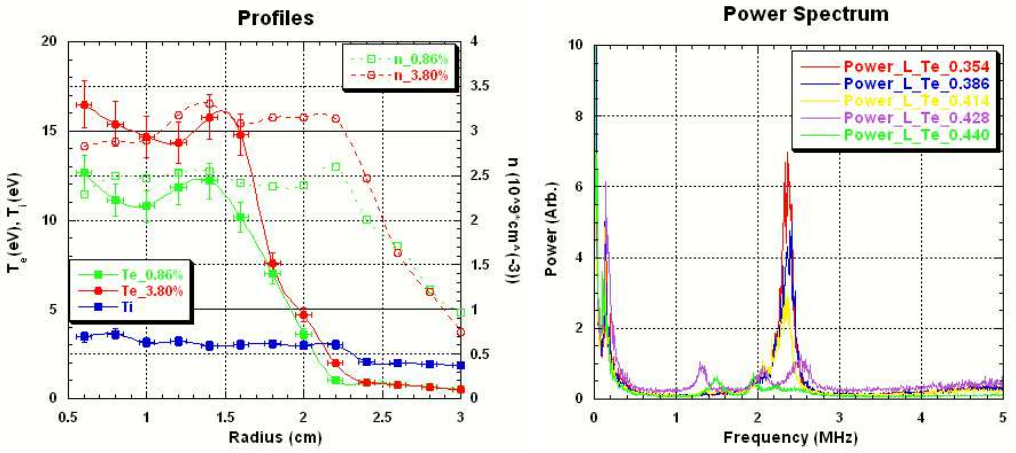


(a) (b)

Figure 5.2: (a) Radial profiles of electron temperature $T_e$, ion temperature $T_i$ and plasma density $n_e$ measured in the CLM. Two sets of data with two different bias voltages (thus different temperature gradients) are shown. A strong electron temperature gradient is produced between $r = 1.5\,\text{cm}$ and $r = 2.2\,\text{cm}$. Note that the density in the region of $1.5\,\text{cm} < r < 2.2\,\text{cm}$ is nearly flat. The electron velocity distribution is close to a local Maxwell-Boltzmann distribution with the temperature $T_e(r)$ and a constant electron density $n_e$. The ion temperature is also constant and less than 1/5 the electron temperature. (b) The power spectra of the signals picked up by a high frequency probe are recorded for various temperature gradients ($a/L_{T_e}$). For strong enough temperature gradient, $L_{T_e} < 0.428\,\text{cm}$, signals are found to be peak around 2.4 MHz in the laboratory frame. Reprinted with permission from Wei et al. [65]. Copyright 2010 American Institute of Physics.

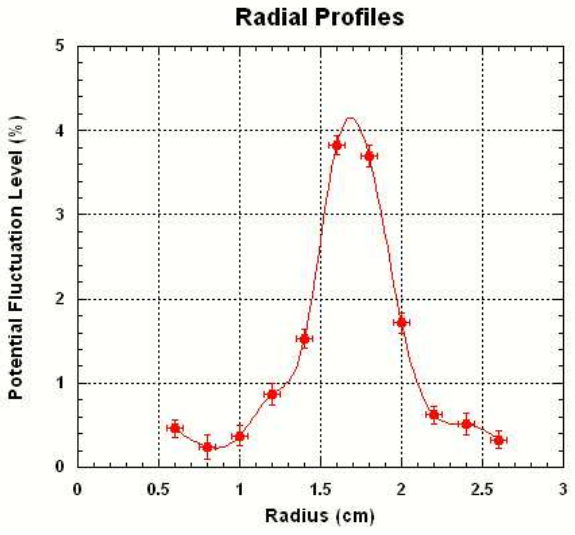


Figure 5.3: The radial profile of the electric potential fluctuation measured in the CLM, peaking around $r = 1.7\,\mathrm{cm}$. Reprinted with permission from Ref. [65]. Copyright 2010 American Institute of Physics.

## 5.3 Linear Properties of ETG Modes in a Cylinder

In this section we will report on the linear properties of ETG modes for the CLM plasma. The linear properties of ETG modes have been studied throughly and the dispersion relation of the slab ETG mode in the fluid limit with no density gradient is given by [45]:

$$\left[\frac{T_e}{T_i} + (k_\perp \lambda_{De})^2 + \frac{k_\perp^2 \rho_e^2}{2}\right] \left(\frac{\omega}{\omega_{ce}}\right)^3 + \frac{k_\perp^2 \rho_e^2}{2} k_y \rho_e \frac{\rho_e}{L_{Te}} \left(\frac{\omega}{\omega_{ce}}\right)^2 + \left(\frac{k_\perp^2 \rho_e^2}{4} - \frac{1}{2}\right) (k_\parallel \rho_e)^2 \left(\frac{\omega}{\omega_{ce}}\right) + \frac{1}{4}\left(1 + \frac{k_\perp^2 \rho_e^2}{2}\right) k_y \rho_e \frac{\rho_e}{L_{Te}} (k_\parallel \rho_e)^2 = 0. \quad (5.16)$$

This slab model is equivalent to the toroidal ETG mode (e.g. [33]) in the limit of large toroidal curvature $R/L_{T_e}$ and large safety factor $q = rB_t/RB_p$. We use these limits in simulating the cylindrical CLM plasma by the toroidal

GTC code.

We solved the cubic dispersion relation of Eq. (5.16) for eigenmodes for CLM parameters and plot the results in Fig. 5.4. Three modes (roots) exist and the unstable Mode 2 is the source of turbulence. The remaining modes are damped and may absorb wave energy received by the nonlinear transfer from the unstable mode. In the plasma rest frame the frequency of the most unstable mode is $\omega \approx 1.5 \times 2\pi\,\mathrm{MHz}$ with wave number $k_y\rho_e \approx 0.3$, or the poloidal wave number $m \approx 70$. In the laboratory frame the plasma is rotating so the corresponding laboratory frequency is $\omega_{\mathrm{lab}} = m\Omega + \omega(\mathbf{k})$, where $\Omega \equiv E_r/(rB) \sim 2\pi \times 130\,\mathrm{kHz}$ for nearly rigid-body rotation.

## 5.4 Gyrokinetic Simulations using GTC code

Gyrokinetic Toroidal Code (GTC) [31] is a sophisticated massively-parallel gyrokinetic particle simulation code, which has been successful in simulating toroidal ITG, CTEM, toroidal ETG, Alfvén eigenmodes, and other plasma phenomena[47, 68, 48, 15]. We adapt the toroidal GTC code to study the cylindrical plasmas by taking the limit of infinite constant $q$ and setting the equivalent major radius $R_0 \gtrsim 1/k_\parallel$. In this section, we will first focus on results for the set of parameters listed in Table 5.1, and later do a parametric scan of the $T_e$ gradient and parallel wave number $k_\parallel$ [22].

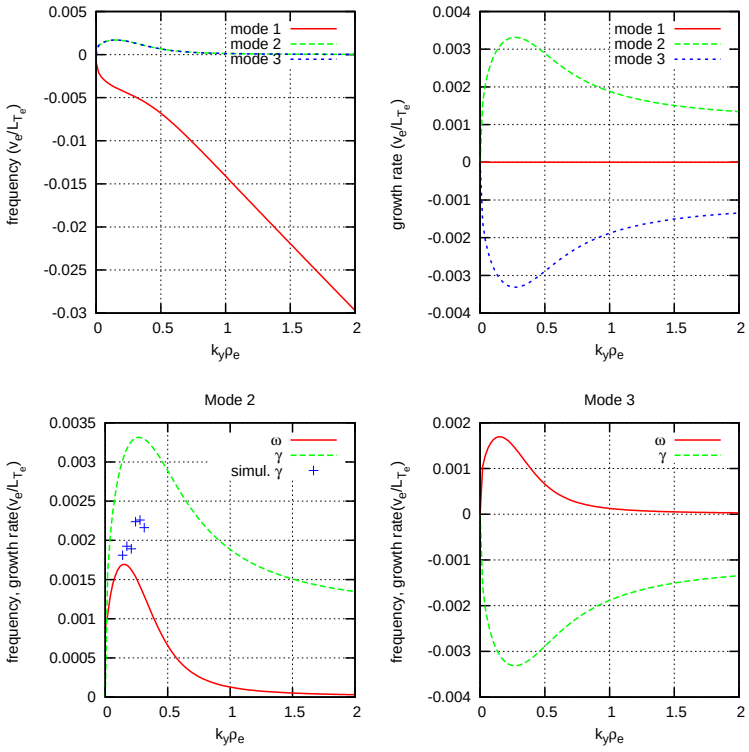


Figure 5.4: The dispersion relation of the slab ETG mode without density gradient, given by Eq. (5.16). There are three modes: mode 1 is purely damping; mode 2 and mode 3 are complex conjugates. We are interested in the unstable mode 2, whose growth rate is larger than the frequency. The growth rates obtained from linear simulations are shown as blue crosses.

### 5.4.1 Numerical Results

Based on the parameters in Table 5.1, the time and space units in the code are normalized as

$$t \to tc_{s,e}/R_0, \;\; l \to l/R_0, \tag{5.17}$$

where $R_0 = 300\,\mathrm{cm}$ and $c_{s,e} = \sqrt{T_i/m_e} \approx 7.27 \times 10^7\,\mathrm{cm/s}$. The time step $t_0 = 0.0025 \times c_{s,e}/R_0 \approx 10^{-8}\,\mathrm{s}$. For a typical run, we employ approximately $150 \times 600 \times 32$ (in the radial, poloidal, and toroidal direction, respectively) cells and 1000 electrons per cell. This corresponds to a perpendicular spatial resolution of $\sim 0.35\rho_{e0}$. It takes about ten hours to run on NERSC Hopper or TACC Ranger with 2048 nodes for simulating 8000 time steps.

In our simulation model, electrons are advanced by the electrostatic gyrokinetic equation using the $\delta f$ algorithm [31]

$$\frac{dw_e}{dt} = (1 - w_e)\left[-\mathbf{v}_E \cdot \frac{\nabla f_{0e}}{f_{0e}} - (e\mathbf{b} \cdot \nabla\phi)\,\frac{1}{m_e}\frac{1}{f_{0e}}\frac{\partial f_{0e}}{\partial v_\parallel}\right], \tag{5.18}$$

where $w_e \equiv \delta f_e/f_{0e}$ and $f_{0e}$ is the background electron distribution function. Ions are treated as adiabatic

$$\frac{\delta f_i}{f_i} = -\frac{e\phi}{T_i}. \tag{5.19}$$

which is valid when $k_\perp \rho_i \gg 1$. The boundary condition in the $z$ direction (along $\mathbf{B}$ field) is periodic, and the electric potential $\phi$ vanishes at the inner ($r/a = 0.2$) and outer ($r/a = 0.8$) radii.

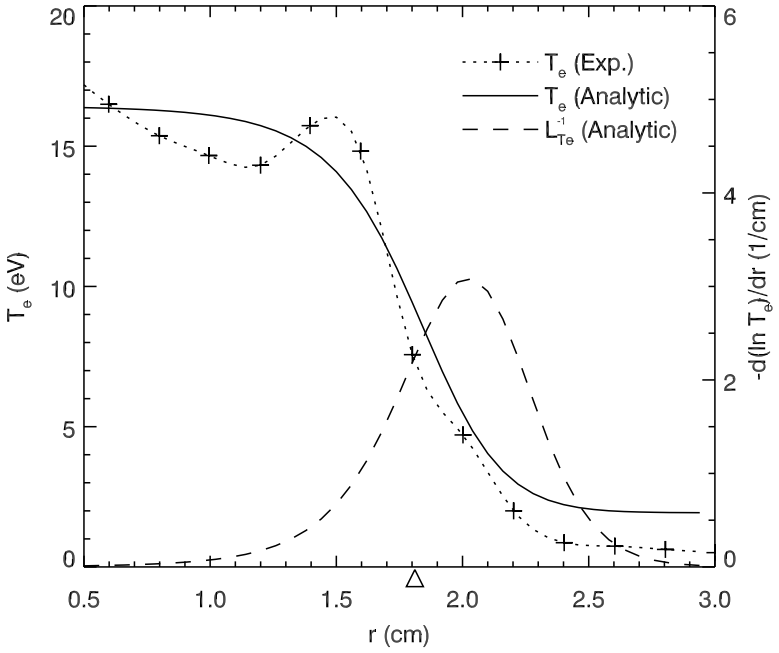


Figure 5.5: The electron temperature profile for GTC simulations. The experimental results are shown as the dotted curve with plus signs. The analytic model is depicted by the solid curve, and the dash curve is its inverse scale length $1/L_{Te}$. The triangle marks the radial position of the maximum gradient of the model.

#### 5.4.1.1 Modeling electron temperature and density profiles

As shown in Fig. 5.5, the background temperature profile used in the simulations are modeled by the analytic formula

$$T_e = T_{e0}\left(1 + c_1\left[\tanh\left(\frac{c_2 - r^2/a^2}{c_3}\right) - 1\right]\right), \tag{5.20}$$

with $[c_1, c_2, c_3] = [0.44, 0.36, 0.14]$, where $c_2$ controls the position of the steepest gradient, $c_3$ controls the width of the temperature drop, and $c_1$ controls the temperature at the edge (with the core temperature $T_{e0}$ fixed). This background profile is fixed during the simulation. For the density, we use a flat profile, i.e. $n_e(r) = \text{const}$. The maximum temperature gradient is located at $r = 1.8\,\text{cm}$, but $L_{T_e}^{-1}$ peaks at $r = 2.1\,\text{cm}$ with a minimum $L_{T_e} \approx 0.3\,\text{cm}$, where the linear growth rate is largest. The drift frequency at this peak is

$$\omega_{*Te} \;=\; k_y \rho_e v_{te}/L_{Te} = m \times 2\pi \times 0.193 \;\; \text{MHz}. \tag{5.21}$$

#### 5.4.1.2 Time history of the simulation

Figure 5.6 shows the time history of the averaged electric potential fluctuation and electron energy flux. It is clear that during $0 < t < 2200t_0$, both quantities grow exponentially, corresponding to a linear stage. The growth rates for a few modes obtained from the simulations are shown in Fig. 5.4 as blue crosses. Thereafter, the ETG modes saturate and when $t > 4000t_0$ they enter a quasi-steady state.

Two contours of the electric potential at $t = 2000t_0$ and $t = 4000t_0$ are shown in Fig. 5.7 representing a typical linear and nonlinear case respectively.

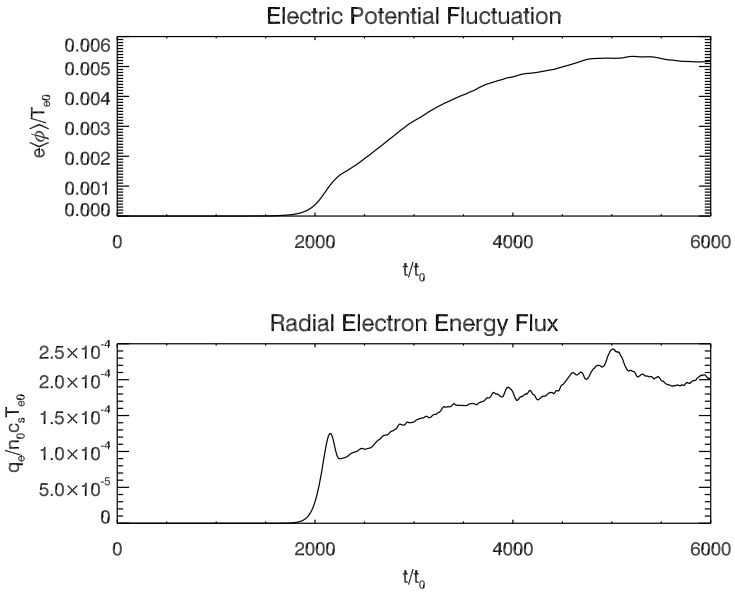


Figure 5.6: The time evolution of the root-mean-square of the electric potential $\langle\phi\rangle = \int_V \sqrt{\phi^2} d^3r / \int_V d^3r$, and the radial electron energy flux $q_e = \int\int \frac{cE_\theta}{2B} m_e(v^2 - v_0^2)\delta f d^3v d^3r / \int_V d^3r$.

Strong nonlinear effects cause inverse cascading, with energy transfer from short poloidal wave length (large $m$ number) modes to long wave length modes (small $m$ number). The power spectra of signals measured at $r = 1.88\,\text{cm}$ for $t = 2000t_0$, $t = 2400t_0$, $t = 3200t_0$, and $t = 4000t_0$ are shown in Fig. 5.8.

#### 5.4.1.3 Time history of two modes

The time history of two modes $m = 15$ and $m = 60$ are shown in Fig. 5.9. The mode with $m = 60$ is the fastest growing mode at the late linear stage and $m = 15$ is the dominant mode in the nonlinear stage. The frequency of the $m = 15$ mode in the plasma frame is about 0.24 MHz, close to the

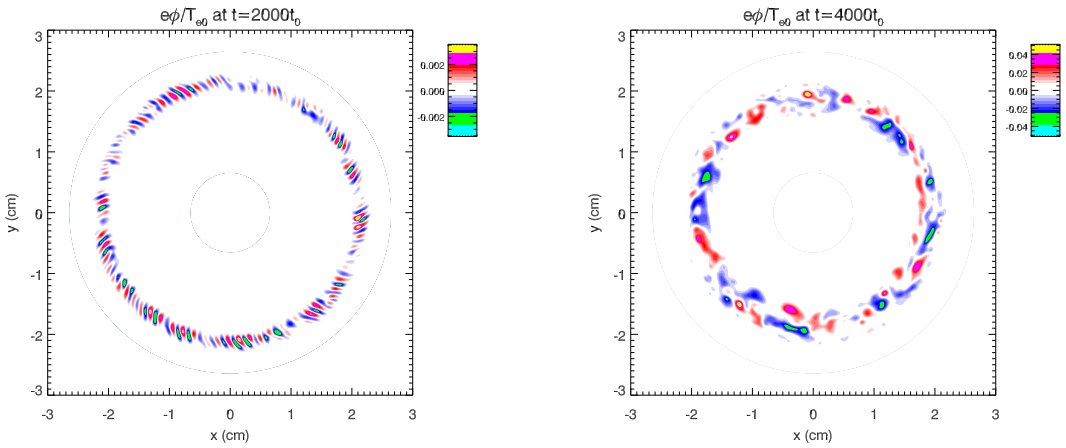


(a) (b)

Figure 5.7: Contours of the electric-potential fluctuation in the poloidal plane at a) linear stage $t = 2000t_0$, and b) nonlinear stage $t = 4000t_0$. In the linear stage, the fastest growing mode with $m \approx 70$, $n = 2$ ($m, n$ are the poloidal and the parallel mode number, respectively) dominates, while in the nonlinear stage, $m \approx 12$, $n = 1$ mode dominates.

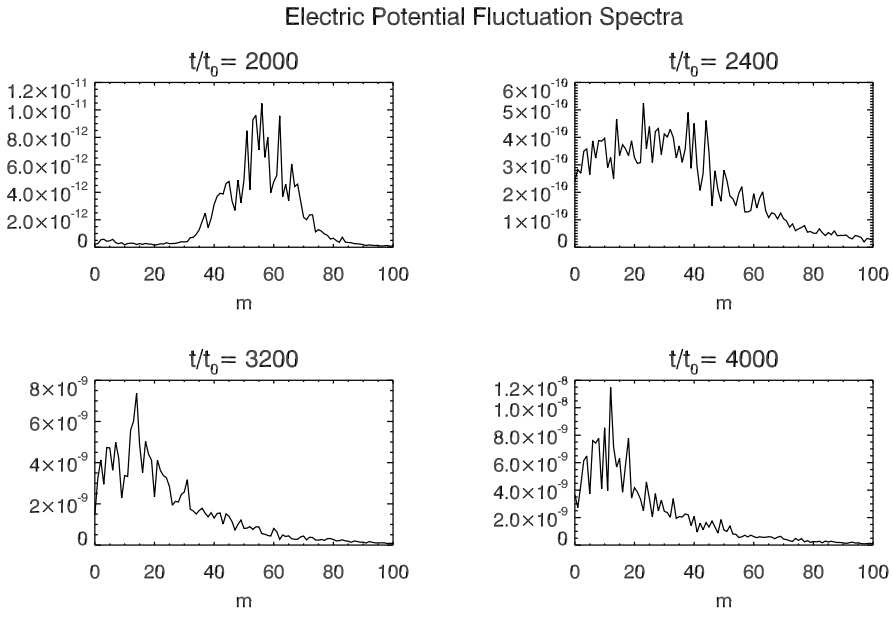


Figure 5.8: The poloidal power spectra of the electric potential fluctuation at $r = 1.88\,\mathrm{cm}$. The strong nonlinear coupling causes inverse cascading, and the peaking mode shifts from $m = 55$ down to $m = 12$.

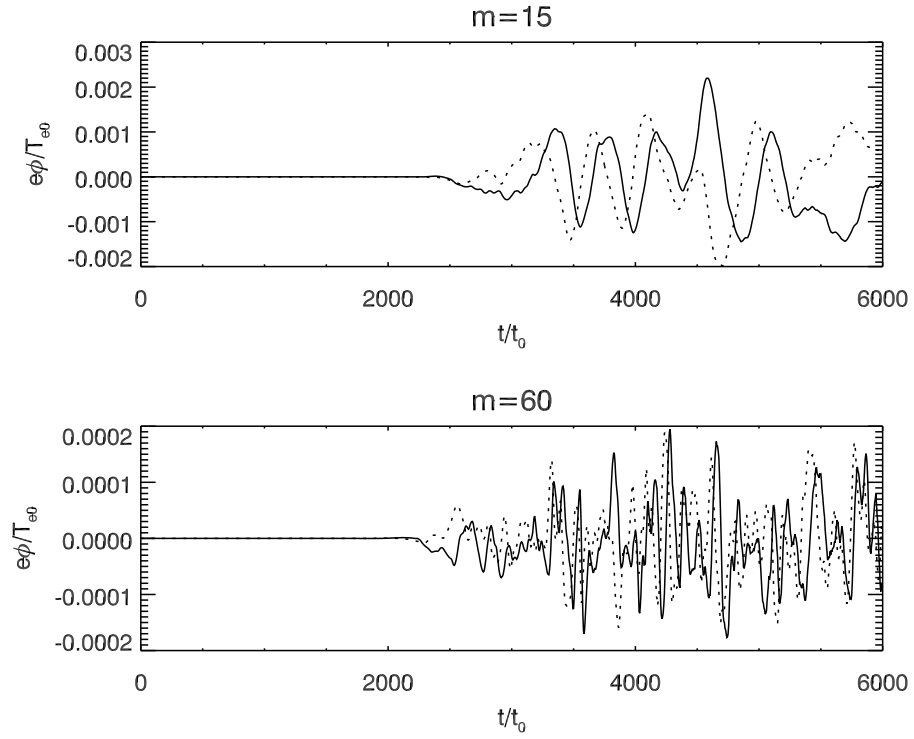


Figure 5.9: The time history of the electric potential of $m = 15$ mode and $m = 60$ mode. The solid line is the real part and the dotted line is the imaginary part. The frequency of $m = 15$ mode is about 0.24 MHz in the nonlinear stage.

experimental measurements ($0.3 - 0.5$ MHz).

#### 5.4.1.4 Radial profile of the electric potential fluctuations

The radial profile of root-mean-square values of the potential fluctuations $\phi_{\rm rms}(r)$ at different stages ($t = 2000t_0, 3000t_0, 4000t_0$) are shown in Fig. 5.10. The fluctuation of $e\phi/T_{e0}$ can go as high as 2%, and the peak of the fluctuation moves radially inward. This value is lower than that of experimen-

tal results which yield $e\phi/T_e \sim 5\%$. There are also small outward extending vortex structures or "fingers" in this nonlinear state. The inward and outward extensions may be caused by the density fluctuation. In this work we used the $\delta f$ algorithm with a fixed background temperature profile while letting the density fluctuation evolve freely. Consequently, in the nonlinear stage the density profile is no longer flat but has gradients away from the maximum temperature gradient. These trigger $\eta_e$-modes causing fluctuations to spread inward and outward.

#### 5.4.1.5 Heat flux

The evolution of the radial profile of electron energy flux, given by the correlation function of $\langle v_r \delta T_e \rangle$, is shown in Fig. 5.11. The nonlinear thermal flux extends over a broad radial region. The electron thermal conductivity can be estimated by

$$\chi_e = -q_e/n_e \nabla T_e. \tag{5.22}$$

At $t = 4000t_0$ and $r = 1.9\,\mathrm{cm}$, $\chi_e/D_{gB} \approx 0.43$, where $D_{gB} = \frac{\rho_e}{a}\frac{cT_e}{eB}$.

### 5.4.2 Parametric Variations of Measured Signal and those from Simulations

#### 5.4.2.1 Variation of fluctuations with the temperature gradient

In order to study the dependence of the electron heat flux on the temperature gradient, we compare three cases with the maximum $L_{T_e} = 0.33\,\mathrm{cm}$, $L_{T_e} = 0.45\,\mathrm{cm}$, and $L_{T_e} = 0.66\,\mathrm{cm}$. The profiles are shown in Fig. 5.12(a), and the comparison of the maximum potential fluctuation, the maximum electron

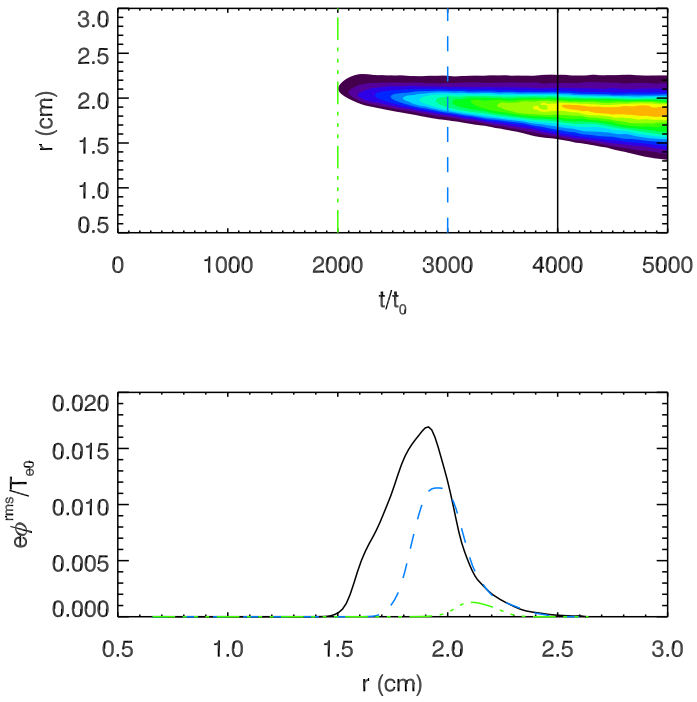


Figure 5.10: The evolution of the radial profile of the electric potential fluctuation averaged over an $r =$ constant surface, with the green curve corresponding to $t = 2000t_0$, the blue curve to $t = 3000t_0$, and the black curve to $t = 4000t_0$. The background electron temperature profile is fixed with the maximum gradient at $r = 1.8\,\mathrm{cm}$ and maximum $1/L_{Te}$ at $r = 2.1\,\mathrm{cm}$. Due to nonlinear effects, the peak of the fluctuation profile moves inward in time.

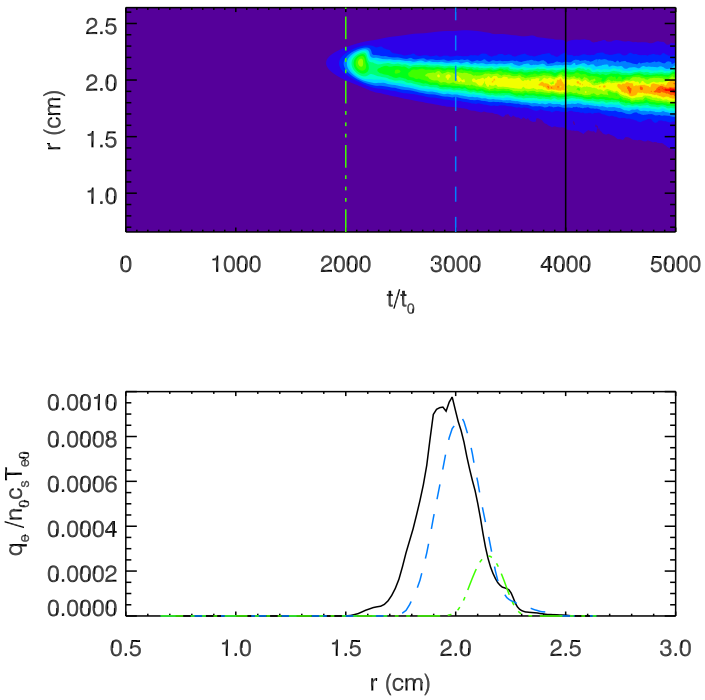


Figure 5.11: The evolution of the radial profile of the electron energy flux, with the green curve corresponding to $t = 2000t_0$, the blue curve to $t = 3000t_0$, and the black curve to $t = 4000t_0$.

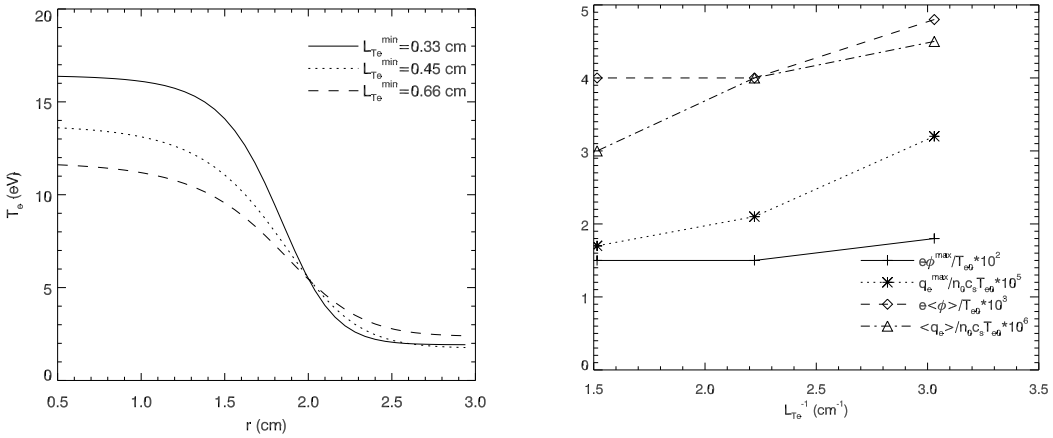


(a) (b)

Figure 5.12: (a) Various background electron temperature profiles for simulations, with the minimum $L_{T_e} = 0.33\,\mathrm{cm}, 0.45\,\mathrm{cm}$, and $0.66\,\mathrm{cm}$. (b) Comparison of the maximum potential fluctuation, the maximum electron heat flux, the averaged potential fluctuation, and the averaged electron heat flux between these simulations.

heat flux, the averaged potential fluctuation, and the averaged electron heat flux are shown in Fig. 5.12(b). The turbulence amplitude changes slower than the thermal flux, which indicates the turbulent transport may rely more on the correlation length and the temperature-fluctuation-to-potential phase than the turbulence intensity.

#### 5.4.2.2 Variation of the fluctuations with parallel wavenumber or axial Length

We also study the dependence of ETG modes on the parallel wavenumber by changing the major radius (or equivalently the machine length) from $R_0 = 300\,\mathrm{cm}$ to $R_0 = 100\,\mathrm{cm}$. The case with $R_0 = 100\,\mathrm{cm}$ shows very similar

features as $R_0 = 300\,\mathrm{cm}$ except that in the linear stage the fastest growing mode has $n = 1$ rather than $n = 2$ and the final quasi-steady-state is dominated by the $m = 15$ mode (cf. $m = 12$ in Fig. 5.7).

### 5.4.3 Nonlinear Saturation of ETG modes

As shown in the previous section, the inverse cascading of ETG energy from high-$m$ mode to low-$m$ mode indicates strong nonlinear coupling. The nonlinear theory for the saturation of toroidal ETG/ITG modes can be found in [33, 38]. A nonlinear saturation mechanism for slab ITG can be found in [55, 62]. In order to study the power spectrum, a higher spatial resolution simulation with $200 \times 1000 \times 32$ grid and $t_0 = 0.005 \times c_{s,e}/R_0$ is carried out. The log-log plot of the nonlinear power spectrum of the electric potential $\phi$ fluctuations is shown in Fig. 5.13 where a power law decay with $|\phi_m|^2$ proportional to $m^{-p}$, with $p = 1$ for $10 < m < 100$, and $p = 3$ for $m > 100$ is seen. This double-power-law spectrum agrees with the prediction of renormalization theory in Horton Jr et al. [38], which involved a three-wave interaction and non-resonant mode coupling under the quasi-normal approximation for the fourth order correlation function. The argument is based on the fact that the energy $\langle v_E^2 \rangle$ should be finite, which leads to a decay rate of $I(k)$ faster than $k^{-3}$ for high $k$ modes. The turning point in present work ($m \sim 100$) is, however, higher than that in Ref [38] ($m \sim 60$) due to the absence of toroidal effects.

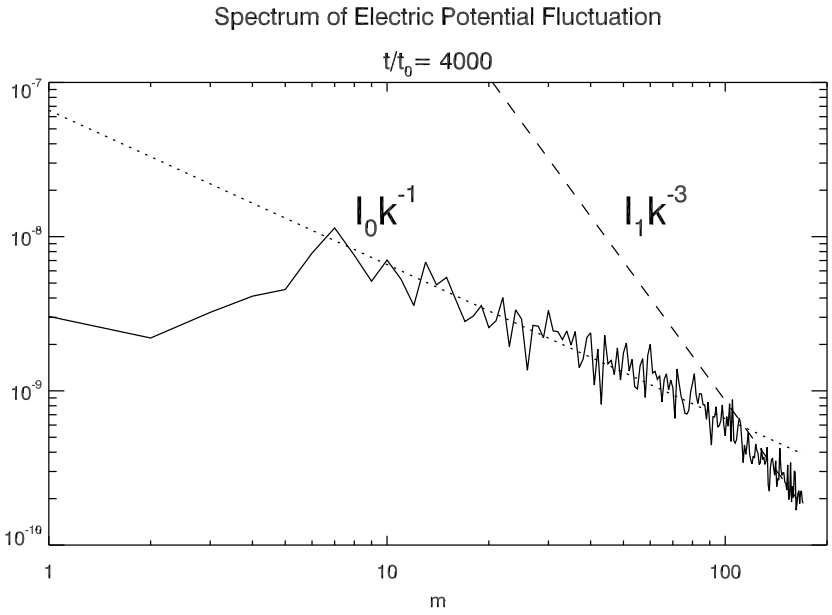


Figure 5.13: The power spectrum of electric potential fluctuation in the nonlinear stage. Shown is a power-law decay with the intensity proportional to $k^{-1}$ for $10 < m < 100$ modes, and $k^{-3}$ for $m > 100$ modes.

## 5.5 A Hamiltonian Model for ETG

In this section, we will present a Hamiltonian model for two-dimensional ETG. First a brief review of finite and infinite dimensional Hamiltonian systems is given and then we construct an infinite-dimensional Hamiltonian ETG model.

### 5.5.1 Finite-dimensional Hamiltonian System

We have learned in classical mechanics that a finite-dimensional Hamiltonian system can be written in the canonical form

$$\dot{Z} = J\nabla H = [Z, H] \tag{5.23}$$

where the Poisson bracket is defined with the operator $J$ as

$$[f, g] = \frac{\partial f}{\partial z^i} J^{ij} \frac{\partial g}{\partial z^j}. \tag{5.24}$$

For example, an N-dimensional system with $Z = (q^1, q^2, \ldots, q^N, p^1, p^2, \ldots, p^N)$ and

$$J = \begin{bmatrix} \mathbf{0}_N & \mathbf{I}_N \\ -\mathbf{I}_N & \mathbf{0}_N \end{bmatrix} \tag{5.25}$$

is described by Hamiltonian equations:

$$\dot{q}^i = \frac{\partial H}{\partial p^i} \tag{5.26}$$

$$\dot{p}^i = -\frac{\partial H}{\partial q^i}. \tag{5.27}$$

It turns out that because $\partial^2 f/\partial z^i \partial z^j = \partial^2 f/\partial z^j \partial z^i$ and operator $J$ is anti-symmetric, the Jacobi identity

$$[f, [g, h]] + [g, [h, f]] + [h, [f, g]] = 0 \tag{5.28}$$

is satisfied.

### 5.5.2 Hamiltonian for Infinite-Dimensional System

#### 5.5.2.1 Functional Derivatives

In order to extend finite-dimensional Hamiltonian to infinite dimensional, functionals (or integrals) and their derivatives need to be introduced since the Hamiltonian (or energy) of the system is usually the integral of energy density over the whole domain. A functional $F$ maps a function $f(x)$ to a value, e.g. in $R$. And its first functional derivative $\delta F/\delta f$ is defined by

$$\frac{d}{d\epsilon}F\left[f+\epsilon\delta f\right]\Big|_{\epsilon=0} = \left\langle \frac{\delta F}{\delta f}\middle| \delta f \right\rangle \equiv \int \frac{\delta F}{\delta f}\delta f dx; \tag{5.29}$$

therefore

$$\frac{\delta F}{\delta f} = \frac{\partial \mathcal{F}}{\partial f} - \frac{d}{dx}\frac{\partial \mathcal{F}}{\partial f_x} + \frac{d^2}{dx^2}\frac{\partial \mathcal{F}}{\partial f_{xx}} - \cdots \tag{5.30}$$

if $F = \int \mathcal{F}(f, f_x, f_{xx}, \dots)dx$.

#### 5.5.2.2 Generalized Hamiltonian Field Theory

Following [54], we define Hamiltonian systems in more general way. A system of equations

$$\frac{\partial u^k(t,\mathbf{x})}{\partial t} = F^k(\mathbf{u},\mathbf{x}),\ k = 1, 2, \dots, N \tag{5.31}$$

is Hamiltonian if it can be cast into the form

$$\frac{\partial u^k}{\partial t} = \left\{u^k, H\right\}, \tag{5.32}$$

where the bracket makes the functional space a Lie Algebra, namely, it is a vector space equipped with a bilinear bracket

$$\{F, G\} = \left\langle \frac{\delta F}{\delta u^i} \middle| O^{ij} \frac{\delta G}{\delta u^j} \right\rangle \tag{5.33}$$

that satisfies Jacobi identity (cf Eq. (5.28))

$$\{F, \{G, H\}\} + \{G, \{H, F\}\} + \{H, \{F, G\}\} = 0 \tag{5.34}$$

#### 5.5.2.3 Jacobi Identity

It can be proved [54] that if $O^{ij}$ is independent of $\mathbf{u}$ and anti-self-adjoint, then the above Jacobi identity is satisfied.

Then the next question is given $F^k$ as in Eq. (5.31), how to obtain the Hamiltonian $H$ and the operator $O$. A systematic way of doing this, based on Hamilton's principle for many fluid and plasma models can be found in [53].

### 5.5.3 Electrostatic ETG Turbulence

Now we will "Hamiltonianize" the electrostatic ETG model.

#### 5.5.3.1 Model Equations

In this model, the plasma is described by a distribution function $f(\mathbf{x}, \mathbf{v}, t)$ and we consider only the electrostatic field (the magnetic field still exists but is treated as constant, so the full Maxwell equations are reduced to Poisson's equation only). Poisson's equation reads

$$\Delta\phi = 4\pi e(\delta n_e - \delta n_i) \tag{5.35}$$

where $\phi = \phi(\mathbf{x}, t)$ is the electric potential and $\delta n_e$, $\delta n_i$ are density fluctuations for electrons and ions, respectively. We assume the ion response to electric field is adiabatic, i. e.

$$\delta n_i \approx -\frac{n_i e\phi}{T_i}. \tag{5.36}$$

And the electron density fluctuation can be calculated from the distribution function

$$\delta n_e = \int \delta f \, d\mathbf{v}. \tag{5.37}$$

In order to further simplify the model, we make guiding-center assumptions:

1. The electrons gyrate very fast about a strong $B$ field, and the major motion across the field is $\mathbf{E} \times \mathbf{B}$ drift

2. The electron gyroradius is much smaller than the spatial scale of $\mathbf{E}$-field variation

Therefore for the time scale of interest (much slower than electron gyrofrequency), the motion of electrons can be approximated by the guiding center motion. The Vlasov equation for electrons is then written as

$$\frac{\partial f}{\partial t} + v_z \frac{\partial f}{\partial z} + v_E \cdot \frac{\partial f}{\partial x_\perp} + \frac{e}{m_e} \frac{\partial \phi}{\partial z} \frac{\partial f}{\partial v_z} = 0, \tag{5.38}$$

where $x_\perp = (x, y)$, $v_E = \hat{z} \times \frac{c\nabla\phi}{B}$ and $f = f(x, y, z, v_z, t)$ is the distribution function for guiding centers (not electrons). Note, here we assume the distribution function is independent of $v_\perp$, i.e. the velocity distribution perpendicular

to $B$ field is always Maxwellian. And Poisson's equation becomes

$$\Delta\phi = 4\pi e\left(\int \delta f\, dv_z + \frac{n_i e\phi}{T_i}\right). \tag{5.39}$$

Equation (5.38) can be written as

$$\frac{\partial f}{\partial t} - [f, \mathcal{E}] = 0 \tag{5.40}$$

with $\mathcal{E} = -e\phi + m_e v_z^2/2$ and Poisson bracket

$$[f, g] = \frac{c}{eB}\left(\frac{\partial f}{\partial x}\frac{\partial g}{\partial y} - \frac{\partial f}{\partial y}\frac{\partial g}{\partial x}\right) + \frac{1}{m_e}\left(\frac{\partial f}{\partial z}\frac{\partial g}{\partial v_z} - \frac{\partial f}{\partial v_z}\frac{\partial g}{\partial z}\right). \tag{5.41}$$

Defining a new operator

$$\Delta^* \equiv \nabla^2 - \frac{1}{\lambda_{De}^2}\frac{T_e}{T_i} \tag{5.42}$$

where $\lambda_{De}$ is the Debye length, Eq. (5.39) becomes

$$\Delta^*\phi = 4\pi e\int \delta f\, dv_z. \tag{5.43}$$

#### 5.5.3.2 Noncanonical Poisson Bracket

We can find an noncanonical Poisson bracket

$$\{F, G\} = \int \left[\frac{\delta F}{\delta f}, \frac{\delta G}{\delta f}\right] dxdydv_z dz \tag{5.44}$$

and Hamiltonian

$$H[f] = \frac{1}{2}\int (f m_e v_z^2 - e\phi\Delta^*\phi) dxdydzdv_z \tag{5.45}$$

such that

$$\frac{\partial f}{\partial t} = \{f, H\} = -[f, \mathcal{E}] \tag{5.46}$$

### 5.5.4 Conservation Laws

Obviously, the Hamiltonian (energy) $H$ is conserved. The system also has Casimir invariants

$$C[f] = \int dxdydzdv_z \mathcal{C}(f) \tag{5.47}$$

where $\mathcal{C}(f)$ is an arbitrary function of $f$; e.g.,

$$M = \int f\, dxdydzdv_z. \tag{5.48}$$

There are also other conserved quantities like momentum and angular momentum

$$\mathbf{P} = \hat{\mathbf{e}}_z \int v_z f\, dxdydzdv_z, \tag{5.49}$$

$$\mathbf{L} = \int (yv_z\hat{\mathbf{e}}_x - xv_z\hat{\mathbf{e}}_y) f\, dxdydzdv_z \tag{5.50}$$

## 5.6 Conclusions

The ETG mode is a universal mechanism for turbulent electron thermal transport across various magnetic confinement geometries. The variable electron temperature gradient driven high frequency drift wave turbulence produced in the CLM experiment is well interpreted by the GTC gyrokinetic code. In the terminology of simulation modeling, the agreement allows one to state the GTC code is verified by the data from the CLM experiment. The amplitude of the saturation level is set principally by the nonlinear cascade from the fastest linearly growing modes with $m \sim 70$, as given by the linear

kinetic dispersion relation, to the nonlinear spectrum that peaked at $m \sim 15$. These results can be explained by the early nonlinear model of the inverse cascade given in Horton et al. [33]. Thus, the verification of the strong inverse cascade in the CLM data using the GTC gyrokinetic equation simulations is an important confirmation of early turbulence theory models for drift wave systems.

Future work is planned to extend the simulations to low-$m$ modes ($m < 10$) where the plasma response functions are those of the usual ion drift waves and acoustic modes. This involves coupling the simulations to the conventional ion scale simulations and theories and it may further lower the rms amplitude of the high-$m$ modes in the spectrum.

# Chapter 6

# Summary

In this thesis, particle and thermal transport in a magnetized plasmas driven by drift wave turbulence were studied. Background material of the research and simple pictures of drift waves were introduced in Chapter 1.

In Chapter 2, physical models of various type of the drift waves were derived and summarized. Equations for density-gradient driven drift waves, ion temperature gradient (ITG) modes, trapped electron modes (TEM) and electron temperature gradient (ETG) modes were given.

In Chapter 3, passive particle transport by given electric and magnetic fields in the Gamma-10 tandem mirror machine were presented. The total given field consists of a background field produced externally and a fluctuating part driven by drift wave instabilities. By assuming an infinite coherent spectrum of drift waves, the motion of charge particles was reduced to maps with a general momentum and general coordinate. It was observed that particle transport was reduced when the background electric potential is changed from a monotonic profile to one with reversed $E_r$.

In Chapter 4, impurity particle transport in Alcator C-Mod was studied by a quasilinear theory. Eigensystems of various unstable modes in the C-

Mod plasma was solved and quasilinear particle fluxes were calculated with models for the fluctuation level. Transport coefficients, the diffusivity $D$ and the pinch velocity $V$ were derived. With CXRS, boron density profiles were measured in C-Mod for confinement modes, including the H-mode, ITB and the I-mode. The ratio of $V/D$ was extracted from the profiles. $V/D$ driven by the ordinary drift wave and the ITG mode were calculated and compared to the experiments.

In Chapter 5, the electron thermal transport by the ETG mode was investigated. The ETG mode was produced and verified in the Columbia Linear Machine. Large scale gyrokinetic simulations using the GTC code were seen to reproduce results from the experiment. The early growth stage of the simulations was verified by comparison with linear theory, and nonlinear results showed good agreement in the dominant mode number, the wave frequency, and the radial structure. Some nonlinear processes, such as the inverse cascading of the poloidal wave spectrum and the radial spreading of the fluctuation profile were also analyzed using the code.

# Appendices

# Appendix A

# Plasma Dispersion Function

## A.1 Plasma Dispersion Function

In plasma physics, to study wave particle interactions, we often encounter the integral over Maxwellian velocity distribution with a singular resonant point. In the case of 1D Landau damping, the dispersion relation is given by

$$D(\omega, k) = 1 + \frac{e^2}{m_e k^2 \epsilon_0} \int_{-\infty}^{\infty} \frac{\partial f_0/\partial v}{\omega/k - v} dv \tag{A.1}$$

where

$$f_0(v) = n_0 \sqrt{\frac{m_e}{2\pi T_e}} \exp\left(-\frac{m_e v^2}{2T_e}\right) \tag{A.2}$$

$$\frac{\partial f_0}{\partial v} = -\frac{n_0}{\sqrt{\pi}} \frac{2v}{v_{th}^3} \exp\left(-\frac{v^2}{v_{th}^2}\right) \tag{A.3}$$

and $v_{th} = \sqrt{2T_e/m_e}$. The integral can be evaluated as

$$\begin{aligned}
\int_{-\infty}^{\infty} \frac{\partial f_0/\partial v}{\omega/k - v} dv &= -\frac{n_0}{\sqrt{\pi}} \frac{2}{v_{th}^3} \int_{-\infty}^{\infty} \frac{v \exp(-v^2/v_{th}^2)}{\omega/k - v} dv & \text{(A.4)} \\
&= \frac{2n_0}{\sqrt{\pi} v_{th}^3} \int_{-\infty}^{\infty} \left(1 + \frac{\omega/k}{v - \omega/k}\right) e^{-v^2/v_{th}^2} dv & \text{(A.5)} \\
&= \frac{2n_0}{\sqrt{\pi} v_{th}^3} \sqrt{\pi} v_{th} \left(1 + \frac{\omega}{k v_{th} \sqrt{\pi}} \int_{-\infty}^{\infty} \frac{e^{-t^2}}{t - \omega/k v_{th}} dt\right) & \text{(A.6)} \\
&= \frac{2n_0}{v_{th}^2} \left[1 + \zeta Z(\zeta)\right], & \text{(A.7)}
\end{aligned}$$

where $t = v/v_{th}$, $\zeta = \omega/kv_{th}$ and $Z(\zeta)$ is the plasma dispersion function or Z function

$$Z(\zeta) = \pi^{-1/2} \int_{-\infty}^{\infty} \frac{\exp(-t^2)}{t - \zeta} dt \tag{A.8}$$

There are two limits of the $Z$ function useful for analytic analysis,[20] i.e. the power series ($|\zeta| \ll 1$)

$$Z(\zeta) = i\sqrt{\pi} e^{-\zeta^2} - 2\zeta(1 - 2\zeta^2/3 + 4\zeta^4/15 - 8\zeta^6/105 + \dots) \tag{A.9}$$

and the asymptotic series ($|\zeta| \gg 1$)

$$Z(\zeta) = i\sqrt{\pi}\sigma e^{-\zeta^2} - \zeta^{-1}(1 + 1/2\zeta^2 + 3/4\zeta^4 + 15/8\zeta^6 + \dots) \tag{A.10}$$

where

$$\sigma = \begin{cases} 0 & y > 0 \\ 1 & y = 0 \\ 2 & y < 0 \end{cases} . \tag{A.11}$$

## A.2 Computational Method

To evaluate the plasma dispersion function numerically, there are two methods.

### A.2.1 Direct Method

According to Landau's prescription, the integral path needs to be deformed properly to make $Z(\zeta)$ analytic when $\zeta$ moves across the real axis. This requires that the singular point of the $v$-integral be always on the same side of integration path (say left). For $\mathfrak{Im}(\zeta) > 0$, there is no problem. However, for

$\mathfrak{Im}(\zeta) = 0$, we need to deformed the path a little bit to include a semi-circle under the singular point. The integral over this semi-circle gives $i\pi$ times the residue. Similarly, for $\mathfrak{Im}(\zeta) < 0$, the integral over an extra circle around the singular point is needed and gives $2i\pi$ times the residue. Therefore,

$$Z(\zeta) = \pi^{-1/2} \int_{-\infty}^{\infty} \frac{\exp(-t^2)}{t-\zeta} dt \tag{A.12}$$

$$= \pi^{-1/2} \left( \Pr \int_{-\infty}^{\infty} \frac{\exp(-t^2)}{t-\zeta} dt + I_{\text{ex}} \right) \tag{A.13}$$

$$I_{\text{ex}} = \begin{cases} 0 & \mathfrak{Im}(\zeta) > 0 \\ i\pi \exp(-\zeta^2) & \mathfrak{Im}(\zeta) = 0 \\ 2i\pi \exp(-\zeta^2) & \mathfrak{Im}(\zeta) < 0 \end{cases} \tag{A.14}$$

If $\zeta = x + iy$, then

$$\Pr \int_{-\infty}^{\infty} \frac{\exp(-t^2)}{t-\zeta} dt = \Pr \int_{-\infty}^{\infty} \frac{(t-x)e^{-t^2}}{(t-x)^2+y^2} dt + i \Pr \int_{-\infty}^{\infty} \frac{y e^{-t^2}}{(t-x)^2+y^2} dt. \tag{A.15}$$

This method will encounter difficulty when evaluating the principal-value integrals for $y = 0$.

### A.2.2 Integral Transform

The plasma dispersion function can be transformed into a form that's valid for any $\zeta$ [20]. Taking the derivative with respect to $\zeta$, and integrating by parts over $t$, we have

$$Z'(\zeta) = -2[\zeta Z(\zeta) + 1], \tag{A.16}$$

which is a first-order linear ODE that can be solved analytically. Multiplying the equation by an unknown function $\alpha(\zeta)$ gives

$$\alpha \frac{dZ}{d\zeta} + 2\alpha\zeta Z + 2\alpha = 0, \tag{A.17}$$

which can then be transformed to

$$\frac{d(\alpha Z)}{d\zeta} = -2\alpha \tag{A.18}$$

if $\frac{d\alpha}{d\zeta} = 2\alpha\zeta$. Finally, we solve for $Z$

$$Z(\zeta) = -\frac{\int 2\alpha d\zeta}{\alpha} = -\frac{\int 2e^{\zeta^2} d\zeta}{e^{\zeta^2}} = -\left[e^{-\zeta^2} \int_0^{\zeta} 2e^{\zeta^2} d\zeta\right] + Z(0). \tag{A.19}$$

We want the analytic continuation of $Z(\zeta)$ from the upper complex plane across the real axis to the lower plane, so

$$Z(0) = \pi^{-1/2}(\mathrm{Pr} \int_{-\infty}^{\infty} \frac{e^{-t^2}}{t} dt + i\pi) = i\sqrt{\pi}; \tag{A.20}$$

therefore, let $t = i\zeta$, and notice

$$\int_{-\infty}^{0} e^{-t^2} dt = \sqrt{\pi}/2. \tag{A.21}$$

Thus, we obtain a second form of plasma dispersion function

$$Z(\zeta) = 2ie^{-\zeta^2} \int_{-\infty}^{i\zeta} dt\, e^{-t^2}. \tag{A.22}$$

If $\zeta = x + iy$, then $\zeta^2 = (x^2 - y^2) + 2ixy$, and

$$Z(x + iy) = 2ie^{-x^2+y^2} e^{-2ixy} \int_{-\infty}^{-y+ix} dt\, e^{-t^2} \tag{A.23}$$

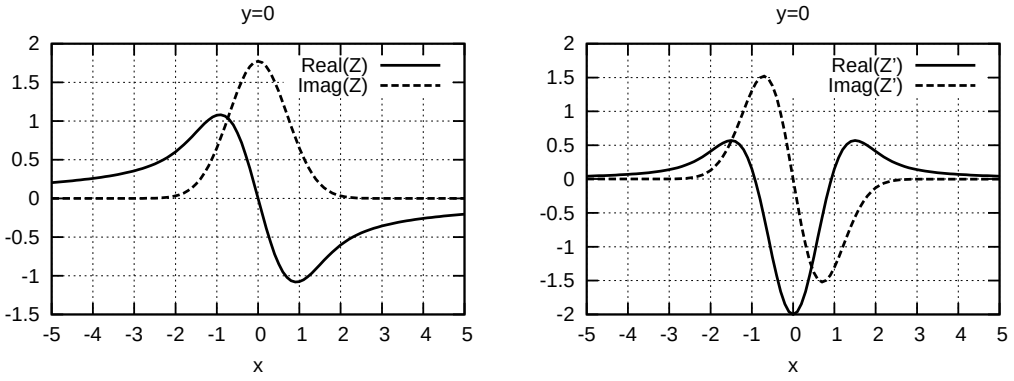


Figure A.1: Plasma dispersion function $Z(\zeta)$ and its derivative with real argument $\zeta = x$.

The integral is carried out as

$$\int_{-\infty}^{-y+ix} dt\, e^{-t^2} \tag{A.24}$$

$$= \int_{-\infty}^{-y} dt\, e^{-t^2} + \int_{-y}^{-y+ix} dt\, e^{-t^2} \tag{A.25}$$

$$= \int_{y}^{\infty} dt'\, e^{-t'^2} + i\int_{0}^{x} dt'\, e^{-(it'-y)^2} \tag{A.26}$$

($t' = -t$ for fist part, and $t' = -i(t+y)$ for the second part)

$$= \int_{y}^{\infty} dt\, e^{-t^2} + ie^{-y^2}\int_{0}^{x} dt\, e^{t^2}[\cos(2yt) + i\sin(2yt)] \tag{A.27}$$

$$= \frac{\sqrt{\pi}}{2}[1 - \mathrm{erf}(y)] + e^{-y^2}\int_{0}^{x} dt\, e^{t^2}[i\cos(2yt) - \sin(2yt)] \tag{A.28}$$

By rearranging terms, we get

$$Z(x+iy) = 2ie^{-2ixy}\left\{\frac{\sqrt{\pi}}{2}[1 - \mathrm{erf}(y)]e^{-x^2+y^2} + \int_{0}^{x} dt\, e^{t^2-x^2}[i\cos(2yt) - \sin(2yt)]\right\}. \tag{A.29}$$

suitable for numerical evaluation.

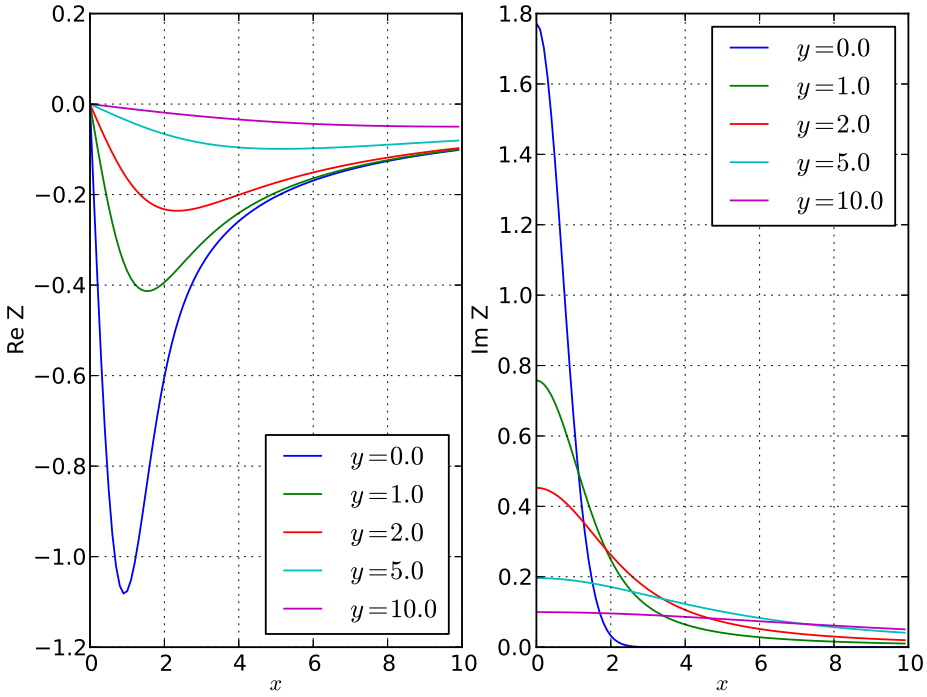


Figure A.2: The general behavior of the plasma dispersion function $Z(x+iy)$.

The following is a table of the Z-function with real argument. It has been tested against the analytic formula.

| x+iy | Z | Z' |
|---|---|---|
| 0.0+0.0i | +0.000000e+00+1.772454e+00i | -2.000000e+00+0.000000e+00i |
| 0.5+0.0i | -8.488728e-01+1.380388e+00i | -1.151127e+00-1.380388e+00i |
| 1.0+0.0i | -1.076159e+00+6.520493e-01i | +1.523180e-01-1.304099e+00i |
| 1.5+0.0i | -8.564981e-01+1.868153e-01i | +5.694944e-01-5.604458e-01i |
| 2.0+0.0i | -6.026808e-01+3.246362e-02i | +4.107231e-01-1.298545e-01i |
| 2.5+0.0i | -4.461674e-01+3.421641e-03i | +2.308372e-01-1.710820e-02i |
| 3.0+0.0i | -3.565421e-01+2.187382e-04i | +1.392524e-01-1.312429e-03i |
| 3.5+0.0i | -2.992432e-01+8.481400e-06i | +9.470230e-02-5.936980e-05i |
| 4.0+0.0i | -2.586960e-01+1.994634e-07i | +6.956802e-02-1.595707e-06i |
| 4.5+0.0i | -2.281772e-01+2.845193e-09i | +5.359498e-02-2.560673e-08i |
| 5.0+0.0i | -2.042681e-01+2.461574e-11i | +4.268149e-02-2.461574e-10i |
| 5.5+0.0i | -1.849865e-01+1.291715e-13i | +3.485111e-02-1.420887e-12i |
| 6.0+0.0i | -1.690854e-01+4.111247e-16i | +2.902454e-02-4.933497e-15i |
| 6.5+0.0i | -1.557356e-01+7.936574e-19i | +2.456329e-02-1.031755e-17i |
| 7.0+0.0i | -1.443619e-01+9.292773e-22i | +2.106729e-02-1.300988e-20i |
| 7.5+0.0i | -1.345516e-01+6.599489e-25i | +1.827435e-02-9.899234e-24i |
| 8.0+0.0i | -1.260004e-01+2.842681e-28i | +1.600636e-02-4.548289e-27i |
| 8.5+0.0i | -1.184787e-01+7.426747e-32i | +1.413864e-02-1.262547e-30i |
| 9.0+0.0i | -1.118101e-01+1.176852e-35i | +1.258168e-02-2.118334e-34i |

```
9.5+0.0i -1.058563e-01+1.131092e-39i +1.126980e-02-2.149075e-38i
```

# Appendix B

# Useful Expressions

$$\mathbf{v}_E \cdot \nabla_\perp f = \frac{c}{B}\left[\phi, f\right]_{\mathrm{PB}}, \tag{B.1}$$

where $\mathbf{v}_E = \frac{c\mathbf{b}\times\nabla_\perp\phi}{B}$.

$$\nabla_\perp \cdot \mathbf{v}_{pi} = \frac{c}{\omega_{ci}B_0}\left(-\frac{\partial}{\partial t}\nabla_\perp^2\phi - \frac{c}{B_0}\left[\phi, \nabla_\perp^2\phi\right]_{\mathrm{PB}}\right), \tag{B.2}$$

where $\omega_{ci} = eB_0/m_i c$, and $\mathbf{v}_{pi} = \frac{c^2 m_i}{q_i B^2}\frac{d\mathbf{E}}{dt}$.

$$\nabla_\perp \cdot \mathbf{v}_{pe} = \frac{c}{\omega_{ce}B_0}\left(\frac{\partial}{\partial t}\nabla_\perp^2\phi + \frac{c}{B_0}\left[\phi, \nabla_\perp^2\phi\right]_{\mathrm{PB}}\right), \tag{B.3}$$

where $\omega_{ce} = eB_0/m_e c$.

$$\mathbf{v}_{*ne} = \frac{cT_e}{eB}\frac{1}{L_{ne}}, \tag{B.4}$$

$$\mathbf{v}_{*Te} = \frac{cT_e}{eB}\frac{1}{L_{Te}}, \tag{B.5}$$

$$\frac{cT_e}{eB} = \rho_s c_s = \rho_e v_{te} = L_{ne}v_{*ne} = L_{Te}v_{*Te}, \tag{B.6}$$

where $c_s = \sqrt{T_e/m_i}$, $\rho_s = c_s/\omega_{ci}$, $v_{te} = \sqrt{T_e/m_e}$, $\rho_e = v_{te}/\omega_{ce}$.

Poisson's equation

$$\nabla^2\phi = 4\pi e(-Z\delta n_i + \delta n_e) \tag{B.7}$$

is equivalent to

$$\nabla^2 \left( \frac{e\phi}{T_e} \right) = \frac{\omega_{pe}^2}{\omega_{ce}^2} (-Z \frac{\delta n_i}{n_e} + \frac{\delta n_e}{n_e}) \tag{B.8}$$

The thermal balance equation for species $a$ is [29]:

$$\frac{3}{2} n_a \frac{dT_a}{dt} + p \nabla \cdot \mathbf{V}_a = -\nabla \cdot \mathbf{q}_a - \boldsymbol{\pi}_a : \nabla \mathbf{V}_a + Q_a, \tag{B.9}$$

where

$$p \equiv nm \left\langle v'^2 \right\rangle_f /3 = nT, \tag{B.10}$$

$$\pi_{jk} \equiv nm \left\langle v'_j v'_k \right\rangle_f - p\delta_{jk}, \tag{B.11}$$

$$\mathbf{q} \equiv n \left\langle \frac{mv'^2}{2} \mathbf{v}' \right\rangle_f, \tag{B.12}$$

$$Q \equiv \int \frac{mv'^2}{2} C(f) d^3 v. \tag{B.13}$$

# Appendix C

# Index of Notation

## C.1 General notation

Italic character like $f$ is a scalar.

Boldface character like $\mathbf{v}$ is a vector.

Character with left-right arrow overhead like $\overleftrightarrow{\mathrm{T}}$ is a tensor.

Directional derivative

$$\frac{\partial f}{\partial \mathbf{x}} \equiv \frac{\partial f}{\partial x}\hat{\mathbf{e}}_x + \frac{\partial f}{\partial y}\hat{\mathbf{e}}_y + \frac{\partial f}{\partial z}\hat{\mathbf{e}}_z.$$

Vectors in both the numerator and the denominator is a tensor

$$\nabla \mathbf{v} \equiv \frac{\partial \mathbf{v}}{\partial \mathbf{x}}\ , \left(\frac{\partial \mathbf{v}}{\partial \mathbf{x}}\right)_{ij} \equiv \frac{\partial v_i}{\partial x_j}.$$

## C.2 Special notations

| | |
|---|---|
| $a$ | Minor radius |
| $A$ | Atomic mass number |
| $B$ | Magnetic field strength |
| $\mathbf{B}$ | Magnetic field vector |
| $c$ | Speed of light |
| $E$ | Electric field strength |
| $\mathbf{E}$ | Electric field vector |
| $e$ | Charge of electron |
| $\mathbf{k}$ | Wave number vector |
| $m$ | mass |
| $n$ | number density |
| $R$ | Major radius |
| $R_0$ | Major radius at the center of plasma |
| $t$ | time |
| $\mathbf{v}$ | Velocity vector |
| $\mathbf{v}_*$ | diamagnetic drift velocity (with density gradient only) |
| $\mathbf{v}_d$ | diamagnetic drift velocity |
| $\mathbf{v}_D$ | curvature drift velocity |
| $\mathbf{v}_E$ | $E \times B$ drift velocity |
| $\mathbf{v}_p$ | polarization drift velocity |
| $Z$ | Charge number |

# Bibliography

[1] C. Angioni and A. Peeters. Direction of Impurity Pinch and Auxiliary Heating in Tokamak Plasmas. *Physical Review Letters*, 96(9):1–4, March 2006. ISSN 0031-9007. doi: 10.1103/PhysRevLett.96.095003. URL `http://link.aps.org/doi/10.1103/PhysRevLett.96.095003`.

[2] C. Angioni, A.G. Peeters, G.V. Pereverzev, A. Bottino, J. Candy, R. Dux, E. Fable, T. Hein, and R.E. Waltz. Gyrokinetic simulations of impurity, He ash and $\alpha$ particle transport and consequences on ITER transport modelling. *Nuclear Fusion*, 49(5):055013, 2009. URL `http://stacks.iop.org/0029-5515/49/i=5/a=055013`.

[3] E. Asp, J.-H. Kim, W. Horton, L. Porte, S. Alberti, A. Karpushov, Y. Martin, O. Sauter, G. Turri, and The Tcv Team. Electron thermal transport analysis in Tokamak à Configuration Variable. *Physics of Plasmas*, 15(8):082317, August 2008. doi: 10.1063/1.2965828.

[4] R. Balescu. *Transport Processes in Plasmas: Classical transport*. Transport Processes in Plasmas. North-Holland, 1988. ISBN 9780444870919.

[5] R. Balescu. *Transport Processes in Plasmas: Neoclassical transport*. Transport Processes in Plasmas. North-Holland, 1988. ISBN 9780444870926.

[6] R. Balescu. *Aspects of Anomalous Transport in Plasmas*. Series in Plasma Physics. Taylor & Francis, 2005. ISBN 9780750310307.

[7] E. A. Belli and J. Candy. Kinetic calculation of neoclassical transport including self-consistent electron and impurity dynamics. *Plasma Physics and Controlled Fusion*, 50(9):095010, September 2008. doi: 10.1088/0741-3335/50/9/095010.

[8] John P. Boyd. *Chebyshev and Fourier Spectram Methods*. Dover, New York, 2 edition, 2001. URL `http://www-personal.umich.edu/\~jpboyd/BOOK\_Spectral2000.html`.

[9] A. J. Brizard and T. S. Hahm. Foundations of nonlinear gyrokinetic theory. *Reviews of Modern Physics*, 79(2):421–468, April 2007. ISSN 0034-6861. doi: 10.1103/RevModPhys.79.421. URL `http://link.aps.org/doi/10.1103/RevModPhys.79.421`.

[10] J. N. Brooks, J. P. Allain, R. P. Doerner, A. Hassanein, R. Nygren, T. D. Rognlien, and D. G. Whyte. Plasma-surface interaction issues of an all-metal ITER. *Nuclear Fusion*, 49(3):035007, 2009. URL `http://stacks.iop.org/0029-5515/49/i=3/a=035007`.

[11] T. Cho, J. Kohagura, T. Numakura, M. Hirata, H. Higaki, H. Hojo, M. Ichimura, K. Ishii, K. Islam, A. Itakura, I. Katanuma, R. Minami, Y. Nakashima, T. Saito, Y. Tatematsu, O. Watanabe, M. Yoshikawa, A. Kojima, Y. Miyake, Y. Miyata, K. Shimizu, Y. Tomii, M. Yoshida,

K. Sakamoto, T. Imai, V. Pastukhov, and S. Miyoshi. Observation and Control of Transverse Energy-Transport Barrier due to the Formation of an Energetic-Electron Layer with Sheared ExB Flow. *Physical Review Letters*, 97(5):1–4, July 2006. ISSN 0031-9007. doi: 10.1103/PhysRevLett.97.055001. URL http://link.aps.org/doi/10.1103/PhysRevLett.97.055001.

[12] T. Cho, V. P. Pastukhov, W. Horton, T. Numakura, M. Hirata, J. Kohagura, N. V. Chudin, and J. Pratt. Active control of internal transport barrier formation due to off-axis electron-cyclotron heating in GAMMA 10 experiments. *Physics of Plasmas*, 15(5):056120, May 2008. ISSN 1070664X. doi: 10.1063/1.2906262. URL http://link.aip.org/link/?PHPAEN/15/056120/1.

[13] Darío Correa-Restrepo and Dieter Pfirsch. New method of deriving local energy- and momentum-conserving Maxwell-collisionless drift-kinetic and gyrokinetic theories: conservation laws and their structures. *Journal of Plasma Physics*, 70(6):757–797, December 2004. ISSN 0022-3778. doi: 10.1017/S0022377804003034. URL http://www.journals.cambridge.org/abstract_S0022377804003034.

[14] Diego Del-Castillo-Negrete and P. J. Morrison. Chaotic transport by Rossby waves in shear flow. *Physics of Fluids A: Fluid Dynamics*, 5(4):948, 1993. ISSN 08998213. doi: 10.1063/1.858639. URL http://link.aip.org/link/PFADEB/v5/i4/p948/s1\&Agg=doi.

[15] W. Deng, Z. Lin, I. Holod, X. Wang, Y. Xiao, and W. Zhang. Gyrokinetic particle simulations of reversed shear Alfvén eigenmode excited by antenna and fast ions. *Physics of Plasmas*, 17(11):112504, November 2010. doi: 10.1063/1.3496057.

[16] K. J. Dietz and The JET Team. Effect of beryllium on plasma performance in jet. *Plasma Physics and Controlled Fusion*, 32(11):837, 1990. URL `http://stacks.iop.org/0741-3335/32/i=11/a=002`.

[17] B D Dudson, H R Wilson, M V Umansky, X Q Xu, and P B Snyder. BOUT ++ : a framework for parallel plasma fluid simulations. (November), 2008.

[18] C. L. Fiore, D. R. Ernst, Y. a. Podpaly, D. Mikkelsen, N. T. Howard, Jungpyo Lee, M. L. Reinke, J. E. Rice, J. W. Hughes, Y. Ma, W. L. Rowan, and I. Bespamyatnov. Production of internal transport barriers via self-generated mean flows in Alcator C-Mod. *Physics of Plasmas*, 19 (5):056113, 2012. ISSN 1070664X. doi: 10.1063/1.3694668. URL `http://link.aip.org/link/PHPAEN/v19/i5/p056113/s1\&Agg=doi`.

[19] Harald U. Frey. Localized aurora beyond the auroral oval. *Reviews of Geophysics*, 45(1):RG1003, March 2007. ISSN 8755-1209. doi: 10.1029/2005RG000174. URL `http://www.agu.org/pubs/crossref/2007/2005RG000174.shtml`.

[20] Burton D. Fried and Samuel D. Conte. *The Plasma Dispersion Function*. Academic Press, New York and London, 1961.

[21] X. R. Fu, W. Horton, W. L. Rowan, I. O. Bespamyantnov, S. Benkadda, C. L. Fiore, S. Futatani, and K. T. Liao. Turbulent impurity transport modeling for c-mod. submitted to Journal of Plasma Physics.

[22] X. R. Fu, W. Horton, Y. Xiao, Z. Lin, A. K. Sen, and V. Sokolov. Validation of electron temperature gradient turbulence in the Columbia Linear Machine. *Physics of Plasmas*, 19(3):032303, March 2012. doi: 10.1063/1.3686148.

[23] S. Futatani, W. Horton, S. Benkadda, I. O. Bespamyatnov, and W. L. Rowan. Fluid models of impurity transport via drift wave turbulence. *Physics of Plasmas*, 17(7):072512, July 2010. doi: 10.1063/1.3459062.

[24] Robert J. Goldston and Paul H. Rutherford. *Introduction to Plasma Physics*. Institute of Physics Publishing, London, UK, 1995.

[25] A Hasegawa and M Wakatani. Plasma edge turbulence. *Physical Review Letters*, 50(9):682–686, 1983. ISSN 00319007. doi: 10.1103/PhysRevLett.50.682. URL `http://link.aps.org/doi/10.1103/PhysRevLett.50.682`.

[26] Akira Hasegawa. Drift-wave instability at the plasmapause. *Journal of Geophysical Research*, 76(22):5361–5364, 1971. URL `http://adsabs.harvard.edu/abs/1971JGR....76.5361H`.

[27] Akira Hasegawa and Kunioki Mima. Pseudo-three-dimensional turbulence in magnetized nonuniform plasma. *Physics of Fluids*, 21(1):87, 1978. ISSN

00319171. doi: 10.1063/1.862083. URL http://link.aip.org/link/?PFLDAS/21/87/1.

[28] R. D. Hazeltine and J. D. Meiss. *Plasma Confinement*. Dover Publications, Minoela, New York, 2003.

[29] Per Helander and Dieter J. Sigmar. *Collisional Transport in Magnetized Plasmas*. Cambridge University Press, Cambridge, UK, 2002.

[30] G. T. Hoang, C. Bourdelle, X. Garbet, B. Pégourié, J. F. Artaud, V. Basiuk, J. Bucalossi, C. Fenzi Bonizec, F. Clairet, L.-G. Eriksson, C. Gil, R. Guirlet, F. Imbeaux, J. Lasalle, C. Lowry, B. Schunke, J. L. Ségui, J. M. Travère, E. Tsitrone, and L. Vermare. Turbulent particle transport in Tore Supra. *Nuclear Fusion*, 46:306–316, February 2006. doi: 10.1088/0029-5515/46/2/014.

[31] I. Holod, W. L. Zhang, Y. Xiao, and Z. Lin. Electromagnetic formulation of global gyrokinetic particle simulation in toroidal geometry. *Physics of Plasmas*, 16(12):122307, December 2009. doi: 10.1063/1.3273070.

[32] W. Horton. Drift waves and transport. *Reviews of Modern Physics*, 71(3): 735–778, April 1999. ISSN 0034-6861. doi: 10.1103/RevModPhys.71.735. URL http://link.aps.org/doi/10.1103/RevModPhys.71.735.

[33] W. Horton, B. G. Hong, and W. M. Tang. Toroidal electron temperature gradient driven drift modes. *Physics of Fluids*, 31:2971–2983, October 1988. doi: 10.1063/1.866954.

[34] W Horton, H.V Wong, P.J Morrison, A Wurm, J.H Kim, J.C Perez, J Pratt, G.T Hoang, B.P LeBlanc, and R Ball. Temperature gradient driven electron transport in NSTX and Tore Supra. *Nuclear Fusion*, 45 (8):976–985, August 2005. ISSN 0029-5515. doi: 10.1088/0029-5515/45/8/025. URL `http://stacks.iop.org/0029-5515/45/i=8/a=025?key=crossref.8e09cb15059575edabe922a1654b15eb`.

[35] W. Horton, P. J. Morrison, X. R. Fu, and J. Pratt. Transport with reversed $e_r$ in the gamma-10 tandem mirror. *Transactions of Fusion Science and Technology*, 55(2T), February 2009.

[36] W. Horton, Jr. Drift wave stability of inverted gradient profiles in Tokamaks. *Physics of Fluids*, 19:711–718, May 1976. doi: 10.1063/1.861517.

[37] Wendell Horton. *Turbulent Transport in Magnetized Plasmas*. World Scientific Publishing, Singapore, 2012. ISBN 9789814383530.

[38] W Horton Jr, D I Choi, and WM Tang. Toroidal drift modes driven by ion pressure gradients. *Physics of Fluids*, 24(6):1077–1085, 1981. URL `http://link.aip.org/link/?PFLDAS/24/1077/1`.

[39] W. A. Houlberg, K. C. Shaing, S. P. Hirshman, and M. C. Zarnstorff. Bootstrap current and neoclassical transport in tokamaks of arbitrary collisionality and aspect ratio. *Physics of Plasmas*, 4:3230–3242, September 1997. doi: 10.1063/1.872465.

[40] G. Hu and W. Horton. Minimal model for transport barrier dynamics based on ion-temperature-gradient turbulence. *Physics of Plasmas*, 4 (9):3262, 1997. ISSN 1070664X. doi: 10.1063/1.872467. URL `http://link.aip.org/link/PHPAEN/v4/i9/p3262/s1\&Agg=doi`.

[41] A. E. Hubbard, D. G. Whyte, R. M. Churchill, I. Cziegler, A. Dominguez, T. Golfinopoulos, J. W. Hughes, J. E. Rice, I. Bespamyatnov, M. J. Greenwald, N. Howard, B. Lipschultz, E. S. Marmar, M. L. Reinke, W. L. Rowan, and J. L. Terry. Edge energy transport barrier and turbulence in the I-mode regime on Alcator C-Mod. *Physics of Plasmas*, 18(5):056115, May 2011. doi: 10.1063/1.3582135.

[42] J. W. Hughes, D. Mossessian, K. Zhurovich, M. Demaria, K. Jensen, and A. Hubbard. Thomson scattering upgrades on Alcator C-Mod. *Review of Scientific Instruments*, 74:1667–1670, March 2003. doi: 10.1063/1.1532764.

[43] S. M. Kaye, F. M. Levinton, D. Stutman, K. Tritz, H. Yuh, M. G. Bell, R. E. Bell, C. W. Domier, D. Gates, W. Horton, J. Kim, B. P. LeBlanc, N. C. Luhmann, Jr., R. Maingi, E. Mazzucato, J. E. Menard, D. Mikkelsen, D. Mueller, H. Park, G. Rewoldt, S. A. Sabbagh, D. R. Smith, and W. Wang. Confinement and local transport in the National Spherical Torus Experiment (NSTX). *Nuclear Fusion*, 47:499–509, July 2007. doi: 10.1088/0029-5515/47/7/001.

[44] W. W. Lee. Gyrokinetic approach in particle simulation. *Physics of Fluids*, 26:556, 1983. URL http://link.aip.org/link/?PFLDAS/26/556/1.

[45] Y. C. Lee, J. Q. Dong, P. N. Guzdar, and C. S. Liu. Collisionless electron temperature gradient instability. *Physics of Fluids*, 30:1331–1339, May 1987. doi: 10.1063/1.866248.

[46] W. S. Lewis, J. L. Burch, J. Goldstein, W. Horton, J. C. Perez, H. U. Frey, and P. C. Anderson. Duskside auroral undulations observed by IMAGE and their possible association with large-scale structures on the inner edge of the electron plasma sheet. *Geophysical Research Letters*, 32 (24):L24103, December 2005. ISSN 0094-8276. URL http://www.agu.org/pubs/crossref/2005/2005GL024390.shtml.

[47] Z. Lin. Turbulent Transport Reduction by Zonal Flows: Massively Parallel Simulations. *Science*, 281(5384):1835–1837, September 1998. doi: 10.1126/science.281.5384.1835. URL http://www.sciencemag.org/cgi/doi/10.1126/science.281.5384.1835.

[48] Z. Lin, L. Chen, and F. Zonca. Role of nonlinear toroidal coupling in electron temperature gradient turbulence. *Physics of Plasmas*, 12(5): 056125, 2005. ISSN 1070664X. doi: 10.1063/1.1894766. URL http://link.aip.org/link/PHPAEN/v12/i5/p056125/s1\&Agg=doi.

[49] R.G. Littlejohn. Variational principles of guiding centre motion. *Journal*

*of Plasma Physics*, 29(1), 1983. URL http://journals.cambridge.org/production/action/cjoGetFulltext?fulltextid=4732472.

[50] G.P. Maddison, M. Brix, R. Budny, M. Charlet, I. Coffey, J.G. Cordey, P. Dumortier, S.K. Erents, N.C. Hawkes, M. von Hellermann, D.L. Hillis, J. Hogan, L.D. Horton, L.C. Ingesson, S. Jachmich, G.L. Jackson, A. Kallenbach, H.R. Koslowski, K.D. Lawson, A. Loarte, G.F. Matthews, D. McDonald, G.R. McKee, A. Meigs, A.M. Messiaen, F. Milani, P. Monier-Garbet, M. Murakami, M.F.F. Nave, J. Ongena, M.E. Puiatti, E. Rachlew, J. Rapp, S. Sharapov, G.M. Staebler, M. Stamp, J.D. Strachan, W. Suttrop, G. Telesca, M.Z. Tokar, B. Unterberg, M. Valisa, K.-D. Zastrow, and EFDA-JET 2000 workprogramme contributors. Impurity-seeded plasma experiments on jet. *Nuclear Fusion*, 43(1):49, 2003. URL http://stacks.iop.org/0029-5515/43/i=1/a=306.

[51] F. A. Marcus, I. L. Caldas, Z. O. Guimaraes-Filho, P. J. Morrison, W. Horton, Yu. K. Kuznetsov, and I. C. Nascimento. Reduction of chaotic particle transport driven by drift waves in sheared flows. *Physics of Plasmas*, 15(11):112304, 2008. ISSN 1070664X. doi: 10.1063/1.3009532. URL http://link.aip.org/link/PHPAEN/v15/i11/p112304/s1\&Agg=doi.

[52] E. Mazzucato, D. R. Smith, R. E. Bell, S. M. Kaye, J. C. Hosea, B. P. Leblanc, J. R. Wilson, P. M. Ryan, C. W. Domier, N. C. Luhmann, Jr., H. Yuh, W. Lee, and H. Park. Short-Scale Turbulent Fluctuations Driven by the Electron-Temperature Gradient in the National Spherical Torus

Experiment. *Physical Review Letters*, 101(7):075001, August 2008. doi: 10.1103/PhysRevLett.101.075001.

[53] P. J. Morrison. On Hamiltonian and Action Principle Formulations of Plasma Dynamics. *AIP Conference Proceedings*, 329(1):329–344, 2009. doi: 10.1063/1.3266810. URL http://link.aip.org/link/APCPCS/v1188/i1/p329/s1\&Agg=doi.

[54] Philip J. Morrison. Poisson brackets for fluids and plasmas. *AIP Conference Proceedings Volume 88*, 13(1):13–46, 1982. doi: 10.1063/1.33633. URL http://link.aip.org/link/APCPCS/v88/i1/p13/s1\&Agg=doi.

[55] S. E. Parker and A. K. Sen. Simulation of cylindrical ion temperature gradient modes in the Columbia Linear Machine experiment. *Physics of Plasmas*, 9:3440–3448, August 2002. doi: 10.1063/1.1488950.

[56] Jean C. Perez, W. Horton, Roger D. Bengtson, and Troy Carter. Study of strong cross-field sheared flow with the vorticity probe in the Large Plasma Device. *Physics of Plasmas*, 13(5):055701, 2006. ISSN 1070664X. doi: 10.1063/1.2179423. URL http://link.aip.org/link/PHPAEN/v13/i5/p055701/s1\&Agg=doi.

[57] D Pfirsch and PJ Morrison. Local conservation laws for the Maxwell-Vlasov and collisionless kinetic guiding-center theories. *Physical Review A*, 32(3), 1985. URL http://www.ph.utexas.edu/~morrison/85PRA_morrison.pdf.

[58] Dieter Pfirsch and Darío Correa-Restrepo. New method of deriving local energy- and momentum-conserving Maxwell-collisionless drift-kinetic and gyrokinetic theories: basic theory. *Journal of Plasma Physics*, 70(6):719–755, December 2004. ISSN 0022-3778. doi: 10.1017/S0022377804002995. URL http://www.journals.cambridge.org/abstract_S0022377804002995.

[59] W. L. Rowan, I. O. Bespamyatnov, and R. S. Granetz. Wide-view charge exchange recombination spectroscopy diagnostic for Alcator C-Mod. *Review of Scientific Instruments*, 79(10):100000, October 2008. doi: 10.1063/1.2979865.

[60] William L. Rowan, Igor O. Bespamyatnov, and C.L. Fiore. Light impurity transport at an internal transport barrier in Alcator C-Mod. *Nuclear Fusion*, 48(10):105005, 2008. URL http://stacks.iop.org/0029-5515/48/i=10/a=105005.

[61] P. H. Rutherford. Impurity transport in the Pfirsch-Schluter regime. *Physics of Fluids*, 17(9):1782, 1974. ISSN 00319171. doi: 10.1063/1.1694975. URL http://link.aip.org/link/PFLDAS/v17/i9/p1782/s1\&Agg=doi.

[62] V. Sokolov and A. K. Sen. A new paradigm for plasma turbulent transport. *Nuclear Fusion*, 45:439–449, June 2005. doi: 10.1088/0029-5515/45/6/005.

[63] D. L. Toufen, Z. O. Guimaraes-Filho, I. L. Caldas, F. A. Marcus, and K. W. Gentle. Turbulence driven particle transport in Texas Helimak. *Physics of Plasmas*, 19(1):012307, 2012. ISSN 1070664X. doi: 10.1063/1.3676607. URL http://link.aip.org/link/PHPAEN/v19/i1/p012307/s1\&Agg=doi.

[64] L.N. Trefethen. *Spectral Methods in MATLAB*. Software, Environments, Tools. Society for Industrial and Applied Mathematics, 2000. ISBN 9780898714654. URL http://books.google.com/books?id=l1YfkwEfQtQC.

[65] X. Wei, V. Sokolov, and A. K. Sen. Experimental production and identification of electron temperature gradient modes. *Physics of Plasmas*, 17 (4):042108, April 2010. doi: 10.1063/1.3381070.

[66] J. Weiland. *Collective Modes in Inhomogeneous Plasmas: Kinetic and Advanced Fluid Theory*. Plasma Physics Series. Taylor & Francis, 1999. ISBN 9780750305891. URL http://books.google.com/books?id=cDNKgCqDh6UC.

[67] KW Wenzel and DJ Sigmar. Neoclassical analysis of impurity transport following transition to improved particle confinement. *Nuclear Fusion*, 30: 1117, 1990. URL http://iopscience.iop.org/0029-5515/30/6/013.

[68] Yong Xiao and Zhihong Lin. Turbulent Transport of Trapped-Electron Modes in Collisionless Plasmas. *Physical Review Letters*, 103(8):1–4, Au-

gust 2009. ISSN 0031-9007. doi: 10.1103/PhysRevLett.103.085004. URL http://link.aps.org/doi/10.1103/PhysRevLett.103.085004.

[69] M. Yoshinuma, K. Ida, M. Yokoyama, M. Osakabe, K. Nagaoka, S. Morita, M. Goto, N. Tamura, C. Suzuki, S. Yoshimura, H. Funaba, Y. Takeiri, K. Ikeda, K. Tsumori, and O. Kaneko. Observation of an impurity hole in the Large Helical Device. *Nuclear Fusion*, 49 (6):062002, June 2009. ISSN 0029-5515. doi: 10.1088/0029-5515/49/6/062002. URL http://stacks.iop.org/0029-5515/49/i=6/a=062002?key=crossref.05213edea08b522f67cc5ab0c73eb5af.

# Index

*Abstract*, vi
*Acknowledgments*, v
*Appendices*, 124

*Bibliography*, 150
BOUT++, 14

C-Mod, 49, 62
classical transport, 5
CLM, 95

D-T reaction, 1
*Dedication*, iv
drift kinetic, 12
drift velocities, 16
drift wave, 7, 51
DTRANS, 14

ETG, 27, 90

fluctuation spectrum, 74

Gamma-10, 38
GTC, 15, 100
gyrokinetic, 10, 15

H-mode, 50, 80
Hasegawa-Mima, 17
Hasegawa-Wakatani, 20

I-mode, 80
Impurity Transport, 48
*Notation*, 135
ionosphere, 31
ITB, 50, 80
ITER, 62
ITG, 24, 75

Lawson criterion, 1
LHD, 87

mirror machine, 37
MPI, 15

neoclassical, 5, 70
NERSC, 15
nontwist map, 42

OpenMP, 15

passive, 69
plasma dispersion function, 125
plasmapause, 35
Poisson bracket, 18

quasilinear, 72
quasilinear theory, 50

TACC, 15
TEM, 26, 77
tokamak, 2, 58
turbulent transport, 5

# Vita

Xiangrong Fu was born in Shanghang, Fujian, P. R. China in 1982, the son of Shanhua Fu and Chunying Yuan. He received the Bachelor of Science degree in geophysics in 2003 from the University of Science and Technology of China (USTC). He then attended the graduate school at USTC and received the Master of Science degree in space physics in 2007. He started his Ph.D. in plasma physics at the University of Texas at Austin in the fall of 2007, and finished the study in 2013.

Permanent address: 3363 Lake Austin Blvd #D
Austin, Texas 78703

This dissertation was typeset with LaTeX[†] by the author.

[†]LaTeX is a document preparation system developed by Leslie Lamport as a special version of Donald Knuth's TeX Program.